Near-wall turbulence in the transitionally rough regime

Nabil Abderrahaman-Elena

Department of Engineering
University of Cambridge

This dissertation is submitted for the degree of
Doctor of Philosophy

Darwin College September 2018

Para mamá.

I'm sure he regarded the whole phenomenon of turbulence
as being unrigorous and probably invented by the Devil
on the seventh day of Creation (when the Good Lord wasn't looking);
I am inclined to agree.
— *Turbulence: the chief outstanding difficulty of our subject.*
Peter Bradshaw.

Declaration

I hereby declare that except where specific reference is made to the work of others, the contents of this dissertation are original and have not been submitted in whole or in part for consideration for any other degree or qualification in this, or any other university. This dissertation is my own work and contains nothing which is the outcome of work done in collaboration with others, except as specified in the text and Acknowledgements. This dissertation contains fewer than 65,000 words including appendices, bibliography, footnotes, tables and equations and has fewer than 150 figures.

Nabil Abderrahaman-Elena
May 2019

Acknowledgements

Firstly, I would like to express my sincere gratitude to my supervisor Ricardo. Without his support and guidance, I would not be where I am.

I would also like to thank all the academics that have helped me during my research, especially Dr. Daniel Chung, Prof. Jonathan Morrison and Prof. Sergei Chernyshenko for their support and insightful comments on my work.

I am grateful to my labmates for making my days a bit more fun and a bit less monotonous, especially, I'd like to thank Chris, Akshath, Garazi and Joe. My sincere thanks to Chris, in particular, with whom I've shared this journey from beginning to end.

This adventure would have not been possible without the support of my friends. I would like to thank those from the lab, Darwin, Cambridge, Spain, or just from around the world, those who fed me, cooked tortilla and Serbian sausage, and gave me a place to stay, those who I've recently met and those who I met even before moving from France, those who I can always find at the other end of the phone, those who live in Cambridge, London or Davis, those I've rowed, climbed, lifted and run with; thanks to all of you, thanks for sharing a bit of your lives with me to make mine better.

Y, finalmente, gracias a mi familia por todo.

Abstract

The purpose of this thesis is to investigate and model how roughness increases drag in turbulent flows.

This work focuses on the transitionally rough regime, where roughness is large enough to have an impact on drag but the rough regime is not fully developed. By restricting ourselves to this regime, we can investigate the changes produced in the flow by roughness before the canonical smooth-wall turbulence is entirely altered. To study this regime, direct numerical simulations of turbulent flows over transitionally rough surfaces are conducted.

First, a modulated triple decomposition of the flow is proposed to study the effect that roughness produces on the overlying turbulence. This decomposition allows us to separate the roughness-coherent component from the background turbulence. Second, the roughness function is decomposed into different contributions to identify the sources of drag increase and propose the initial steps towards a predictive model. A simplified model for the roughness function is then presented. Finally, the modifications to turbulence that arise for larger roughness size, when scaled in viscous units, are also analysed; notably the increase in energy of short, wide eddies, which is consistent with the appearance of a shear flow instability. A complementary study is also presented, which models densely packed roughness elements as anisotropic permeable substrate. This analysis leads to the study of permeable substrates, with the focus, not on drag increase, but on their potential capability to reduce drag.

Contents

Nomenclature

Roman symbols

B	Smooth-wall intercept of the logarithmic velocity profile.
B'	Fully rough intercept of the logarithmic velocity profile.
c	Complex phase velocity.
C_f	Friction coefficient.
CFL	Courant–Friedrichs–Lewy numerical stability condition.
D	Discrete divergence operator.
$\mathbb{D}$	Divergence of the velocity: $\mathbb{D} = \nabla \boldsymbol{u}$.
DNS	Direct Numerical Simulation.
DR	Drag reduction.
$\mathbb{F}$	Divergence free equation right-hand-side.
E_{uu}	Spectral density of the streamwise velocity.
E_{uv}	Spectral density of the Reynolds shear stress.
E_{vv}	Spectral density of the wall-normal velocity.
E_{ww}	Spectral density of the spanwise velocity.
G	Discrete gradient operator.
H	Upper limit of integration of the mean momentum equation.
h	Lower limit of integration of the mean momentum equation.
h_p	Height of the permeable layer.
k	Height of roughness.

k_s	Equivalent sand grain size.
k_{s_∞}	Fully rough equivalent sand grain size.
k_x	Wavenumber in the streamwise direction.
k_z	Wavenumber in the spanwise direction.
$\mathtt{Ktens}$	Permeability tensor.
K_x	Permeability in the streamwise direction.
K_y	Permeability in the wall-normal direction.
K_z	Permeability in the spanwise direction.
$\mathcal{K}$	Permeability function (piecewise-linear profile).
$\widetilde{\mathcal{K}}$	Equivalent permeability (piecewise-linear profile).
$\widetilde{K}$	Equivalent permeability (turbulent profile).
$\widetilde{K}^+_{KH}$	Permeability limit for maximum drag reduction in wall units.
L	Discrete Laplacian operator.
L_x	Length of the channel in the streamwise direction.
L_z	Width of the channel in the spanwise direction.
ℓ_J	Displacement height.
ℓ_U	Virtual origin of the mean velocity profile.
ℓ_u	Virtual origin of the streamwise root-mean-square fluctuations.
ℓ_{uv}	Virtual origin of the Reynolds shear stress.
ℓ_s	Slip length.
ℓ_x	Slip velocity in the streamwise direction.
ℓ_z	Slip velocities in the spanwise direction.
N	Discrete non-linear operator.
n_x	Number of grid points in the streamwise direction.
n_y	Number of grid points in the wall-normal direction.
n_z	Number of grid points in the spanwise direction.
p	Pressure.
Q	Mean flow rate.
Re	Reynolds number.
Re_D	Divergence free equation parameter
Re_τ	Frictional Reynolds number.

RHS	Right-hand-side.
S_x	Uniform shear in the streamwise direction.
s_x	Texture pattern wavelength in the streamwise direction.
s_z	Texture pattern wavelength in the spanwise direction.
T	Contribution to the integral of the mean momentum equation.
t	Time.
U	Streamwise mean velocity profile.
U_0	Mean velocity at the roughness crests, $y = 0$.
U_D	Mean velocity inside the permeable substrate.
U_s	Mean slip velocity at the permeable interface.
$\boldsymbol{u}$	Velocity.
u	Velocity component in the streamwise direction.
u_τ	Frictional velocity $u_\tau = \sqrt{\tau_w/\rho}$.
$\boldsymbol{V}$	Forcing velocity at the immersed boundary grid points.
v	Velocity component in the wall-normal direction.
$\overline{v}'_t$	Root-mean-square of the wall-normal velocity component at the roughness crests.
$\widetilde{v}$	Conditional mean v with respect to its direction over a roughness element.
$\widetilde{w}$	Conditional mean w with respect to its direction over a roughness element.
w	Velocity component in the spanwise direction.
x	Streamwise coordinate.
y	Wall-normal coordinate.
y_c	Inner scaling of the shear flow instability, $y_c \approx 8$.
y_r	Wall-normal coordinate measured from the virtual origin of the mean velocity.
z	Spanwise coordinates.

Greek symbols

α	Coefficient of the explicit contribution of the viscous term.
α_{BJ}	Beavers-Joseph jump condition coefficient.
$\alpha_{i_{RK}}$	Runge-Kutta coefficient by Le and Moin (1991).
α_x	Wavenumber in the streamwise direction.
α_z	Wavenumber in the spanwise direction.
β	Coefficient of the implicit contribution of the viscous term.
$\beta_{i_{RK}}$	Runge-Kutta coefficient by Le and Moin (1991).
$\gamma_{i_{RK}}$	Runge-Kutta coefficient by Le and Moin (1991).
δ	Half-height of the channel measured from roughness crests to centreline.
δ'	Half-height of the channel measured from the virtual origin of the mean velocity profile, $\delta' = \delta + \ell_U$.
ΔC_f	Change in friction coefficient respect to the smooth-wall case.
ΔP	Mean pressure gradient.
ΔU	Roughness function.
Δt	Time step.
Δx	Grid spacing in the streamwise direction.
Δy	Grid spacing in the wall-normal direction.
Δz	Grid spacing in the spanwise direction.
$\zeta_{i_{RK}}$	Runge-Kutta coefficient by Le and Moin (1991).
κ	Kármán constant.
λ_D	Divergence free equation parameter.
λ_x	Wavelength in the streamwise direction.
λ_z	Wavelength in the spanwise direction.
μ_0	Ratio between the roughness function and the slip length.
ν	Kinematic viscosity.
$\tilde{\nu}$	Macroscale apparent viscosity.
ρ	Density.
σ	Amplification of the flow instability.

τ_w	Mean skin friction.
ϕ	Fractional step pressure correction.
Φ_{xy}	Anisotropy of the permeable layer, $\Phi_{xy} = \sqrt{K_x/K_y}$.
ω_x	Streamwise vorticity component.

Superscripts

$+$	Variable in wall units, normalized using u_τ and ν.
$\prime$	Root-mean-square fluctuation.

Subscripts

δ	Values at the centreline.
i_{RK}	Runge-Kutta sub-step.
BT	Background turbulent component.
RC	Roughness-coherent component.
RC, u	Roughness-coherent component induced by u.
RC, v	Roughness-coherent component induced by v.
RC, w	Roughness-coherent component induced by w.

Other symbols

$\hat{(\cdot)}$	Fourier transform of $(\cdot)$.
$\langle(\cdot)\rangle$	Average of $(\cdot)$ in time and in the homogeneous spatial directions.
$\mathcal{F}(\cdot)$	Fourier transform of $(\cdot)$.
$\mathcal{O}(\cdot)$	Order of magnitude of $(\cdot)$ (Landau's big O notation).
$\mathcal{T}$	Contribution to the integral of the mean momentum equation.

1. The transitionally rough regime

We are surrounded by fluids. Their presence shapes our interactions, activities and technology. And yet we still cannot fathom many of the secrets of their dynamics. The understanding of their behaviour is key, especially that of the chaotic, and seemingly random, turbulent regime. Turbulence plays an active role in a wide variety of technological problems, with friction drag and pressure losses directly traced back to it. The economic impact of turbulence can be quantified as its negative effects can be directly translated into the form of energy losses. The presence of roughness enhances the aforementioned effects of wall-bounded turbulence, increasing even further friction and pressure losses. However, the mechanics and physics that lead to such changes still remain unclear.

A glance back to the past shows how much interest turbulence has arisen. As early as the 15$^{\text{th}}$ century, Da Vinci (1452–1519) formulated one of the first descriptions of turbulence and, to an extent, the first visualisation of a turbulent flow. It took three more centuries to obtain a formal description of the motion of fluids, the Navier–Stokes equations, named after Claude-Louis Navier (1785–1836) and Sir George Gabriel Stokes (1819–1903). Not long after, Osborne Reynolds (1842–1912) carried out some of the first modern experiments and visualisations, as well as reported invaluable findings about turbulence and transition. Nowadays, turbulence is still a hot topic, to the point that it has being included as one of the seven *Millennium Prize Problems*.

The interest in fluid mechanics and turbulence has steadily grown, eventually developing a vast field of study. As in most new branches in engineering, the challenge was to go farther, faster, and higher; understanding nature and using it to our advantage. Classical examples are the first flights by the Wright brothers and the Space Race during the Cold War. In recent years, that angle has shifted.

The paradigm has changed. The overarching challenges have been achieved, now the goal is to perform better, to be more efficient. In a world where resources are finite and the footprint of humans on earth is patent, efficiency has become a major factor to consider in any design. In fluid dynamic problems, the cost is generally measured in terms of energy; the energy paid in order to move fluid, or to be moved when immersed in a fluid. For aerodynamic bodies, one of the main source of losses is the friction drag. For aeroplanes, skin friction accounts for roughly one half of the total drag (Spalart and McLean, 2011), i.e. half of the energy supplied by the engines. In pipelines and ducts, this ratio is even higher, as friction drag is the only cause of energy losses in straight sections. Friction drag is, in most cases, intensified by the presence of roughness. At the high velocities found in most industrial flows, even seemingly small roughness may unexpectedly increase drag. The presence of roughness can greatly increase skin friction, which in turn, as mentioned, represents an important contribution to the total energy input in many industrial applications. Understanding the underlying physics of turbulent flows over rough surfaces will indisputably lead to an improvement in performance, as well as a decrease in used resources and energy losses.

In this chapter we review wall-bounded turbulent flows and their interaction with roughness. We limit ourselves to the transitionally rough regime, where the modification on the flow by roughness are still weak, and we can still observe similarities and differences with respect to smooth-wall flows. When roughness is large, the flow is changed to a great extent, rendering its study more complex. Furthermore, if the flow is only moderately altered, the knowledge on smooth-wall turbulence can be used to one's advantage. This regime, in which the effect of roughness is not fully developed in the flow, is the ideal setup to observe the effect that roughness of small size starts having on the flow, as well as the physics that accompany those changes. In the last part of the chapter, we overview some methods that can be used to simulate turbulence and roughness surfaces, and explain the reasons that lead us to opt for this particular methodology.

1.1. Wall-bounded turbulence

In experience, flows that move sufficiently fast become disordered. This chaotic state is referred to as turbulence. While there is an extensive literature about the topic, an established definition of turbulence has not yet been agreed. Instead, it is common practice to enumerate its features, and dodge the formulation of an actual definition (Tennekes and Lumley, 1972; Pope, 2001). In particular, wall-bounded turbulence is the subject of a large amount of current research, as these flows, which include pipes, channels and boundary layers, are common in most technological applications. Their relevance resides in most pressure losses in ducts and friction drag in vehicles being caused by wall-bounded turbulence.

Turbulent flows, although chaotic, display certain organisation and certain coherence. Robinson (1991) defines coherent motions as three-dimensional regions of the flow over which some fundamental variable, such as velocity component or vorticity, exhibits significant correlation over a range of space and time larger than the smallest local scales of the flow. Although the author himself criticises the generality of this definition, it includes the main characteristics: coherent motions are parts of the flow that correlate in time and space for longer than pure random fluctuations would. Streaks were the first of these structures to be identified in wall-bounded flows (Kline et al., 1967). These are elongated regions of high and low velocity, with a characteristic length of order 1000 wall units (Kim et al., 1971) and a width of approximately 100 wall units (Smith and Metzler, 1983). Some authors suggest that coherent structures can be interpreted as major blocks that compose the flow. Studying their dynamics and their relationship with macroscopic characteristic of the flow has been one of the classical approaches to turbulence (Townsend, 1976; Robinson, 1991; Jiménez and Pinelli, 1999; Jiménez, 2018).

1.2. Roughness

Although one of the oldest problems in fluid dynamics, the understanding of roughness in turbulent flows is still an active area of research. Turbulent flows over rough surfaces have been thoroughly studied due to their ubiquity and im-

pact in pressure losses and drag increase, as well as in mixing and heat transfer. Roughness is commonly found in an immense variety of situations, both natural and artificial. Atmospheric flows interact with grass, forests, topography and urban landscape, affecting the motion of the upper layers of the atmosphere. Soon after ships are launched, hulls are populated by microorganisms, algae and animals, referred to as biofouling; the surface is then no longer smooth with drag and costs increasing notably (Schultz et al., 2011). At high Reynolds number, most technological flows are in practice developed over rough walls. Engineers like Darcy (1856), especially concerned about pressure losses in pipe flows, began studying turbulent flows over rough walls more than a century and a half ago. Since then, a large number of experimental, theoretical and numerical works have been conducted. Initially, the main focus was placed on exploring the universality of roughness and establishing correlations. During the last century the attention has also been drawn towards other questions, such as the study of outer flows and the differences between types of roughness. The classical studies by Schlichting (1968), Raupach et al. (1991), Jiménez (2004), and more recently by Flack and Schultz (2014), compile and summarise results on flows over rough surfaces. Roughness has also become a relevant aspect in the understanding and modelling of atmospheric flows. The review by Finnigan (2000) on flows over plant canopies is a useful reference regarding those flows.

The seminal works by Nikuradse (1933) and Colebrook and White (1937), offering a systematic study of turbulent flows over rough surfaces, set the foundations for the field. Nikuradse manufactured samples of pipes with rough interior wall. Sand of equal grain size was used to systematically roughen these surfaces. Results of the velocity profiles showed that the law of the wall holds over rough walls. Additionally, the friction obtained was measured as a function of the Reynolds number for all different sand roughness sizes. Based on the friction he identified three regimes: the hydraulically smooth regime, equivalent to smooth-wall behaviour; the fully rough regime, where the roughness function is independent of the Reynolds number; and the transitionally rough regime that serves as a transition between them. Unlike the hydraulically smooth regime, the fully rough regime is represented by a family of curves whose governing parameter is the equivalent sand grain size. The research by Nikuradse (1933) was

highly valuable from a scientific point of view, but the morphology of the sand grain roughness studied was substantially different from those rough surfaces found in industrial applications. Following a similar methodology to that by Nikuradse (1933), Colebrook and White (1937) and Colebrook (1939) conducted a campaign of experiments on commercial pipes. Using their results and Nikuradse's, they proposed a general expression that correlates friction and Reynolds number of the flow. These correlations are commonly used by engineers in the form of the Moody chart (Moody, 1944), where figure 1.2 depict its main features.

Nikuradse's results showed that sufficiently far away over rough walls the mean velocity profile exhibits the same logarithmic behaviour found in smooth-wall turbulence. Effectively, roughness only modifies the intercept of the logarithmic velocity profile while the Kármán constant, κ, and the wake function are unaffected (Nikuradse, 1933; Clauser, 1956; Castro, 2007). In the logarithmic layer, the mean velocity profile, U, can then be expressed as

$$U^+ = \kappa^{-1} \ln(y^+) + B + \Delta U^+ = U_0^+ + \Delta U^+, \tag{1.1}$$

where the Kármán constant is $\kappa \approx 0.36$–0.39 (Marusic et al., 2010b; Mizuno and Jiménez, 2011; Luchini, 2017), and the smooth-wall intercept of the logarithmic velocity profile $B \approx 5.1$, in channel flows. The roughness function, ΔU^+ (Hama, 1954), depends on the particular geometry of the roughness texture and its size. The subscript $_0$ denotes values on a corresponding smooth-wall flow. The superscript $^+$ indicates scaling in wall units using the kinematic viscosity ν and the friction velocity, $u_\tau = (\tau_w/\rho)^{1/2}$, where τ_w is the mean wall shear stress and ρ is the density. In the fully rough regime, Nikuradse (1933) finds that the mean velocity profile can be rewritten in the form

$$U^+ = \kappa^{-1} \ln(y^+/k_s^+) + B', \tag{1.2}$$

where $B' \approx 8.5$ and the equivalent sand roughness size k_s^+ appears explicitly. Clauser (1956) found that equations (1.1) and (1.2) can be combined to obtain an

expression for the roughness function,

$$\Delta U^+ = 3.4 - \kappa^{-1} \ln k_s^+. \tag{1.3}$$

This expression also represents a definition for k_s^+. By establishing a direct relationship with ΔU^+, this expression highlights that k_s^+ is a property of the flow, not of the surface. The equivalent sand roughness size, k_s^+, is essentially a measure of the hydrodynamic response of the flow to roughness. In the work by Flores and Jiménez (2006), the fully rough regime was simulated using velocity disturbances at the wall, and they could still define the k_s^+ value of their flow based on the roughness function. Also notice that k_s^+ is a Reynolds number and it is equivalent to the frictional Reynolds number, Re_τ, although it is based on the sand grain roughness height as length scale, $k_s^+/Re_\tau = k_s/\delta$, with δ the thickness of the flow, i.e. the boundary layer thickness or the channel half-height, for instance. Equation (1.3) also allows to characterise the corresponding equivalent sand roughness, k_s^+, to other surfaces with the same ΔU^+. The concept of equivalent sand grain roughness was proposed by Schlichting (1936), in which surfaces are assigned the same k_s^+ as the sand roughness case that produces the same friction. This approach captures the complexity of the roughness geometry within one single parameter. However, Colebrook and White (1937) highlighted that this parameter does not adequately represent the transitionally rough regime. Recent experimental works also show how the actual surface arrangement, and not only the height of the roughness elements, significantly affects the skin friction and flow structure within the roughness sublayer (Amir and Castro, 2011; Florens et al., 2013; Placidi and Ganapathisubramani, 2015; Placidi and Ganapathisubramani, 2018).

Jiménez (2004) points out that for values of $k_s^+ \lesssim 4$ the skin friction provided by equation (1.3) would be lower than that over a smooth-wall. In most cases, however, friction remains bounded by the smooth-wall case. On the other hand, this is not a rule; riblets are a remarkable exception that do reduce skin friction (Walsh and Lindemann, 1984; Bechert et al., 1997). Riblets are a special case of organised roughness composed by grooves aligned with the mean flow, that reduce drag in a certain range of height and spacing. In the vast majority of

cases, however, roughness increases wall friction. Jiménez (2004) suggests that the reason might be that roughness is a better generator of wall friction than the viscous cycle (Jiménez and Pinelli, 1999). This is based on the idea that roughness, of characteristic height k, would alter the viscous sublayer and the buffer-layer, affecting the viscous cycle or even destroying it for $k^+ \gtrsim 50$–100.

The change in friction coefficient, ΔC_f, can be directly related to ΔU^+. At the centreline of a channel or in the free-stream in a boundary layer, denoted by the subscript $_\delta$, the mean velocity is U_δ. The friction coefficient C_f is then

$$C_f = \frac{\tau_w}{1/2\rho U_\delta^2} = \frac{2u_\tau^2}{U_\delta^2} = \frac{2}{U_\delta^{+2}}. \tag{1.4}$$

While in channel flows, it is common to scale the skin friction with the bulk velocity instead of the centreline velocity, the latter allows for a better comparison with boundary layer results (García-Mayoral and Jiménez, 2011; Garcia-Mayoral et al., 2018). Making use of this expression for the friction coefficient, equation (1.1) evaluated at δ becomes

$$(2/C_f)^{1/2} = U_\delta^+ = U_{\delta_0}^+ + \Delta U^+, \tag{1.5}$$

with $U_{\delta_0}^+$ the value of U_δ^+ over a smooth wall. For changes in friction, ΔC_f, the previous equation gives

$$\Delta C_f = C_f - C_{f_0} = \frac{2}{\left(U_{\delta_0}^+ + \Delta U^+\right)^2} - \frac{2}{U_{\delta_0}^{+2}}, \tag{1.6}$$

that results in

$$\frac{\Delta C_f}{C_{f_0}} = -\frac{1}{\left(1 + \Delta U^+/U_{\delta_0}^+\right)^2} - 1. \tag{1.7}$$

This expression establishes the link between the roughness function and the change in friction. It shows that an increase in friction is always accompanied by a downward displacement of the velocity profile towards the wall, and vice versa. In the context of drag reduction, the same or similar linearised expressions for ΔC_f are discussed by Luchini (1996), Spalart and McLean (2011), García-Mayoral and Jiménez (2011) and Garcia-Mayoral et al. (2018). Express-

ing the change in friction as a function of ΔU^+ presents advantages with respect to using the change in friction coefficient, ΔC_f. Drag depends on the particular setup, i.e. whether the flow is internal or external. Even more, in numerical periodic channels, some authors propose that the drag force cannot be defined unambiguously (MacDonald et al., 2018).

Friction is commonly found to be a function of the roughness height, k, with roughness geometries that obey equation (1.3) usually referred to as k-roughness. However, some rough surfaces, notably spanwise-aligned bars, have been found to display a different behaviour. Perry et al. (1969) coined the term d-roughness that refers to surfaces in which friction is not a function of k but a function of δ, i.e. the boundary layer thickness, the channel half-height or the pipe radius. This roughness has been mainly studied experimentally (Perry et al., 1969; Djenidi et al., 1999), with the work by Leonardi et al. (2007) being one of the first numerical simulations to investigate it. Recently MacDonald et al. (2018) re-examined this question, proposing that friction scales with the spacing between spanwise elements, as opposed to the thickness of the flow as it was previously believed.

Notice that equation (1.1) is obtained by establishing a comparison with an equivalent smooth-wall channel. In flows over smooth walls, the origin for the wall-normal coordinates, y, is clearly determined by the wall. However, over roughness, a straightforward origin for y cannot be identified. In literature, the position of this origin of coordinates is commonly expressed as an offset from the bottom of the roughness troughs, or from the roughness crests, referred to as displacement height. In experiments, the displacement height is usually estimated to maximise the fit of the Kármán constant in the log region to the values for smooth walls (Jiménez, 2004). In simple roughness geometries, such as those frequently used in numerical experiments, it is often determined based on geometrical considerations. For instance, Chan et al. (2015) and MacDonald et al. (2016) place the origin of y at the half-height of their sinusoidal roughness. This approach, however, fails in the extreme cases of very dense, as it tends to become a smooth wall shifted to the top of the highly packed sinusoids (MacDonald et al., 2016), and very sparse roughness, as the flow behaves as that over a smooth wall with isolated obstacles, as in the model by Bradshaw (2000). The origin of the y-coordinate can also be related to the obstruction that the rough elements pro-

duce on the flow. One such approach is taken by Jackson (1981), who defines the displacement height using the momentum balance below the roughness crests. A similar approach is also common in the drag reduction community. In riblets and superhydrophobic surfaces, this obstruction is characterised by introducing the concepts of longitudinal protrusion height (Bechert and Bartenwerfer, 1989) and slip velocity, which is the value of the velocity at the plane of the roughness tips. These measures are analogous to the displacement height, and are defined as the height at which the mean velocity profile seemingly tends to zero as it approaches the wall.

1.3. Transitional roughness

In the hydraulically smooth regime, the roughness is of small size and has a negligible effect on the flow. The rough surface causes no change on the wall friction, being effectively equivalent to canonical smooth-wall turbulence. In the fully rough regime, on the other hand, roughness dominates. The friction coefficient becomes independent of the Reynolds number and the roughness geometry determines the friction drag. Between these two regimes there is the so-called transitionally rough regime (Colebrook, 1939). Nikuradse (1933) observed that his sand grain roughness was hydraulically smooth for $k_s^+ \lesssim 5$, fully rough for $k_s^+ \gtrsim 70$, and transitional between those extremes. However, Colebrook and White (1937) and Colebrook (1939) noticed important discrepancies in the behaviour of the friction function for different roughness surfaces. They found that surfaces yielding the same friction in the fully rough regime, and therefore characterised by the same k_s^+, may differ in the friction produced in the transitionally rough regime, as illustrated in figure 1.1. Flack and Schultz (2010) compiled experimental results for typologies of roughness other than sand grain roughness, finding that the limits of the different regimes vary considerably. In particular, the literature shows the transitionally rough regime spanning $1.4\text{–}15 \lesssim k_s^+ \lesssim 18\text{–}70$. This has important consequences on the applicability of the Moody chart (Moody, 1944), as it does not correctly describe the transitionally rough regime for all surfaces, as the limits of the transitionally rough regime depend on each particular geometry. Recently, the importance of numerical simulations has been

highlighted as a means to replace the Moody chart (Flack, 2018).

The lower bound of the transitionally rough regime has classically been treated as a threshold below which the surface completely behaves as a smooth wall. Nikuradse (1933) observed that the results for roughness surfaces below a certain k_s^+ agreed, within experimental error, with smooth-wall results. In that light, he proposed a hard boundary that separates the hydraulically smooth regime from the transitionally rough regime. Notice that equation (1.3), which seemingly agrees with this view, is not valid in the transitionally rough regime, and in particular, the additive factor B' in equation (1.2) is no longer constant (Nikuradse, 1933). For those small roughness elements, one would expect viscous effects to dominate, with advective effects quickly taking over in importance as k^+ increases. This would give rise to a progressive adaptation rather than an abrupt threshold. Based on this concept, Bradshaw (2000) proposed and modelled a gradual transition between these regimes, without a defined hard boundary. A recent numerical study by Thakkar et al. (2018) also seems to point in this direction.

Figure 1.2 depicts the three hydrodynamic regimes of flows over rough walls. In this classical representation, friction is displayed as a function of the Reynolds number. The fully rough regime is represented by a family of horizontal lines as it is independent of viscosity and the friction only depends on the roughness size for a given roughness topology. To focus on the transitionally rough regime, Jiménez (2004) proposed to study the evolution of ΔU^+ as a function of $k_{s_\infty}^+$. The equivalent sand grain roughness k_{s_∞} of an arbitrary surface corresponds to the sand grain roughness k_s that yields the same friction in the fully rough regime. Notice that k_{s_∞} is a geometric property of the surface. The roughness surfaces characterised in figure 1.1 display different types of transition across the hydrodynamic regimes. Some evolutions are abrupt, presenting a sudden increase in friction beyond a certain roughness size; and some are more gradual, where ΔU^+ progressively increases with the roughness size. This transition tends to be abrupt in organised geometries, while the presence of a wider range of sizes makes it more gradual (Colebrook and White, 1937). Notice that in this work the term transition refers to evolutions across hydrodynamic regimes and not to the laminar–turbulent transition, as the flow is always considered to be turbu-

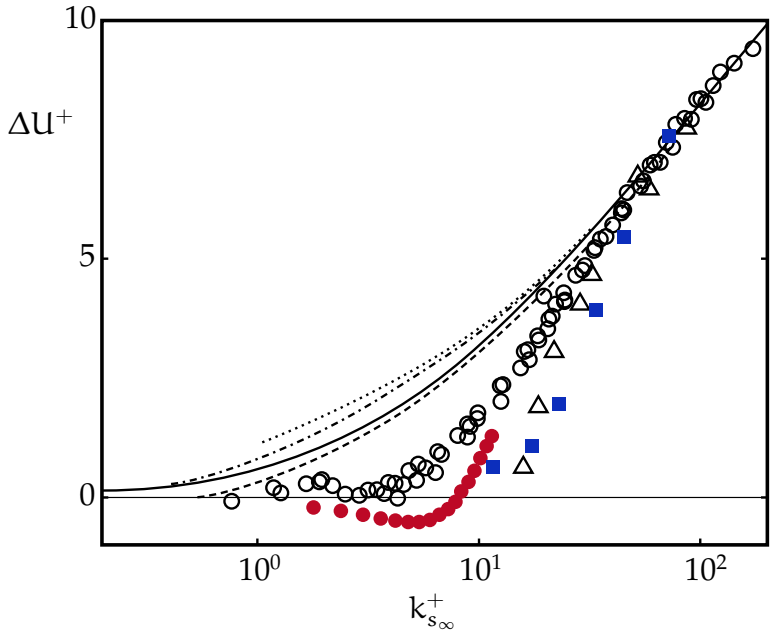

Figure 1.1.: Roughness function in the transitionally rough regime as a function of Reynolds number based on k_{s_∞}. ○, uniform sand (Nikuradse, 1933); △, uniform packed spheres (Ligrani and Moffat, 1986); ●, triangular riblets (Bechert et al., 1997); ■, cases C06 to C36 presented in this work (see section 2.6); ····· , galvanized iron; – – , tar-coated cast iron; –·– , wrought-iron; ——, interpolation (Colebrook, 1939). Adapted from Jiménez (2004)

lent. Figure 1.1 shows that the transition of non-uniform roughness (Colebrook, 1939) extends over a range about a decade larger than uniform sand roughness (Nikuradse, 1933), and almost two with respect to uniform spheres (Ligrani and Moffat, 1986).

Jiménez (2004) suggests that, in the transitionally rough regime, the friction produced by conventional roughness is determined by two opposing mechanisms. On the one hand, the form drag generated by the rough elements increases skin friction. On the other hand, the viscous cycle (Jiménez and Pinelli, 1999) is altered and eventually destroyed, resulting in drag reduction. Depending on the particular surface, this mechanisms would have different intensities, and as a result different geometries would display different evolutions in the transitionally rough regime. As k^+ increases, the second effect completely destroys the viscous cycle and the form drag of roughness dominates.

In figure 1.1, the results corresponding to riblets present an unusual beha-

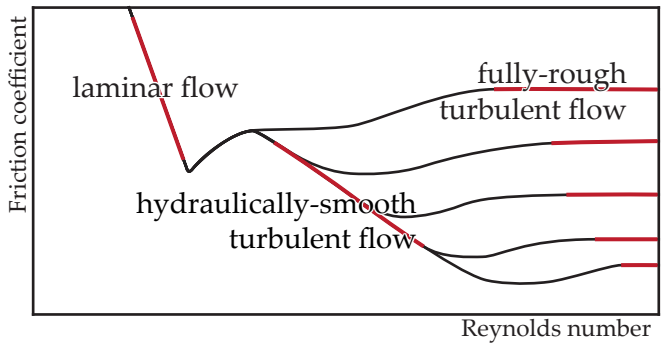

Figure 1.2.: Schematic representation of the Moody chart. In red the three hydrodynamic regimes.

viour, going to values of friction below that for smooth wall and hence reducing drag. Riblets display this drag-reducing effect in a small range of values of k^+ in the transitionally rough range. For larger values of k^+, riblets behave as conventional roughness. The reduction in drag is caused by the difference in the slip velocity created between the streamwise and spanwise directions (Luchini et al., 1991; Jiménez, 1994). For larger riblet size, the appearance of spanwise roller structures destroys the drag reduction effect, with riblets beginning to behave as conventional roughness. These rollers, caused by a Kelvin-Helmholtz instability, increase mixing and drag, destroying the drag reducing effect (García-Mayoral and Jiménez, 2011). The appearance of this instability has been reported over several and very different surfaces. Similar spanwise rollers have been observed over obstructed surfaces in general (Ghisalberti, 2009), including flows over plant canopies (Raupach et al., 1996; Ikeda and Kanazawa, 1996; Finnigan, 2000; Py et al., 2006; Ghisalberti and Nepf, 2006), and flows over permeable walls (Jiménez et al., 2001; Breugem et al., 2006; Abderrahaman-Elena and García-Mayoral, 2017; Sharma et al., 2017; Gómez-de-Segura et al., 2018c; Gómez-de-Segura et al., 2018b). While spanwise rollers have been observed over riblets and canopies, their presence has never been reported over conventional roughness. In the transitionally rough regime we may be able to identify the signature of this instability.

The relevance of the equivalent sand roughness, k_s, resides in relating any rough surface with Nikuradse's original experiment. This allows us to classify

and parametrise surfaces based on their effect on the flow. A major example of the importance of k_s is the Moody chart, relating skin friction and Reynolds number via a parameter that is essentially k_s. However, there are two important shortcomings in this strategy. Firstly, as stated by Bradshaw (2000), it "simply defines a useful common currency for roughness size—like paper money, valueless in itself but normally acceptable as a medium of exchange", i.e. k_s is merely a classifier, an a posteriori parameter that is of limited use for prediction purposes. Furthermore, Colebrook (1939) observed that, despite sharing the same value of k_s in the fully rough regime, different surfaces vary in how they depart from the hydraulically smooth regime. Many studies in the recent years have aimed to find a better combination of parameters to describe roughness surfaces and predict their friction. Some authors have explored the effective slope, the solidity, as well as different moments of the roughness height, mainly the mean, the standard deviation and the skewness (Flack and Schultz, 2010; Placidi and Ganapathisubramani, 2015; Jelly et al., 2017). A universal governing parameter is, however, yet to be found, and the changes in the flow that lead to the increase in friction have not been explored in depth or with little success. The work developed by Orlandi and Leonardi (2006) proposes a substitute parameter to k_s, based on the change produced by the rough surface on the local flow. They show that skin friction is strongly correlated to flow statistics at the wall. However, the relationship between these statistical values and the actual roughness geometry remains an open question. As stated by Marusic et al. (2010b), "without further theoretical advances, there is a risk of needing a catalogue of roughness results". Alternatively to seeking a universal parameter, the use of minimal channels, proposed by Chung et al. (2015), lowers the computational cost of roughness simulations. This represents an important step forward in predicting friction of roughness. However, individual cases still need to be computed, with the actual effect of roughness surfaces on the turbulent flow still not fully understood.

1.4. Flow simulation

1.4.1. Direct numerical simulation

The effect of roughness on the flow is generally considered to be confined to the roughness sublayer, a region that extends above the wall to a distance of the order of the roughness height (Raupach et al., 1991; Flack et al., 2007). Flow physics tied to both turbulence and roughness, which are characterised by their own length scales, coexist and interact in this region. Experiments provide great insight about integral properties of the flow, such as friction and pressure drop (Acharya et al., 1986), and large scale structures (Volino et al., 2007; Vanderwel and Ganapathisubramani, 2015). For the past three decades, numerical simulations of turbulence have proven to complement experimental studies. A widespread approach is to numerically solve all scales of turbulence and roughness without artificially modelling turbulence. Simulations in which all scales are directly solved are referred to as direct numerical simulations (DNS), and have played a major role in the study of turbulence (Moin and Mahesh, 1998; Jiménez and Moser, 2007). However, simulations are costly in time and computational resources, setting a limitation to the problems that can be tackled. In particular, high resolution is necessary to capture all scales present in the flow. This requires a high number of grid points, which, as a result, leads to demanding memory and computational requirements. For a prescribed domain, the resolution and storage requirements increase with the Reynolds number as a function of order $\mathcal{O}(\mathrm{Re}^{9/4})$, and the number of operations as $\mathcal{O}(\mathrm{Re}^{11/4})$ (Canuto et al., 1988). The existing technology sets then a practical limit to the maximum Reynolds number that can be reached. Unfortunately, it is still highly costly to conduct simulations with Reynolds numbers of the order of typical engineering applications, and, even then, only with simple geometry configurations. Kim et al. (1987) conducted the first direct numerical simulation of a turbulent channel flow, reaching a Reynolds number of $\mathrm{Re}_\tau = 180$. We had to wait more than a decade to raise the Reynolds number up to $\mathrm{Re}_\tau = 590$ (Moser et al., 1999). Since then, the Reynolds number of the simulations has been increasing alongside with the advancements in technology: reaching $\mathrm{Re}_\tau \approx 1000$ (Álamo et al.,

2006), $Re_\tau \approx 2000$ (Hoyas and Jiménez, 2006), $Re_\tau \approx 4000$ (Bernardini et al., 2014; Lozano-Durán and Jiménez, 2014), and recently attaining $Re_\tau \approx 5200$ (Lee and Moser, 2015). Some of the earliest roughness direct numerical simulations were carried out by Choi et al. (1991) and Choi et al. (1993).

The direct numerical simulations by Kim et al. (1987) and Moser et al. (1999) are spectral in the homogeneous directions, exploiting the periodicity of the domain. To decouple velocity and pressure in the momentum equation, they use the fractional step method (Chorin, 1968). This method was proposed for turbulent flows by Kim and Moin (1985), and formalised and further explored by Perot (1993). If the Navier–Stokes equations are expressed in matrix form, the fractional step scheme is effectively an LU decomposition, permitting the use of high-order temporal methods. This method is combined with a time-integrator scheme. Initially, (Kim and Moin, 1985) used a second-order Adams-Bashforth explicit scheme for the advective terms and a second-order Crank-Nicholson semi-implicit scheme for the viscous terms. This time integrator was successfully used in the historical Re_τ-180 channel by Kim et al. (1987). The predictor-corrector used by Moser et al. (1999) was an hybrid three-substep Runge Kutta scheme that solves explicitly the advective term and semi-implicitly the viscous terms (Spalart, 1991).

The size of the numerical domain also has an effect on the physics represented. The distance between the periodic boundary conditions limits the size of turbulent structures that can develop in the flow. Essentially, if the domain is too small, any point is potentially affected by itself through the periodic boundaries. Jiménez and Moin (1991) characterised the minimum domain in which turbulence is self-sustained; the flow becomes laminar for smaller domain sizes. However, they report that, while the near-wall cycle is maintained (Jiménez and Pinelli, 1999), a large extent of the turbulent channel does not correctly resolve turbulence. This concept of unresolved, or not *healthy*, turbulence was further explored by Flores and Jiménez (2010). They characterise the height of the region where *healthy* turbulence is maintained based on the width and length of the domain. A domain of length $2\pi\delta$ and width $\pi\delta$, where δ is half the distance between the parallel walls, is large enough to correctly represent turbulence. While larger structures, present in high-Reynolds-number flows (Hutchins and

Marusic, 2007), cannot be captured, that domain size is sufficient to correctly represent one-point statistics, identical to those in larger domains (Lozano-Durán and Jiménez, 2014).

Minimal channel simulations (Jiménez and Moin, 1991) resolve most of the physics in the near-wall region at a lower computational cost than full simulations. Chung et al. (2015) and MacDonald et al. (2017) make use of the minimal channel concept to calculate the skin friction of roughness surfaces. The effect of roughness surfaces on the near-wall turbulence is well resolved, thereby capturing the correct change on the intercept of the log profile. The roughness function, ΔU^+, is obtained by comparing this shift with that on the corresponding smooth-wall minimal channel. This technique has been used to study sinusoidal roughness (MacDonald et al., 2016) and spanwise bars (MacDonald et al., 2018).

1.4.2. Immersed boundary method

The techniques to represent rough surfaces can be broadly classified in two groups. On the one hand, methods that adapt the grid and the equations to fit the boundaries of the domain to the rough geometry. Only fluid is contained within the numerical domain and no-slip conditions are imposed at the boundaries to represent the geometry. On the other hand are methods that introduce artificial forces in the domain that mimic the presence of the roughness elements.

Unstructured grid methods are part of the first group of techniques that adapt to the surface. The fluid domain is subdivided using polyhedrons whose nodes and faces can be placed fitting the surface. Finite elements and finite volumes are classical examples of these methods. Although less common in direct numerical simulations, these techniques are frequently used in combination with Reynolds-averaged Navier–Stokes simulations and Large Eddy Simulations. Their main advantage is that they can be more easily used to represent complex geometries, such as those found in many industrial applications. In particular, finite volumes are widely used in commercial software for computational fluid dynamics. In turn, finding the appropriate mesh to represent those complex geometries entails its own difficulties. A different family within this same group consists in combining structured grids and conformal mapping. A

structured grid is mapped to the domain, where the boundaries of the grid are transformed to shape the roughness surface. The differential equations are also transformed using curvilinear coordinate system (Ferziger and Perić, 2002). This method, however, is only adequate for simple geometries that can be analytically defined. Triangular riblets (Choi et al., 1993) and sinusoidal roughness (Chan et al., 2015; MacDonald et al., 2016) are cases in which this methodology has been successfully implemented.

Immersed boundary methods (Peskin, 1972; Mittal and Iaccarino, 2005) belong to the second group of techniques, which do not rely on modifying either the governing equations nor the grid. Instead, the roughness is represented by introducing forcing in the domain. This forcing mimics the presence of solid bodies and their boundaries.

The main advantage of immersed boundary methods is that the grid definition is extremely simple as they can be implemented on a Cartesian grid which does not conform to the geometry. Therefore, the generation of the grid and the spatial discretisation are much simpler than in unstructured grid methods. Additionally, the cell geometry does not need to be incorporated into the discretisation of the equations, as it is the case in the body-conformal techniques. The original immersed boundary method was initially developed by Peskin (1972) for elastic boundaries. In particular, these methods have been widely used to study biological flows, such as those through arteries and the heart. The seminal work by Peskin (1972) has since experienced a profound evolution and improvement, giving rise to a multitude of techniques. Commonly, they are classified into continuous forcing and discrete forcing approaches. In the discrete forcing techniques, the governing equations are first discretised onto the grid, and afterwards, discrete forces are added to account for the presence of the surface. The original method was proposed by Mohd-Yusof (1997), although modifications have been implemented based on the works by Fadlun et al. (2000) and Iaccarino and Verzicco (2003). This methodology has been widely used to study rough-wall turbulent channel flows (Orlandi and Leonardi, 2006; Busse et al., 2015; Thakkar et al., 2018).

1.5. Objectives

In this chapter, we have shown that turbulent flows over rough surfaces are present in a wide variety of situations. They are a key factor in atmospheric dynamics, and play a major role in the performance of most means of transportation, as well as in the energy losses in ducts and pipelines, amongst other applications. In particular, the transitionally rough regime has a strong relevance on a multitude of technological problems. In industrial applications at high velocities, even with well-controlled micro-texture, smooth surfaces enter the transitionally rough regime. This, alongside with the improvements on simulations that are now approaching the Reynolds number of typical engineering applications, has stirred up interest in the topic amongst the high–Reynolds-number community (Marusic et al., 2010b). The interest in transitional roughness also resides in understanding the effects that roughness begins to produce in the flow before it is completely modified. Furthermore, while it may seem that it has a narrow scope, the study of the transitionally rough regime is of more general relevance as it marks the onset of the fully rough behaviour. As size increases, the effects of the rough surface intensify, leading to the departure from the hydraulically-smooth regime and eventually reaching the fully rough regime. Moreover, predicting the skin friction and, in particular, the roughness function are questions that have not been fully answered yet. The classical approaches used in engineering to predict the effect of rough surfaces have limited predictive capability. The equivalent sand grain roughness, k_s, on which the widespread Moody chart is based, does not appropriately predict drag in the transitionally rough regime. Recent studies have aimed to find a better characterisation of the surface. An approach that has shown promising results is that of using reduced models for the flow to obtain the roughness function. All in all, the transitionally rough regime has a great relevance in industry, with physics that have not yet been elucidated.

The approach taken in this work is to understand the modifications produced on the flow by the roughness texture. Specifically, we aim to gain insight into the transitionally rough regime. The final goal is to develop a model to predict the friction drag of a surface based on its roughness geometry alone. To

develop such a model, we first study whether rough flows can be decomposed into independent components, with one capturing the effect of roughness, and another capturing that of the overlying turbulence. Once such a decomposition is developed, we can study the flow by investigating these simpler components. In particular, we investigate the effect of the rough surface on the background turbulence, and the generation of the roughness-induced component of the turbulence by the roughness geometry. Based on that knowledge, we can propose models to estimate the behaviour of the component of the flow: the background turbulent-like component and the roughness-induced component. Combining those models, we finally propose a model for friction drag.

The problem is studied by means of direct numerical simulations of turbulent flows over different rough surfaces and through a range of roughness sizes in the transitionally rough regime. We restrict ourselves to classical k-roughness behaviour, which is more frequently found in engineering and research, and is characteristic of most three-dimensional rough surfaces. These roughness surfaces are represented using the immersed boundary method, which is a widely used technique in the field. Details on the methodology, implementation, and numerical experiments are given in chapter 2. In chapter 3, we analyse how the flow can be decomposed into simpler components. In particular, we separate the flow into one component induced by roughness and coherent with the texture, and a second component that captures the background turbulence with no footprint from the rough surface. Once the roughness-induced contribution is removed, we analyse how the presence of roughness alters the energy distribution and coherent structures of the background turbulence. Some attention is also paid to the height of the roughness sublayer, and to the effect of the rough surface beyond that region, i.e. whether outer-layer turbulence is altered. These findings are combined in chapter 4 to develop a preliminary model for the roughness function. In chapter 5, we study the signature of a flow instability in our data, similarly to those in obstructed flows. We present an analysis of the stability of flows using parameters that characterise the rough surface. The model assumes small size and densely packed roughness, so the flow is highly obstructed and the permeability equations approximate the behaviour within the roughness canopy. This model, initially intended for representing small size

roughness surfaces, is, in a more general sense, a representation of a porous coating. In chapter 6, we take advantage of the insight gathered about the stability of these permeable surfaces, and explore their drag reduction capabilities. This thesis is concluded in chapter 7.

2. Numerical method and simulation setup

The numerical experiments are conducted in a turbulent channel with roughness on the top and bottom walls. The problem is described by the incompressible Navier–Stokes and continuity equations

$$\frac{\partial \boldsymbol{u}}{\partial t} + \boldsymbol{u} \cdot \nabla \boldsymbol{u} = -\nabla p + \frac{1}{Re} \nabla^2 \boldsymbol{u}, \tag{2.1a}$$

$$\nabla \cdot \boldsymbol{u} = 0, \tag{2.1b}$$

where $\boldsymbol{u}$ is the velocity field, Re is the Reynolds number and p is the kinematic pressure, the ratio between the pressure and the density of the fluid. The streamwise, wall-normal and spanwise coordinates are respectively x, y and z, with u, v and w the corresponding components of the velocity $\boldsymbol{u}$. The flow is driven in the streamwise direction by a uniform pressure gradient. We restrict ourselves to the incompressible problem, therefore density can be taken as unity and drop from the equations without loss of generality. The characteristic length and velocity scales of the problem are the half-height of the channel, δ, and the bulk velocity, i.e. the cross-sectional average of the velocity. The domain is periodic in the wall-parallel directions. The channel half-height, δ, is measured from the roughness crests to the centreline, and the length and width of the domain are $L_x = 2\pi\delta$ and $L_z = \pi\delta$, respectively, which has been shown to be appropriate to capture the physics of the problem (Flores and Jiménez, 2010; Lozano-Durán and Jiménez, 2014).

In this chapter the characteristics of the numerical method are outlined. The code was originally developed by García-Mayoral (2011) for his study on turbulent flows over riblets, and it has been adapted for the present work on rough-

ness. The temporal integrator is a fractional-step method combined with a three–sub-step Runge–Kutta method. The treatment of the pressure is implicit, the viscous terms are semi-implicit, and the non-linear advective terms are solved explicitly. The boundary conditions at the walls are $\boldsymbol{u} = 0$ at the first and last planes of the domain, as in a smooth-wall channel simulation. The roughness geometry is implemented using immersed boundary method that modifies the right-hand-side of equation (2.1a) via body forces.

In this chapter, we first introduce the fractional-step method and the Runge–Kutta scheme used for the integration in time of equations (2.1). Then we present the spatial discretisation, followed by the immersed boundary method used to simulate roughness. In the last part of the chapter, we discuss the validation of this numerical implementation.

2.1. Temporal discretisation

Velocity and pressure in equations (2.1) are decoupled using the fractional-step method (Chorin, 1968). While the final implementation of the time integrator uses a Runge–Kutta scheme, we first illustrate the fractional-step method using a simpler first order scheme, for the sake of clarity. The Navier–Stokes equations (2.1) are integrated using an explicit Euler time integrator, of the form $\partial u/\partial t \approx (u^{n+1} - u^n)/\Delta t$, with $\Delta t = t^{n+1} - t^n$, that yields

$$\frac{\boldsymbol{u}^{n+1} - \boldsymbol{u}^n}{\Delta t} = -Gp^{n+1} - N(\boldsymbol{u}^n) + \frac{\alpha}{Re} L\boldsymbol{u}^n + \frac{\beta}{Re} L\boldsymbol{u}^{n+1}, \tag{2.2a}$$

$$D\boldsymbol{u}^{n+1} = 0 \tag{2.2b}$$

where D, G and L represent the discretised divergence, gradient and laplacian operators, respectively, and N is the non-linear advection operator. The superscript indicates the time-step, with n the current one where the flow field is already known, and $n+1$ is the next time-step, yet to be calculated. The factors α and β are the coefficients of the semi-implicit treatment of the viscous terms.

The previous expression can be rearranged into the form

$$\boldsymbol{u}^{n+1}\left(I-\Delta t\frac{\beta}{Re}L\right)+\Delta tGp^{n+1}=\boldsymbol{u}^{n}+\Delta t\left(-N\left(\boldsymbol{u}^{n}\right)+\frac{\alpha}{Re}L\boldsymbol{u}^{n}\right)=RHS, \tag{2.3a}$$

$$D\boldsymbol{u}^{n+1}=0, \tag{2.3b}$$

where I is the identity matrix and the right-hand-side, RHS, contains the explicit terms. On the left-hand-side, we explicitly observe the coupling between velocity and pressure. The fractional-step method is a strategy that allows for these variables to be calculated independently, by means of an intermediate base. Equations (2.3) expressed in matrix form yield

$$\begin{pmatrix} A & \Delta tG \\ D & 0 \end{pmatrix}\begin{pmatrix} \boldsymbol{u}^{n+1} \\ p^{n+1} \end{pmatrix}=\begin{pmatrix} RHS \\ 0 \end{pmatrix}, \tag{2.4}$$

where $A=\left(I-\Delta t\left(\beta/Re\right)L\right)$. The intermediate base is obtained by performing an LU-decomposition on equation (2.4) (Perot, 1993). In an LU-decomposition the equation $MX=Y$ becomes $LZ=Y$ with $Z=UX$, where $M=LU$ is a non-singular matrix, and L and U are lower and upper triangular matrices, respectively. Performing this decomposition on equation (2.4) results in

$$\begin{pmatrix} A & 0 \\ D & -\Delta tDA^{-1}G \end{pmatrix}\begin{pmatrix} \boldsymbol{u}_{\star}^{n+1} \\ p_{\star}^{n+1} \end{pmatrix}=\begin{pmatrix} RHS \\ 0 \end{pmatrix}, \tag{2.5a}$$

$$\begin{pmatrix} I & \Delta tA^{-1}G \\ 0 & I \end{pmatrix}\begin{pmatrix} \boldsymbol{u}^{n+1} \\ p^{n+1} \end{pmatrix}=\begin{pmatrix} \boldsymbol{u}_{\star}^{n+1} \\ p_{\star}^{n+1} \end{pmatrix}, \tag{2.5b}$$

where the subscript $_{\star}$ denotes intermediate variables. Notice that the matrix A^{-1} is time-dependent and, thus, has to be evaluated, and inverted, every time-step. Since $A=I+\mathcal{O}(\Delta t)$ and $\Delta t\ll 1$, we approximate $A^{-1}\approx I$ (Perot, 1993; Simens, 2008). Consequently, the pressure is only first order accurate, $\mathcal{O}(\Delta t)$, and the error propagates to the velocity at the correction stage in equation (2.5b). Therefore, regardless of the accuracy of the velocity, the overall accuracy of the method would be first order. However, this loss of accuracy can be addressed

and improved to second order by means of a mere change of variables. Neglecting the viscous part of A^{-1} produces an error $(\Delta t/Re)Lp^{n+1}$, of order $\mathcal{O}(\Delta t)$. The pressure can be expressed as $p^{n+1} = p^n + \phi^{n+1} + \mathcal{O}(\Delta t^2)$, with the pressure correction $\phi^{n+1} \sim \mathcal{O}(\Delta t)$. As suggested by Simens (2008), solving for the pressure correction produces an error $(\Delta t/Re)L\phi^{n+1}$, which results in an overall error of the method of order $\mathcal{O}(\Delta t^2)$. The pressure, p^{n+1}, remains first order accurate, but since it is calculated every time-step from the corrected velocity, its error does not propagate, and therefore does not carry forward. The method is therefore second order accurate in time for the velocity, and first order for the pressure. Equation (2.5) shows that the discretised Navier–Stokes equation (2.2) is equivalent to

$$\boldsymbol{u}_\star^{n+1}\left(1-\Delta t\frac{\beta}{Re}\right) = \boldsymbol{u}^n + \Delta t\left(\frac{\alpha}{Re}L\boldsymbol{u}^n - N\left(\boldsymbol{u}^n\right) + Gp^n\right), \tag{2.6a}$$

$$\Delta t DG\phi^{n+1} = D\boldsymbol{u}_\star^{n+1}, \tag{2.6b}$$

$$\boldsymbol{u}^{n+1} = \boldsymbol{u}_\star^{n+1} - \Delta t G\phi^{n+1}, \tag{2.6c}$$

$$p^{n+1} = p^n + \phi^{n+1}, \tag{2.6d}$$

where A^{-1} has been simplified to I and the pressure substituted to $p^{n+1} = p^n + \phi^{n+1}$. These equations form a sequence where there is only one unknown per equation, and the right-hand-side is always known explicitly from the previous time-step and previous steps of the sequence.

The fractional-step method decouples the Navier–Stokes equations (2.1), by means of an LU-decomposition. This is achieved by using an intermediate velocity, $\boldsymbol{u}_\star^{n+1}$. Although at first $\boldsymbol{u}_\star^{n+1}$ does not respect the incompressibility condition, it allows us to calculate the correct pressure in the following time-step, p^{n+1}. Once the pressure is known, this intermediate velocity can be corrected, thereby obtaining the incompressible velocity $\boldsymbol{u}^{n+1}$.

The fractional-step method has been introduced above using a simple first-order Euler time integrator. In our numerical experiments, we instead implement a three–sub-step Runge–Kutta time integrator that provides third-order accuracy for the advective terms and second-order accuracy for the viscous terms

Table 2.1.: Fractional step Runge–Kutta coefficients (Le and Moin, 1991).

i_{RK}	1	2	3
$\alpha_{i_{RK}}$	4/15	1/15	1/6
$\beta_{i_{RK}}$	4/15	1/15	1/6
$\gamma_{i_{RK}}$	8/15	5/12	3/4
$\zeta_{i_{RK}}$	0	−17/60	−5/2

(Le and Moin, 1991). Equation (2.1a) then results in

$$\left(1-\Delta t\frac{\beta_{i_{RK}}}{Re}L\right)\boldsymbol{u}^{n}_{i_{RK}} = \boldsymbol{u}^{n}_{i_{RK}-1} + \Delta t\Big(\frac{\alpha_{i_{RK}}}{Re}L\left(\boldsymbol{u}^{n}_{i_{RK}-1}\right) - \gamma_{i_{RK}}N\left(\boldsymbol{u}^{n}_{i_{RK}-1}\right) - \zeta_{i_{RK}}N\left(\boldsymbol{u}^{n}_{i_{RK}-2}\right) - \left(\alpha_{i_{RK}}+\beta_{i_{RK}}\right)G\left(p^{n}\right)\Big), \quad i_{RK}=1,2,3 \tag{2.7a}$$

$$DG\left(\phi^{n+1}\right) = \frac{1}{\Delta t}\left(D\left(\boldsymbol{u}^{n}_{3}\right)\right), \tag{2.7b}$$

$$p^{n+1} = p^{n}+\phi^{n+1}, \tag{2.7c}$$

$$\boldsymbol{u}^{n+1} = \boldsymbol{u}^{n}_{3}-\Delta tG\left(\phi^{n+1}\right). \tag{2.7d}$$

where $\boldsymbol{u}^{n}_{0} = \boldsymbol{u}^{n}$. The constants $\alpha_{i_{RK}}$, $\beta_{i_{RK}}$, $\gamma_{i_{RK}}$ and $\zeta_{i_{RK}}$, with $i_{RK} = 1,2,3$, are the Runge–Kutta method coefficients proposed by Le and Moin (1991), as in table 2.1. Equation (2.7a) is the advancement of the momentum equation at each sub-step i_{RK}. Notice that equations (2.7b) to (2.7d) are only calculated once per overall step, and the velocity and pressure are only corrected at the final step in equation (2.7). Le and Moin (1991) show that this correction can be performed at the final sub-step only without loss of accuracy. Figure 2.1 illustrate this idea, indicating three small corrections every sub-step as opposed to a larger single correction at the final sub-step. The time-step is adjusted to keep the condition for numerical stability, the CFL, constant,

$$\Delta t = \min(\Delta t_{conv}, \Delta t_{visc}), \tag{2.8}$$

$$\Delta t_{conv} = CFL\ \min[\Delta x/\left(\pi|u|\right), \Delta y/\left(|v|\right), \Delta z/\left(\pi|w|\right)], \tag{2.9}$$

$$\Delta t_{visc} = 2.5\ \min\left[\Delta x^{2}_{min}/\pi^{2}, \Delta y^{2}_{min}/4, \Delta z^{2}_{min}/\pi^{2}\right]. \tag{2.10}$$

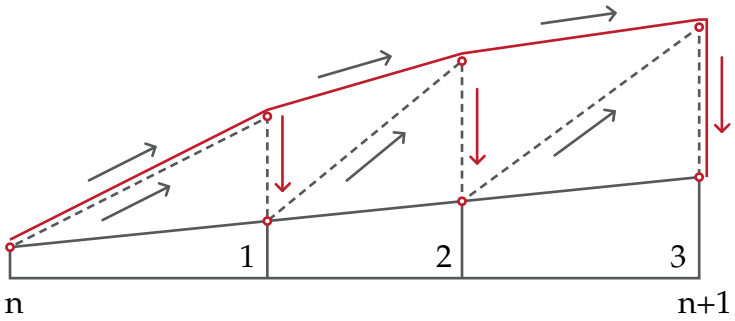

Figure 2.1.: Sketch of the evolution of the velocity through a time-step. Gray arrows are advancements of the momentum equation, and red arrows are pressure corrections. The dashed line is corrected every Runge–Kutta sub-step, while the red one is only corrected at the last sub-step. Adapted from Le and Moin (1991).

2.2. Pressure driven flow

The pressure gradient is adjusted to enforce a constant flow rate. Therefore, it fluctuates around its mean value. This yields statistically equivalent results to keeping the mean pressure gradient constant and letting the flow rate fluctuate (Quadrio et al., 2016), and provides a shorter time for statistical convergence (Nelson and Fringer, 2017).

Following Chu and Karniadakis (1993), to efficiently achieve a constant flow rate Q, the mean velocity can be adjusted by solving an equivalent Stokes flow driven by a unit pressure drop,

$$\left(1 - \Delta t \frac{\beta_{i_{RK}}}{Re} \frac{\partial^2}{\partial y^2}\right) U_\star(y) = -\Delta t \left(\alpha_{i_{RK}} + \beta_{i_{RK}}\right), \tag{2.11a}$$

$$\Delta P_\star = \frac{Q - Q^n_{iRK,\star}}{Q_\star}, \tag{2.11b}$$

$$U^n_{iRK}(y) = U^n_{iRK,\star}(y) + \Delta P_\star U_\star(y), \tag{2.11c}$$

where $U^n_{iRK,\star}$ is the uncorrected plane-averaged mean velocity profile, with $Q^n_{iRK,\star}$ its corresponding flow rate. $U_\star$, $Q_\star$ and $\Delta P_\star$ are auxiliary variables, where $Q_\star$ is the flow rate associated with $U_\star$. For simplicity, $U_\star$ is only defined above the roughness crests, with its boundary condition $U_\star(0) = 0$ at the roughness tips. There is no correction within the roughness region, between tips and troughs.

This produces a negligible error in the velocity field, because the corrections on the velocity and pressure are several orders of magnitude smaller than their uncorrected values (García-Mayoral, 2011). The procedure described by equations (2.11) has been widely used in both smooth-wall and rough channel direct numerical simulations (Choi et al., 1993; Chu and Karniadakis, 1993; Moser et al., 1999; Del Álamo and Jiménez, 2003; Hoyas and Jiménez, 2006; Orlandi and Leonardi, 2006).

2.3. Spatial discretisation

The periodicity of the domain along the wall-parallel directions calls for the use of pseudospectral discretisation. In particular, the periodic directions, x and z, are represented spectrally in Fourier space. The non-homogeneous wall-normal direction, y, on the other hand, is discretised using second order central finite differences.

2.3.1. Wall-parallel discretisation

The use of spectral discretisation for the wall-parallel directions, and in particular Fourier series, presents some advantages with respect to other methods. One of the major advantages of spectral methods is that they yield optimal resolution for a given number of collocation points. This is commonly referred to as spectral accuracy (Moin and Kim, 1982; Canuto et al., 1988). Additionally, the implementation of Fourier series has a positive impact on the computational cost of equation (2.7b). Periodic functions in a uniform grid can be represented by a discrete Fourier series

$$f(x_j) = \sum_{q=-n_x/2}^{n_x/2} \hat{f}(k_q) \exp\left(ik_q x_j\right), \quad \text{where} \quad \hat{f}(k_q) = \frac{1}{n_x} \sum_{j=0}^{n_x} f(x_j) \exp\left(-ik_q x_j\right), \tag{2.12}$$

where $x_j = j\Delta x$, Δx is the grid spacing, n_x is the number of grid points, and $k_q = 2\pi q/(n_x \Delta x)$. The periodicity requirement gives rise to q being undetermined.

That is, the value of $\exp(\pm ik_q x_j)$ is not modified when the index is translated from q to $q + ln_x$, where l is an integer. In every iteration of the time integrator a laplacian operator is inverted, as shown in section 2.1. This operation, however, turns trivial when expressed in Fourier space, since the derivatives become mere products,

$$\mathcal{F}(\partial_q f) = ik_q \mathcal{F}(f), \tag{2.13}$$

where $\mathcal{F}$ is the Fourier transform operator, $\mathcal{F}(f) \equiv \hat{f}$. When the problem is Fourier transformed along x and z, the linear operators then become decoupled in the wall-parallel directions, so the equations can be solved independently for each streamwise and spanwise mode. For instance, the expressions for the laplacian operator is

$$\mathcal{F}_{xz}\left(\nabla^2 f\right) = \mathcal{F}_{xz}\left(\left(\partial_x^2 + \partial_y^2 + \partial_z^2\right) f\right) = \left(\partial_y^2 - k_x^2 - k_z^2\right) \mathcal{F}_{xz}(f). \tag{2.14a}$$

On the other hand, this strategy suffers from an important drawback as the product of functions becomes a convolution in Fourier space,

$$\mathcal{F}(f \cdot g) = \mathcal{F}(f) \star \mathcal{F}(g). \tag{2.15}$$

Convolutions need to perform $\mathcal{O}(N^2)$ elementary operations, with N the size of the elements involved, which in our case is the number of grid points. As a result, there would be a drastic increase in the cost of computing the non-linear terms. To overcome this issue, the non-linear advective terms, $\boldsymbol{u}\cdot\nabla\boldsymbol{u}$ in (2.1a), are solved in physical space, where it only involves $\mathcal{O}(N)$ operations. To efficiently transform the flow field between physical and Fourier spaces we use the Fast Fourier Transform (Cooley and Tukey, 1965), which performs only $\mathcal{O}(N \log_2 N)$ operations (Canuto et al., 1988; Ferziger and Perić, 2002). Transforming the problem into physical space, computing the advective terms, and transforming back, in practice reduces the computational cost by one order of magnitude.

If not treated appropriately, this strategy of alternating between spectral and physical spaces may produce a numerical artefact called aliasing. Let us briefly explore the aliasing phenomenon. In equation (2.12) we observe that q is undetermined due to the periodicity requirement. The result is not altered by

adding or subtracting N, the number of collocation points in the domain, from q. This property of periodicity is preserved through linear operations. For instance, the derivatives of a discretised function share the same period indetermination of step N. However, non-linear operations, such as the product of two functions, may lead to a change in the number of modes that are necessary to correctly define the solution, and commonly it has to be represented in a larger domain. To illustrate this issue, let us consider the multiplication of f_s times f_t that generates all the possible combinations of $exp(\pm ik_s x_j)exp(\pm ik_t x_j) = exp(\pm i(k_s + k_t)x_j)$. Since both k_s and k_t take values in the interval $[-N/2, N/2]$, the resulting non-linear term includes wavelengths from $-N$ to N, twice as large as the initial domain. However, if the solution is projected back into the original interval $[-N/2, N/2]$, modes $\pm N$ indices apart cannot be distinguished, as mentioned above. This results in high frequencies being added to the lower ones, with the $[-N, -N/2]$ and $[N/2, N]$ intervals contaminating the solution in the original domain. As an example let us consider trigonometric functions in the domain $[-N/2, N/2]$,

$$\sin\left(2\pi\frac{j(N/3)}{N}\right)\cos\left(2\pi\frac{j(N/3)}{N}\right) = \frac{1}{2}\sin\left(2\pi\frac{2j(N/3)}{N}\right) \tag{2.16a}$$

$$= \frac{1}{2}\sin\left(-2\pi\frac{j(N/3)}{N} + 2\pi\frac{j(N)}{N}\right) \tag{2.16b}$$

$$\Rightarrow \frac{1}{2}\sin\left(-2\pi\frac{j(N/3)}{N}\right), \tag{2.16c}$$

which not only has an incorrect wavenumber but even its phase velocity has the opposite sign. This phenomenon is known as aliasing and, in non-linear differential equations, may be an important source of error if not addressed adequately (Ferziger and Perić, 2002). There are several methods to overcome this problem. The most commonly used are aliasing removal by padding or truncation, aliasing removal by phase shifts, and aliasing removal for orthogonal polynomials (Canuto et al., 1988). We select the first one for simplicity, and efficiency. As seen above, aliasing arises from the solution domain not being large enough to accommodate the resulting high wavenumbers. As a consequence, they are incorrectly captured in a complementary lower wavenumber within the avail-

able domain, thereby contaminating the solution. By enlarging the domain to a size of 2N and padding with zeros the additional wavenumber prior to the multiplication, we ensure that modes at all wavenumbers are correctly represented. The domain is then truncated back to the original working size N. The perfomance of this process can be improved by decreasing the size of the auxiliary domain to only 3/2N, as shown by Orszag (1971). The Fourier transform of a function, which is represented using n_x complex modes, is illustrated in figure 2.2(*a*). When this function is multiplied by another function defined in the same grid, the number of modes is doubled, $2n_x$, as shown in (*b*), yet only the first half is needed to achieve the original resolution of the problem. However, if we use fewer than $2n_x$ modes, as illustrated in (*c*), we suffer from the described aliasing: higher frequencies contaminate the lower ones. As the number of modes is reduced, a wider region is contaminated, the limit being when the extra region is 1/2 of the initial number of modes. That is, to de-alias we need a domain 3/2 times the initial size, as shown in (*d*). Finally, these additional modes are discarded and we recover the initial resolution, and thus the original number of modes.

2.3.2. Wall-normal discretisation

The periodicity of the problem along the wall-parallel directions favours the use of a Fourier series discretisation. However, walls create a non-homogeneity in the wall-normal direction, making Fourier series unsuitable. An alternative option is to implement the derivatives in the non-homogeneous direction, y, using a second order central finite difference scheme. Central finite difference schemes are of the form

$$f'_i \approx \sum_{i=-m}^{m} w_i \frac{f_{i+m}}{y_{i+m} - y_i}, \tag{2.17}$$

where i is the index of a grid point, $2m$ is the order of the scheme for an appropriate set of weighting coefficient, w_i. In particular, the second order central finite difference scheme implemented takes the simplified form

$$f'_i \approx \left(\frac{dy(\theta)}{d\theta}\right)^{-1} \frac{f_{i+1} - f_{i-1}}{2}, \tag{2.18}$$

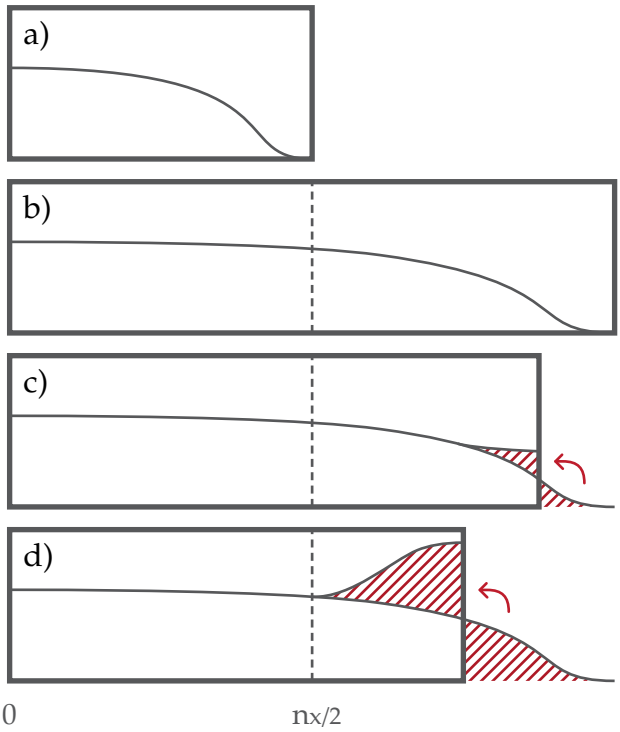

Figure 2.2.: Sketch of the de-aliasing method used. (*a*), representation of the Fourier transform of a function defined in a domain of size $n_x/2$; (*b*), representation of the Fourier transform of two functions in a domain of size $n_x/2$ that is large enough to accommodate all wavelengths; (*c*), wavelengths being contaminated because of aliasing when the domain is smaller than n_x; (*d*), smallest domain, of size $(3/2)n_x/2$, in which aliasing is avoided in the original domain of size $n_x/2$.

where $y(\theta)$ is the mapping from the index $\theta = [1, n_y]$ to the wall-normal coordinate, with n_y the number of grid points in the wall-normal direction. The term $dy/d\theta$ in equation (2.18) results from applying the chain rule to $df/dy = (df/d\theta)(d\theta/dy)$, since we know the analytical expression for $y(\theta)$. The expression $y(\theta)$ maps the stretched grid to an auxiliary unstretched one,

$$y(\theta) = c_1 (\theta - n_y/2) + c_2 (\theta - n_y/2)^5 , \tag{2.19}$$

where the c_i coefficients set the size of the channel, δ, and stretching of the grid.

As shown previously, the Fourier series discretisation decouples the wall-parallel direction, thereby individual modes can be resolved independently along the y direction. However, the differential operators still need to be inverted. Central finite differences only involve adjacent points, and therefore the discrete operators are tridiagonal, which improves the efficiency and further reduces the computational cost. On the other hand, low order finite difference schemes exhibit low spatial resolution, since they are highly numerically dispersive (Trefethen, 1996). This is a potential source of numerical error in finite

difference methods as they demand high resolution to represent quickly varying functions. Fluctuations that take place over long distances, spanning several grid points, are well-represented, while fluctuations with a short wavelength compared to the grid spacing are not well-captured. The error associated with differentiating schemes is classically assessed using Fourier analysis, which provides a way to quantify its resolution accuracy, also called dispersion or phase error (Lele, 1992). The analysis presented hereafter considers periodic functions to simplify the mathematical development. Despite the domain being bounded, this analysis is still valid in the core of the flow, away from the boundaries. Lele (1992) presents an extensive analysis on the effect of the boundaries. For the Fourier analysis we assume that a certain function f can be decomposed using expression (2.12) to calculate its Fourier coefficients and the exact derivative of f satisfies equation (2.13). To characterise the error of a particular discretisation, the Fourier coefficients generated by the differencing scheme are compared with the coefficients of the exact solution. Since these methods are linear, we only need to consider the differentiation of one of the terms of the summation, $\exp(ik_q x)$. For instance, the first derivative of the second order central difference scheme produces

$$\begin{aligned}
\mathcal{F}\left(\frac{\partial f}{\partial x}\right) &\approx \mathcal{F}\left(\frac{f(x+\Delta x) - f(x-\Delta x)}{2\Delta x}\right) \\
&= \sum_q \frac{\exp\left(ik_q(x+\Delta x)\right) - \exp\left(ik_q(x-\Delta x)\right)}{2\Delta x}\hat{f}(k_q) \\
&= \sum_q i\frac{\sin(k_q\Delta x)}{\Delta x}\exp(ik_q x)\,\hat{f}(k_q) \\
&= \sum_q i\tilde{k}_q \exp(ik_q x)\,\hat{f}(k_q),
\end{aligned} \tag{2.20}$$

where $\tilde{k}_q = \sin(k_q\Delta x)/\Delta x$ is the modified, or effective, wavenumber. Figure 2.3 portrays the modified wavenumber for second order finite difference scheme and fourth order finite difference scheme, compared to the exact solution. Spectral schemes reproduce all modes at the correct wavenumber, but neither Fourier nor Chebyshev series, the most common spectral methods, are suitable for representing the non-homogeneous direction of our simulations. For both finite

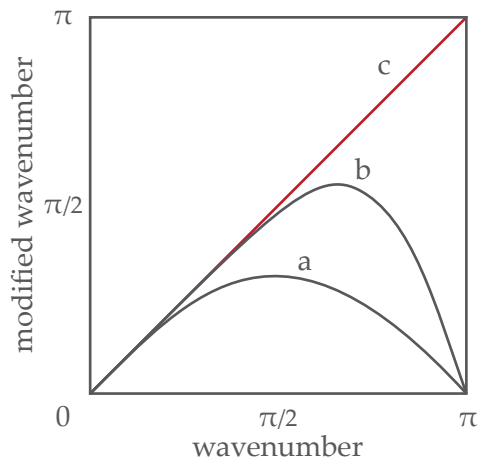

Figure 2.3.: Modification in the wavenumber produced by the the numerical discretisation: (*a*) second order central finite difference scheme, (*b*) fourth order compact finite difference scheme, (*c*) exact solution. Adapted from Lele (1992).

and compact differences, low frequencies are well represented while high frequencies are not correctly captured. To capture all scales, we must increase the resolution such that the smallest scales in the flow are still large with respect to the grid and can be adequately resolved.

2.3.3. The wall-normal collocated grid

While spectral methods usually prescribe the position of their collocation points and therefore the grid to be implemented, other discretisations allow for the grid to be adapted based on the needs of the problem. Along the wall-normal direction, where a finite difference method is used, variables are discretised on a grid that can either be a collocated or a staggered grid. In collocated grids, there is a single grid used for all variables, so the three velocity components and pressure are known at the same positions in space. In a staggered grid, there are several grids which allow variables to be defined at different positions in space. Each approach presents its advantages and disadvantages. In our case, the variables are represented in a collocated grid, where all variables are defined at the same points. This choice simplifies the representation of the rough surfaces with the immersed boundary method. However, it has an important drawback, the chequerboard effect (Ferziger and Perić, 2002), which is a typical problem when

using finite differences on collocated grids. Let us take for instance the second order central difference of a variable f, along y, on an equispaced grid of spacing Δy. The first and second derivatives are

$$f'_i \approx \frac{f_{i+1} - f_{i-1}}{2\Delta y}, \qquad f''_i \approx \frac{f'_{i+1} - f'_{i-1}}{2\Delta y} = \frac{f_{i+2} - 2f_i + f_{i-2}}{(2\Delta y)^2}. \tag{2.21}$$

We observe that while the first derivative is computed using adjacent values, the second derivative uses values two points apart, skipping the adjacent ones. This omission decouples values in even and odd points. The pressure is solved by inverting a laplacian operator that includes such second order derivatives. The pressure evaluated at even and odd points would be solved independently giving rise to two unconnected solutions, resulting in discontinuities in the pressure. This is the so-called chequerboard effect and is a source of numerical instability. To address this problem, incompressibility is weakly enforced (Nordström et al., 2007) using a divergence free formulation. The strategy proposed by García-Mayoral (2011) is to replace the continuity equation (2.1b) for an evolution equation that continuously and exponentially drives $\nabla \cdot \boldsymbol{u}$ to zero,

$$\frac{\partial \mathbb{D}}{\partial t} = -\lambda_D \mathbb{D} + \frac{1}{Re_D} \nabla^2 \mathbb{D}, \tag{2.22}$$

where λ_D and Re_D are parameters of this particular method and $\mathbb{D} = \nabla \cdot \boldsymbol{u}$. This creates communication between even and odd points allowing the use of a collocated grid, while removing the chequerboard effect (García-Mayoral, 2011). At a given time-step of size Δt, the parameters λ_D and Re_D are chosen in order to preserve the stability of equations (2.7),

$$\lambda_D = \frac{0.8}{\Delta t}, \tag{2.23}$$

$$Re_D = \frac{20\Delta t}{7} \left(\frac{\pi^2}{\Delta x_{min}^2} + \frac{4}{\Delta y_{min}^2} + \frac{\pi^2}{\Delta x_{min}^2} \right). \tag{2.24}$$

García-Mayoral (2011) shows that the resulting $\mathbb{D}$ in the flow is never larger than $2 \cdot 10^{-4}$ and it is much smaller than other velocity gradients in the flow, for instance, the magnitude of the vorticity $|\omega^+| \approx 0.05$–0.2.

2.3.4. The multi-block approach

In the core of the flow, away from the walls, the resolution is determined by turbulence and the characteristic size of its smallest eddies. However, near the walls, roughness induces a flow with a characteristic length scale of the order of the roughness size. In the roughness sublayer, the most constraining of these two resolutions is chosen to correctly resolve both the turbulent structures and the roughness-induced flow. Unfortunately, for the small roughness studied in this work, the roughness size is always the limiting factor. As a result, the number of points, n_x and n_z, increases to resolve the flow around roughness elements, with turbulence being over-resolved. Using this spacing in the whole domain would increase dramatically the computational cost. To circumvent this issue, the strategy adopted is to implement a multiblock approach, in which the grid is split into three blocks or bands with different resolutions (García-Mayoral, 2011). The upper and bottom blocks, which include the roughness elements and the roughness sublayer, have a higher number of points in x and z to capture the flow physics and the geometry, while the middle block uses a coarser mesh to alleviate the computational cost.

The original implementation developed by García-Mayoral (2011) only introduced this technique in the spanwise direction, as riblets, being two-dimensional roughness, do not need a finer resolution along the streamwise direction. Additionally, since the geometry along the streamwise direction is homogeneous, the immersed boundary conditions that define the geometry of the surface can be imposed in Fourier space, granting spectral resolution. In this work, to address three-dimensional roughness, the multi-block implementation is extended to the streamwise direction. As well as, the boundary conditions are all imposed in physical space. These changes affect the data structure as depicted in figure 2.6.

At the interface between bands, a boundary condition is needed. High frequencies are strongly damped by viscosity and decay quickly as they evolve away from the wall, hence a reasonable boundary condition at the interface is to set to zero all high frequencies that are not computed in the middle block (García-Mayoral, 2011). Figure 2.4 shows how high frequency Fourier modes,

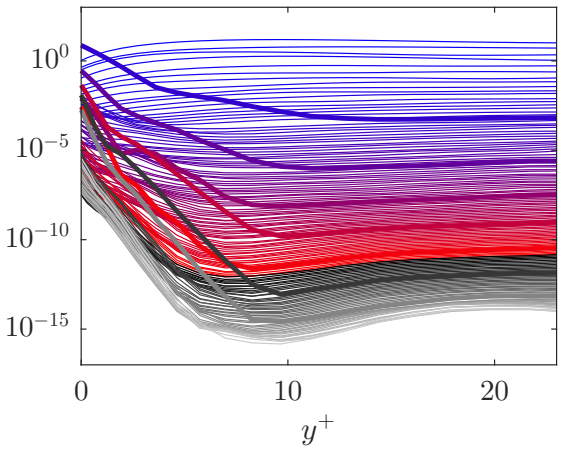

Figure 2.4.: Decay of the streamwise spectral energy, $\hat{u}^{+2}$, for case C15 (see section 2.6), along the wall-normal direction, with individual wavelengths along $\lambda_z = \lambda_x$. From blue to red, modes for increasing wavelengths that are present in the coarse and the fine grid blocks. From black to light grey, modes that are only present in the fine grid block. Thicker lines indicate the texture wavelength and its subharmonics.

those not included in the middle block, are negligible at the interface. These modes exhibit the same behaviour at the interface as intermediate frequency ones that continue through the interface, suggesting that the boundary condition at the interface is not artificially affecting the flow.

2.3.5. Spatial resolution

The size of the domain is chosen so that the physics of large structures is correctly described and captured (Flores and Jiménez, 2010). Therefore, as suggested by Lozano-Durán and Jiménez (2014), the length and width are $L_x \approx 2\pi\delta$ and $L_z \approx \pi\delta$, in the streamwise and spanwise directions, respectively. The wall-normal coordinate is non-uniform in y, in order to capture all turbulent scales at a minimum computational cost. The grid is coarser in the centre of the channel, finer near the walls, and remains almost constant within the immersed boundary region. The number of grid points and the stretching of the wall-normal coordinate are chosen to provide DNS resolution (Moser et al., 1999), resolving all relevant turbulent scales (Moin and Mahesh, 1998). The wall-parallel grid spacings used are $\Delta x^+ \approx 8$ and $\Delta z^+ \approx 4$. Outside the roughness region,

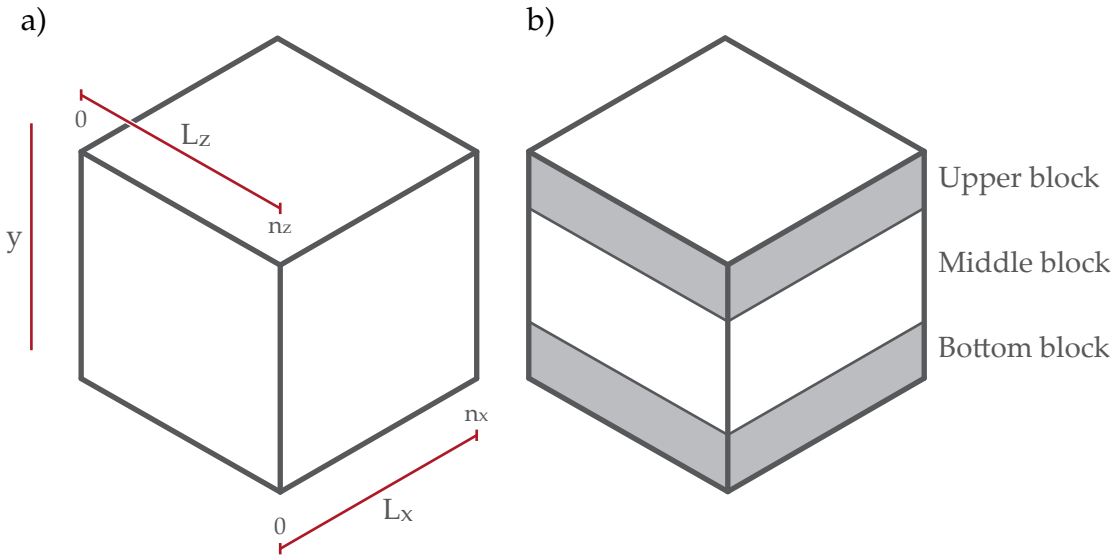

Figure 2.5.: (*a*) Dimensions of the computational domain in physical space. (*b*) The three bands or blocks in which the domain is split.

the minimum wall-normal grid spacing is $\Delta y^+_{min} \approx 0.3$ at the roughness crests and progressively grows to the maximum spacing $\Delta y^+_{max} \approx 3.1$ at the centre of the channel. Within the roughness region, i.e. between roughness crests and troughs, the grid spacing is kept almost constant and approximately equal to Δy^+_{min}. The resolution along x and z is better than that used in Kim et al. (1987) and is comparable to the simulations by Moser et al. (1999). Since in those cases the non-homogeneous direction is discretised using different schemes to ours, the wall-normal resolution is not directly comparable, but we still achieve the objective of resolving the smallest structures (Moin and Mahesh, 1998).

The physical domain is defined by the lengths L_x, L_z, δ and the depth of the roughness in the y-direction; and by the number of grid points n_x, n_y and n_z where the variables are defined. The number of grid points in x and z may vary between different blocks due to the multi-block approach. Figure 2.5 shows the relevant characteristics of the physical domain. The upper and bottom blocks include the immersed boundary with the roughness texture. The number of grid points along the y coordinate is defined so that we obtain DNS resolution in the fluid region of height 2δ. Subsequently, the numerical box is extended below the roughness crests to accommodate the immersed region with the roughness

elements. The resulting total height of the box is $2(\delta + k)$, and the number of grid points depends on the particular roughness height.

In physical space, the domain is a cuboid with three blocks, where each can have a different number of points, n_x and n_z. The spacing is adjusted in each block to cover the whole domain with the available points. However, when transformed to Fourier space, this difference in grid points results in a different number of wavenumbers representing each block. If we use a similar representation to figure 2.5, aligning the wavenumbers of all three blocks, the domain would not necessarily resemble a cube any longer. Modes are aligned based on their wavenumber, i.e. the k^{th} mode will always represent the same information regardless of the total number of modes or collocation points in the original grid. To illustrate this, figure 2.6 depicts a domain with a larger number of wavenumbers in the wall blocks than in the core block. The physical domain is first transformed along the x direction and afterwards along z. The first transformation, depicted in figure 2.6(*a*), takes as arguments real numbers, which results in pairs of complex conjugates. Half of the data is redundant and thus only half of the modes are needed to reconstruct the entire data. Regarding the second Fourier transform along z, typically the coefficients of the Fourier transform are not stored consecutively, but in the series $[0, 1, ..., N/2 - 1, -N/2, ..., -2, -1]$, where N is the number of grid points in that particular block and direction. Therefore the middle block, with fewer high wavenumbers, is shorter in the streamwise direction and displays a spanwise central hole, as portrayed in 2.6(*b*).

To improve the computational efficiency, the pseudo-spectral domain is split into regions that can be calculated independently on parallel computers and with similar computational load per processor. Transferring data between processors is one of the most time-consuming operations and should be minimised. In physical space, data is stored in xz-planes, so two-dimensional Fourier transforms can be performed without communicating with other processors. These xz-planes are grouped together and sent to the processors in sets of similar computational cost. Since the density of grid points may differ between blocks, the computational cost is estimated by the number of points per plane, which is in principle correlated with the amount of operations needed. Similarly, in Fourier space, modes are grouped together and distributed among the processors.

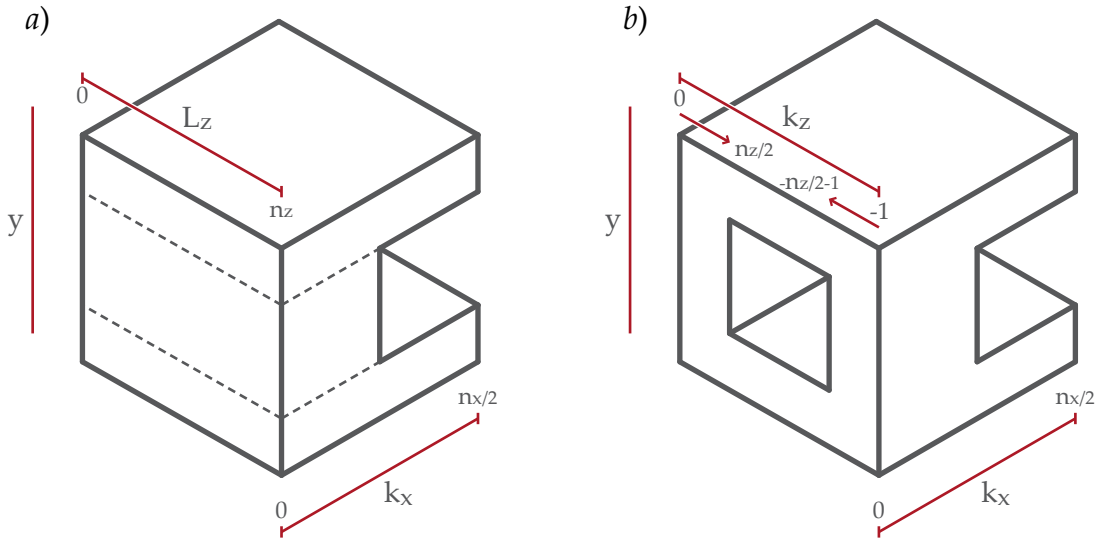

Figure 2.6.: Representation of the spectral domain (*a*) after the first Fourier transform along the x direction, and (*b*) after both Fourier transforms along the x and z directions. The middle block presents fewer points than the wall blocks in both directions.

Modes are independent, therefore, processors can perform the wall-normal derivatives without additional communication. As illustrated in figure 2.7, two types of modes are possible, those present in all three blocks, which extend the whole domain from top to bottom; and those only present in top and bottom blocks. These two types of modes have different computational load and are grouped and calculated independently. This division of the calculation into two steps improves the balancing of the computational load. In the original implementation, in spectral spaces, the data representing Fourier modes is first grouped in sets with equal streamwise wavenumber, and afterwards distributed. In this work, to improve efficiency, the data structure was modified to be able to distribute these Fourier modes independently of their wavenumbers.

2.4. Immersed boundary method

The spatial discretisation and temporal integrator have been described above. Now we introduce the strategy to simulate arbitrary rough geometries at the walls. An immersed boundary method is chosen to simulate the roughness geo-

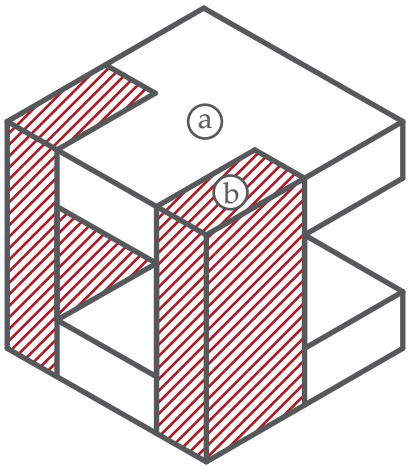

Figure 2.7.: Regions in which the pseudo-spectral domain is split. (*a*) Short columns, only spanning across the fine grid blocks. (*b*) Long columns, spanning the entire channel.

metry (Mittal and Iaccarino, 2005). The main advantage of this family of methods is that they can be implemented on Cartesian grids. Compared to other approaches, this greatly simplifies the grid generation process as well as the spatial discretisation of the equations. In particular, the technique implemented is the one proposed by Mohd-Yusof (1997), Fadlun et al. (2000) and Iaccarino and Verzicco (2003), which uses body forces to simulate the presence of a solid body, reproducing the no-slip condition at the walls of the roughness elements. Intuitively, the condition to implement is

$$\boldsymbol{u}_{\text{solid}}^{n+1} = \boldsymbol{V}, \tag{2.25}$$

where $\boldsymbol{V}$ is the appropriate velocity of the solid body at the forcing points. Expression (2.25) is implemented by modifying the right-hand-side in equation (2.7a) at points representing a solid body. Following Mohd-Yusof (1997), this method yields

$$\left(1 - \Delta t \frac{\beta_{i_{RK}}}{Re} L\right) \boldsymbol{u}_{i_{RK}}^{n} = \left(\boldsymbol{V}_{i_{RK}-1}^{n} - \boldsymbol{u}_{i_{RK}-1}^{n}\right) + \left(1 - \Delta t \frac{\beta_{i_{RK}}}{Re} L\right) \boldsymbol{u}_{i_{RK}-1}^{n}. \tag{2.26}$$

If a solid–fluid boundary crosses through points of the grid, the forcing velocity at those points is $\boldsymbol{V} = 0$. However, if the boundary falls between two points, as it would most likely be the case in arbitrary roughness, we are forced to use more elaborated expressions for $\boldsymbol{V}$. This is inevitably the case when the rough-

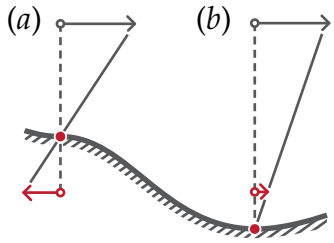

Figure 2.8.: (*a*) Extrapolation and (*b*) interpolation triangular schemes. The grey arrow is the velocity calculated using Navier–Stokes equations, the red arrow is the velocity imposed in order to satisfy the no-slip condition at the boundary.

ness elements have inclined, or curved shapes, such as spheres or pyramids, or when a staggered grid is used. García-Mayoral (2011) proposed a strategy combining the methods by Fadlun et al. (2000) and Iaccarino and Verzicco (2003), whose main idea is illustrated in figure 2.8(*a*). The boundary is implemented by taking the solid and fluid points closest to the boundary, and imposing a velocity $\boldsymbol{V}$ onto the solid point such that the resulting velocity at the boundary is zero (Iaccarino and Verzicco, 2003). If this boundary is relatively too close to the fluid grid point, the extrapolation to the solid point produces large weight coefficients of $\boldsymbol{V}$, that can cause numerical stability issues (Tseng and Ferziger, 2003). In these cases, an interpolation method (Fadlun et al., 2000) is more appropriate, as depicted in figure 2.8(*b*). This method has the notable inconvenience of applying momentum within the flow field, i.e. the Navier–Stokes equation is not solved at those points but instead an extrapolation from the surrounding points.

To obtain $\boldsymbol{V}$ in a two-dimensional geometry, two neighbouring fluid nodes are commonly used, and three in a three-dimensional case. For two-dimensional geometries, figure 2.9 illustrates how to obtain the point on the boundary that is closest to the solid point where the extrapolation is performed. This auxiliary point is used to calculate the weight of the extrapolation for $\boldsymbol{V}$. The extension to the three-dimensional case follows a similar procedure.

Obtaining the body force $\boldsymbol{V}$ relies heavily on the geometry, and is therefore calculated in physical space, alongside with the advective terms. Additionally, a two-dimensional convolution would need to be performed to impose such boundary condition in spectral space, which would dramatically increase its

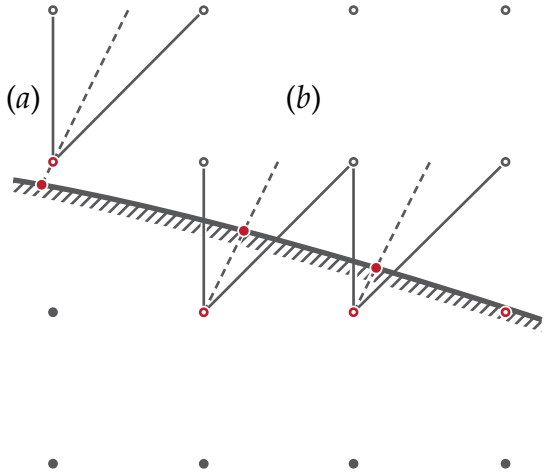

Figure 2.9.: Two-dimensional (*a*) interpolation and (*b*) extrapolation triangular schemes using two neighbours. Grey solid points are solid nodes, grey empty points are fluid points where the velocity is known and red empty points are the points where the forcing is imposed. The red points on the boundary are calculated using the inter/extrapolation schemes. Adapted from García-Mayoral (2011)

computational cost.

As mentioned before, the original implementation for riblets took advantage of the two-dimensional geometry, so the immersed boundaries were applied in physical space along the spanwise direction, and in Fourier space along the streamwise direction. In this work, the implementation was extended to address three-dimensional roughness, where immersed boundary conditions are fully applied in physical space.

The triangulation described has second order accuracy, matching the overall order of the implementation, and as a result the boundary is appropriately captured (Fadlun et al., 2000). On the other hand, this method presents some disadvantages. First, solid points are part of the computational domain, increasing the total computational cost. It is also an explicit technique, and therefore approximate. At the end of a time-step the velocity at the immersed boundary cannot be ensured to be exactly zero, since the forcing is imposed using the velocity at the previous time-step. This generates a residual non-physical flow within the solid elements. Figures 2.10 and 2.11 show the ensemble average and an instantaneous realisation of the u and v components of this residual flow in-

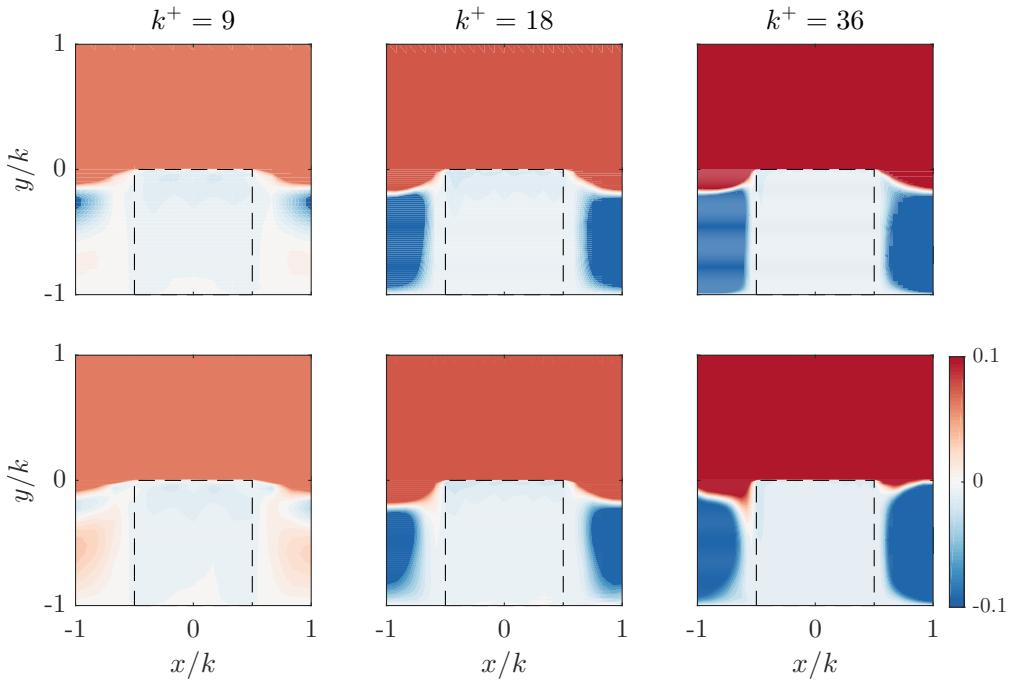

Figure 2.10.: Streamwise velocity component, u, across the centreline of a post at constant streamwise coordinate. From left to right, increasing post size, $k^+ = 9$, 18 and 36, cases C09, C18 and C36 (see section 2.6). The top line displays the ensemble time average. The bottom line displays an instantaneous realisation.

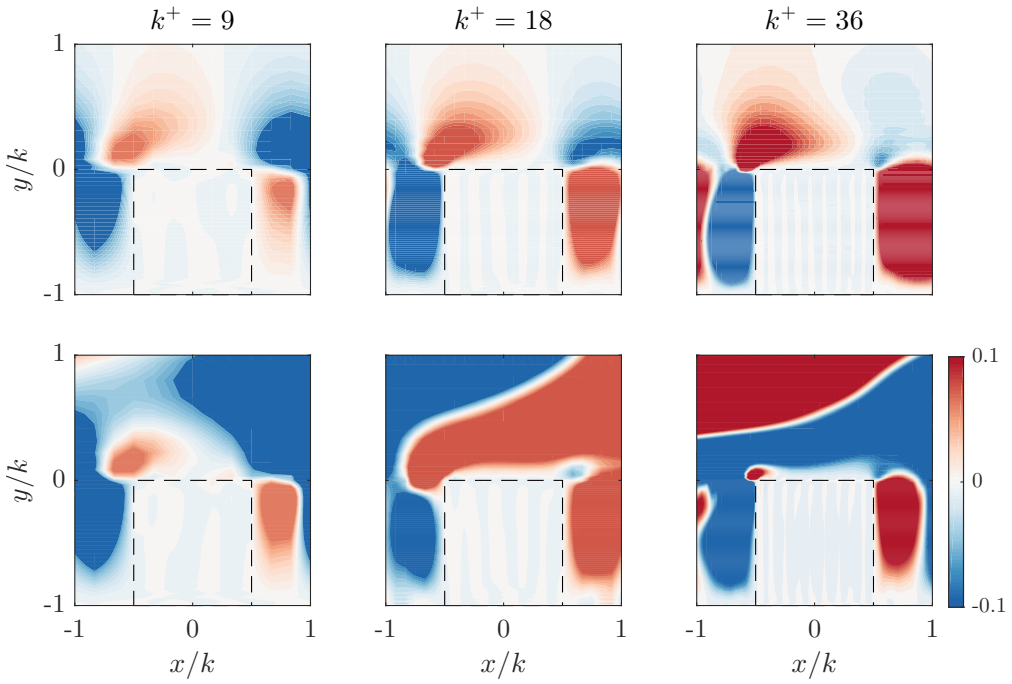

Figure 2.11.: Wall-normal velocity component, v, across the centreline of a post at constant streamwise coordinate. From left to right, increasing post size, $k^+ = 9$, 18 and 36, cases C09, C18 and C36 (see section 2.6). The top line displays the ensemble average. The bottom line displays an instantaneous realisation.

side a roughness element for different roughness heights. This flow, although non-desirable, is negligible and the value inside the solid remains under $0.1u_\tau$.

In some simulations we have observed the appearance of the Gibbs phenomenon, which is highly related to the way the immersed boundaries are imposed. The sudden alternations from fluid points, with an non-zero velocity, to solid points, with an enforced zero velocity, are prone to this problem when treated spectrally. These discontinuities are characterised by a relatively high energy in the high wavenumbers. Consequently, when the series is truncated, spurious high-frequency waves appear in the immersed boundary region, especially just above the tips in the streamwise direction as the velocity gradients are more intense. Like the aforementioned spurious flow, this phenomenon is also bounded to small values and, due to its high wavenumber, they are heavily damped by viscosity. This phenomenon is inherent to the choice of spectral methods combined with discrete boundary conditions, however some measures can be undertaken in order to minimise its impact. While increasing the resolution alleviates this problem; it, unfortunately, does not completely eliminate it. A possible solution could have been the use of a Fourier continuation method (Lyon and Bruno, 2010). This approach extends the function within the geometry, removing the discontinuities while maintaining the no-slip velocity at the boundaries of the roughness elements. However, the challenge then becomes to find a computationally efficient process to obtain expressions for all three velocity components, and the pressure while at the same time satisfying the continuity equation.

2.5. Validation

The numerical methodology presented in this work was originally developed and validated by García-Mayoral (2011). In particular, the implementation was validated for a smooth-wall channel, the transition of the wake behind a cylinder, and triangular riblets. As an example, figure 2.12 shows that one-point statistics over a smooth-wall channel agree well with the results by Moser et al. (1999). We also conducted a smooth-wall test case in which a solid region of 12 wall units below the surface was simulated using the immersed boundary method. These results agree with those by Moser et al. (1999). The inset in figure 2.12 shows

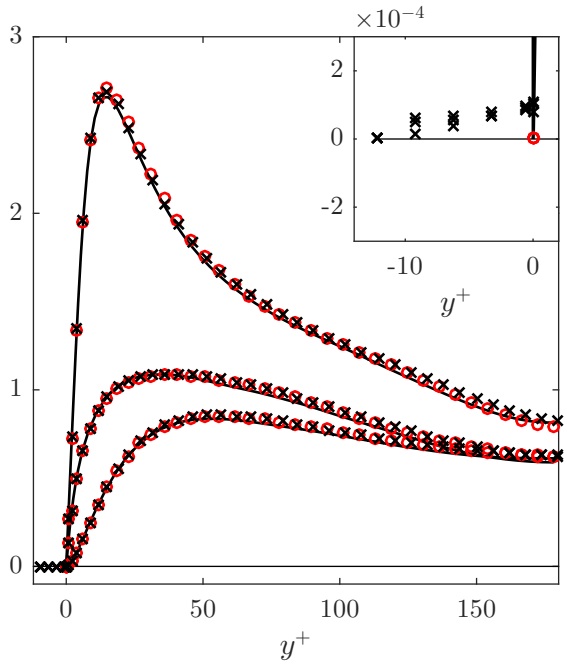

Figure 2.12.: Root-mean-square fluctuations of the velocity components. Comparison between: —, $Re_\tau = 180$ results from Moser et al. (1999); ○, smooth-wall results; and, ×, smooth-wall using 12 wall units of immersed boundary to simulate the wall.

that the fluctuations within the immersed region are negligible. The immersed boundary method adequately drives to zero the velocity and its fluctuations.

The velocity field across a solid element in a rough geometry formed of cube posts is shown in figures 2.10 and 2.11. These figures show that the mean ensemble average velocity within solid elements is negligible. The maxima of both the streamwise and wall-normal velocities are smaller than $0.1u_\tau$, and much smaller than the surrounding velocity. The instantaneous velocity displays the same behaviour with negligible velocity within the solid element.

2.6. Numerical experiments

In this work, we explore the transitionally rough regime. The goal is to understand and predict the effect of roughness on turbulent flows. To explore the transitionally rough regime, we conduct a campaign of direct numerical sim-

ulations of turbulent channel flows with rough walls. The channels are symmetric, with roughness on both walls. Four different geometries are considered, as depicted in figure 2.13. To explore the behaviour of each geometry, the size of the roughness elements, k, is scaled while their shape is kept fixed to a constant value, also resulting in constant solidity and effective slope. These surfaces exhibit the classic k-roughness behaviour, which is characteristic of most three-dimensional rough surfaces. The main characteristics of the simulations can be found in table 2.2.

All geometries are generated by repeating a pattern. The unit element is a cube of side k, repeated along x and z on both walls. These unit elements are described using 12×12 points for the cases with $k^+ \lesssim 9$, 24×24 points for the cases with $12 \lesssim k^+ \lesssim 25$, and 48×48 points for case $k^+ \approx 36$. This choice results from the need to solve both the turbulent scales as well as the flow around the roughness elements, while keeping a moderate computational cost. The simulations carried out by Thakkar et al. (2018) on random roughness, performed using a 12 point-per-element discretisation, are in good agreement with experimental results. In most of our cases, each individual cube element on the rough surface is represented by 24×24 points in the wall-parallel directions. For the smallest cases, $k^+ \lesssim 9$, the number of points is reduced to 12×12 per element to reduce the computational cost. Figure 2.14 shows that one-point statistics are not affected by this change in resolution.

The simulations are conducted at constant mass flow rate, which is adjusted to achieve a friction Reynolds number $Re_\tau \approx 180$ for all simulations. The length-scale used to calculate Re_τ is $\delta' = \delta + \ell_U$, where ℓ_U is the virtual origin of the mean velocity profile. The height ℓ_U is the depth where the mean velocity profile appears to vanish. It will be shown in chapter 4, that in our roughness the value ℓ_U is of the same order of the displacement height as defined by Jackson (1981). The displacement height adjusts the reference level for the velocity profile to the height at which the mean surface shear appears to act. In the transitional regime of the roughness surfaces studied, the apparent origin of the mean velocity profile and apparent plane where the shear acts are approximately equal. The friction velocity u_τ is therefore defined at that height, by extrapolating the total shear stress to δ'.

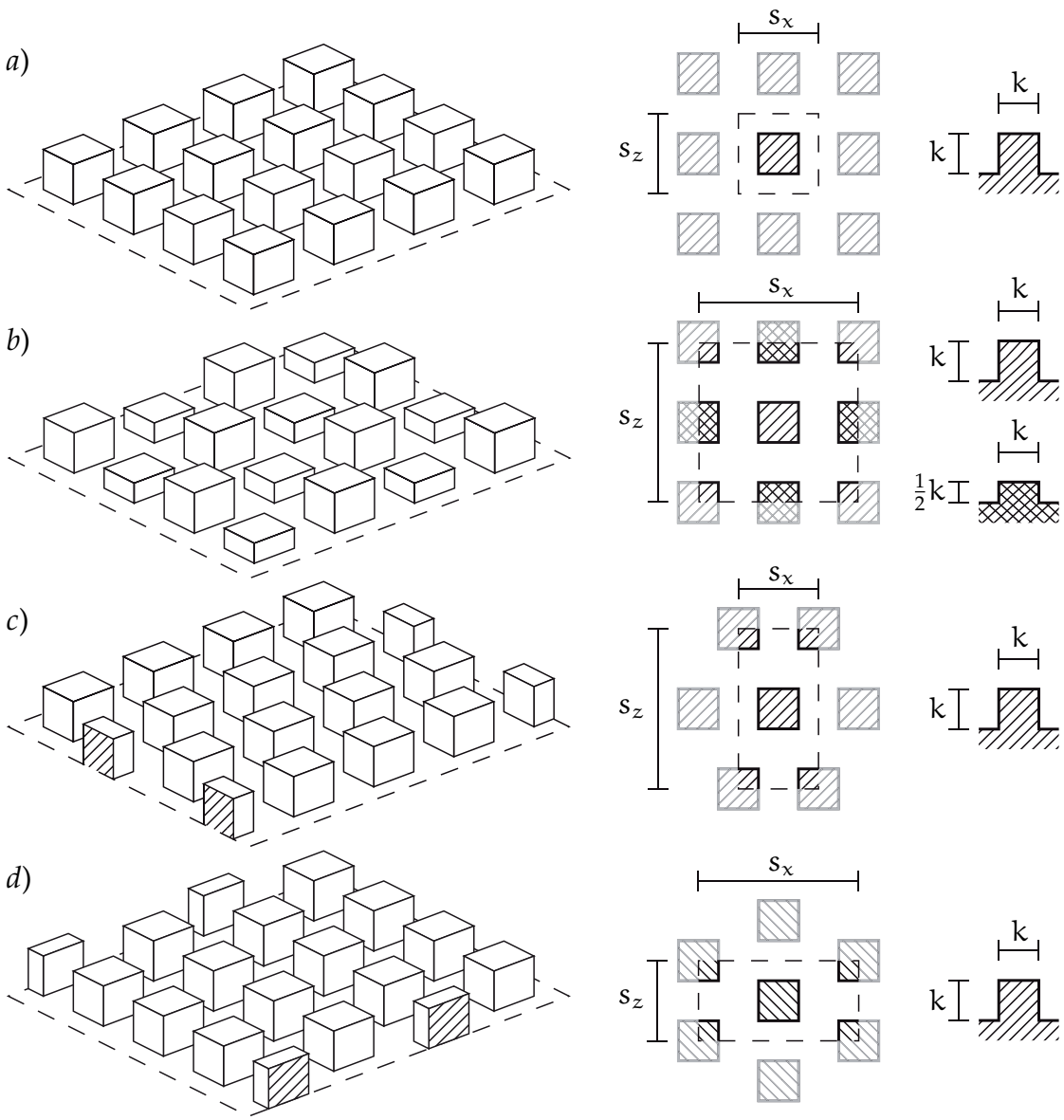

Figure 2.13.: Schematic of (*a*) the collocated, (*b*) the collocated two heights, (*c*) the spanwise staggered and (*d*) the streamwise staggered texture patterns. The mean flow is from bottom left to top right. Left panels, three-dimensional representation of the roughness surface; middle panel, top view of a unit element of the pattern; right panels, side view of an isolated post.

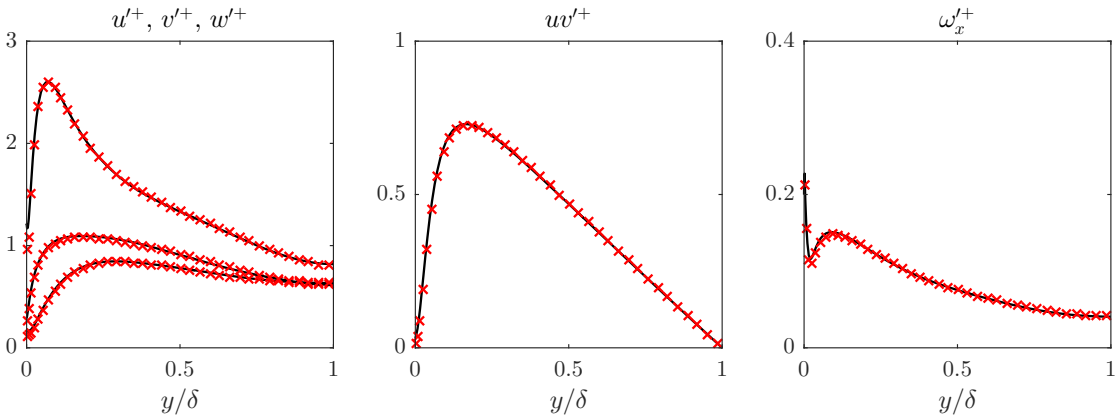

Figure 2.14.: Root-mean-square fluctuations of the velocity components, Reynolds shear stress and streamwise vorticity component. —, case C12, with 24×24 point resolution; ×, equivalent to case C12 with the resolution halved, 12 × 12 points per unit element.

Statistics are collected for a long enough period to ensure statistical convergence. The characteristic time scale of the largest and long-lasting eddies in the flow is of order δ/u_τ. Starting with an already turbulent flow field, statistically converged initial conditions are obtained by simulating and discarding the flow during at least $10\delta/u_\tau$. Statistics are then collected over at least $15\delta/u_\tau$.

2.7. Summary

In this chapter, we have presented the numerical method used in this study to simulate turbulent flows over rough walls. The methodology, initially developed by García-Mayoral (2011), presents some novelties with respect to other simulations in literature. Spectral methods on rough walls are seldom used. The development of the multiblock technique (García-Mayoral, 2011) allows the decoupling of the resolution in the core of the channel and the roughness sublayer, which greatly improves the performance.

While in this work the methodology closely follows that in García-Mayoral (2011), our particular implementation had to be extended to represent fully three-dimensional roughness. The main modification are those in the immersed boundary routines and roughness geometry generation. The data structures were also

	Case	s_x/k	s_z/k	δ/k	k^+	k_s^+	ΔU^+	Re_τ
Smooth Channel	SC	—	—	—	0.0	0.0	0.0	183.9
Collocated	C06	2	2	30.6	6.0	9.6	0.5	183.9
	C09	2	2	20.4	8.8	14.1	0.7	180.8
	C12	2	2	15.4	11.7	18.7	1.5	180.0
	C15	2	2	12.3	14.4	23.1	2.4	178.7
	C18	2	2	10.3	17.4	27.8	3.5	179.0
	C24	2	2	7.7	22.5	36.0	4.7	174.5
	C36	2	2	5.2	35.7	57.2	6.7	186.7
Collocated two heights	CC06	4	4	30.7	5.8	—	0.8	178.7
	CC09	4	4	20.6	8.7	—	1.8	179.8
	CC12	4	4	15.5	11.7	—	3.3	182.6
	CC15	4	4	11.7	15.4	—	4.5	180.1
	CC18	4	4	10.4	17.0	—	4.9	176.7
Spanwise staggered	SZ06	2	4	30.6	5.9	—	0.4	183.0
	SZ09	2	4	20.4	8.9	—	0.9	182.7
	SZ12	2	4	15.4	11.8	—	1.6	181.8
	SZ15	2	4	11.6	16.2	—	3.2	188.3
Streamwise staggered	SX06	4	2	30.6	5.9	—	0.6	181.6
	SX09	4	2	20.4	8.8	—	1.2	179.5
	SX12	4	2	15.4	11.9	—	2.6	183.1
	SX15	4	2	11.5	16.0	—	4.1	185.3
	SX18	4	2	10.3	17.6	—	4.3	180.6

Table 2.2.: Main characteristics of the simulations. The characteristic size of the roughness elements is k, and the streamwise and spanwise pitches of the pattern are s_x and s_z. The half-height of the channel, measured from the roughness crests, is denoted by δ.

modified to improve performance.

Our numerical experiments implement a three–sub-step Runge–Kutta time integrator with a divergence-free formulation for continuity, where the wall-parallel coordinates are discretised using dealiased Fourier expansions and the wall-normal direction implements second order central finite difference. Equations (2.7) and (2.22) then yield

$$\left(1-\Delta t\frac{\beta_{i_{RK}}}{Re}L\right)\boldsymbol{u}^n_{i_{RK}} = \boldsymbol{u}^n_{i_{RK}-1} \tag{2.27a}$$
$$+\Delta t\Big(\frac{\alpha_{i_{RK}}}{Re}L\left(\boldsymbol{u}^n_{i_{RK}-1}\right)-\gamma_{i_{RK}}N\left(\boldsymbol{u}^n_{i_{RK}-1}\right)$$
$$-\zeta_{i_{RK}}N\left(\boldsymbol{u}^n_{i_{RK}-2}\right)-\left(\alpha_{i_{RK}}+\beta_{i_{RK}}\right)G\left(p^n\right)\Big),\quad i_{RK}=1,2,3$$
$$\mathbb{D}^{n+1} = \mathbb{D}^n+\Delta t\mathbb{F}\left(\mathbb{D}^n+\frac{\Delta t}{2}\mathbb{F}\left(\mathbb{D}^n\right)\right), \tag{2.27b}$$
$$DG\left(\phi^{n+1}\right) = -\frac{1}{\Delta t}\left(\mathbb{D}^{n+1}-D\left(\boldsymbol{u}^n_3\right)\right), \tag{2.27c}$$
$$p^{n+1} = p^n+\phi^{n+1}, \tag{2.27d}$$
$$\boldsymbol{u}^{n+1} = \boldsymbol{u}^n_3-\Delta tG\left(\phi^{n+1}\right). \tag{2.27e}$$

where $\mathbb{F}$ is the discretised right-hand-side of equation $\mathbb{F}\left(\mathbb{D}\right)=-\lambda_D\mathbb{D}+1/Re_DL\left(\mathbb{D}\right)$ that is introduced in section 2.3.

Although this numerical method is efficient, further improvements could still be made if it is extended in the future. The use of a staggered grid for the wall-normal direction would allow us to discard the divergence-free continuity equation. This method was only implemented to resolve the chequerboard effect, which does not arise in staggered grids. However, the implementation of the immersed boundary method would become more complex. Another possible improvement is the use of finite differences of higher order or compact differences to discretise the wall-normal direction. Those discretisations require a higher number of operations to be performed, but it would allow a reduction in the number of grid points. This generally results in an overall reduction of the computational cost. In the past, some direct numerical simulations have used Chebyshev series to discretise the wall-normal direction, providing spectral resolution (Kim et al., 1987; Del Álamo and Jiménez, 2003). However, since the

distribution of the collocation points cannot be altered, a fine resolution to solve all scales in the core of the channel gives rise to an excess of planes near the walls, consequently increasing unnecessarily the cost.

3. Flow decomposition

Part of the content of this chapter has been published in N. Abderrahaman-Elena and R. García-Mayoral (2016). 'Geometry-induced fluctuations in the transitionally rough regime'. J. Phys. Conf. Ser. *708.*
Part of the content of this chapter has been published in N. Abderrahaman-Elena et al. (2019). 'Modulation of near-wall turbulence in the transitionally rough regime'. J. of Fluid Mech. *865, pp. 1042–1071.*

In this chapter, we propose that turbulent flows over rough surfaces can be thought of as formed of two components. The background turbulent-like component, which in principle does not contain the footprint of roughness, captures the turbulent characteristics of the flow. The other component, induced by roughness, is coherent with the surface texture, and its amplitude is modulated by the overlying turbulent-like contribution. We study how to extract this two contributions from the full signal, and explore them separately to analyse the changes that roughness produces on the turbulent flow.

3.1. Flow decomposition

In the proximity of the wall, roughness induces fluctuations that alter, and even destroy, the near-wall cycle (Jiménez, 2004). The intensity of these fluctuations decreases exponentially away from the surface, and they are generally considered to be confined within a region near the wall of height $\sim$ 3–5k, known as the roughness sublayer (Raupach et al., 1991; Flack et al., 2007). In this region the fluctuations induced by roughness cannot be neglected and their effect is noticeable in the flow. These roughness-coherent fluctuations are of the same order of

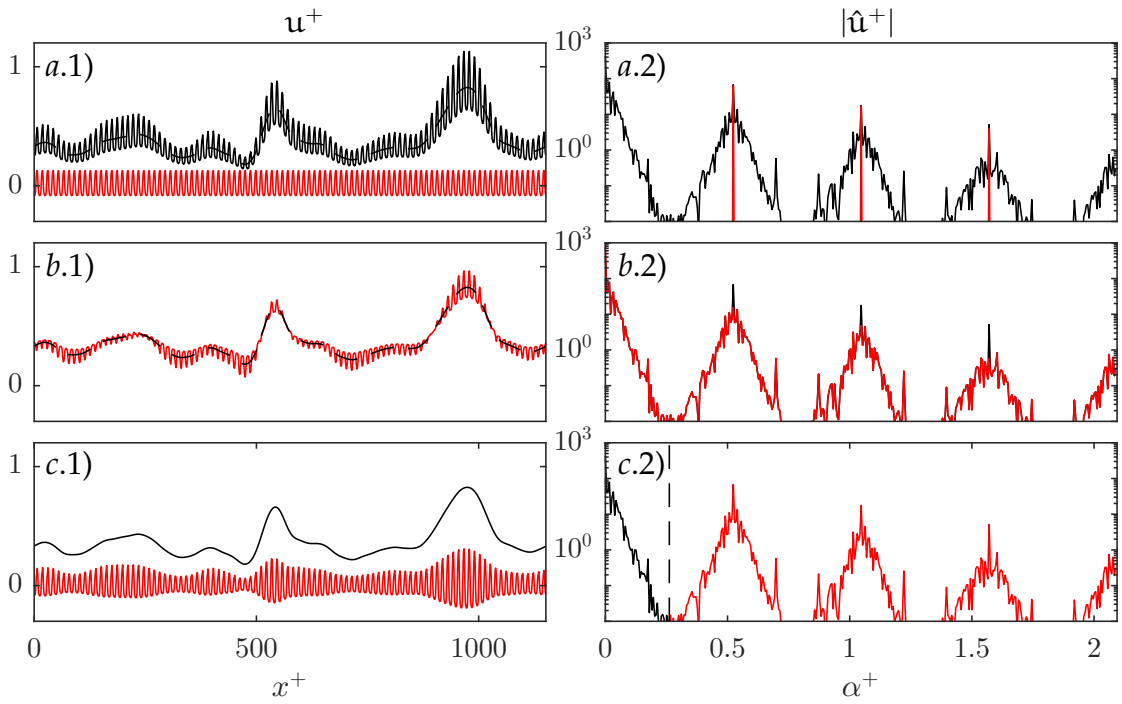

Figure 3.1.: Instantaneous realisation of the streamwise velocity, for case C06, at $y^+ = 0.3$, in a section of constant z^+ through the middle of a row of posts. (*a*.1) and (*a*.2) ——, full streamwise velocity; – –, background turbulent component; ——, ensemble average over time and over the relative position in the periodic unit of texture. (*b*.1) and (*b*.2) ——, full signal minus the ensemble average; – –, background turbulence. (*c*.1) and (*b*.2) ——, low-pass filtered full signal; ——, difference of the latter with the full signal. The left panels represent the signals in physical space, and the right panels in Fourier space, where α^+ is the wavenumber scaled in wall units.

magnitude as the background turbulence fluctuations, leaving their footprint on the velocity field and the energy spectrum.

In the roughness sublayer the flow can be thought of as formed of a roughness-coherent component, which is coherent in time and space with the roughness surface, and a background-turbulent component of a chaotic nature. This is analogous to the decomposition from Reynolds and Hussain (1974) into a coherent and a turbulent component. To illustrate this concept, figure 3.1(*a*.1) displays an instantaneous realisation of the streamwise velocity close to the roughness crests. We observe two contributions. The first, with longer wavelengths, has a characteristic length scale of the order of turbulent eddies. The second,

whose dominant wavelength is that of the roughness texture, smaller than the overlying eddies, can be obtained by ensemble averaging over time and over the relative position in the periodic unit of texture. If the roughness-coherent component is subtracted from the full velocity, as in figure 3.1(*b*.1), we observe that the footprint of the roughness elements does not completely disappear. The reason can be explained by means of their corresponding Fourier transform, shown in figures 3.1(*a*.2) and 3.1(*b*.2). The ensemble average is composed of the wavelength of the texture and its subharmonics. The full velocity exhibits these same wavelengths, induced by the texture; however, they are modulated in amplitude and thereby surrounded by energy in the neighbouring wavelengths. When the ensemble average is subtracted from the full velocity, the most energetic part, which corresponds to the wavelength of the texture and its subharmonics, is removed, but all the energy neighbouring these wavelengths is not, failing to remove the footprint as observed in figure 3.1(*b*.1). In figures 3.1(*c*.1) and 3.1(*c*.2) we set a threshold to identify what wavelengths correspond to background turbulence and thus what the remainder represents in physical space. The wavelengths are then divided into long and short ones. In figure 3.1(*c*.1), we observe that the contribution from long wavelengths closely resembles smooth-wall turbulence. Wavelengths shorter than those of turbulence are similar to the ensemble average, shown in figure 3.1(*a*.1), but they appear to be modulated in amplitude by the overlying, long-wavelength signal of the background turbulence.

Following the above analysis, in Abderrahaman-Elena and García-Mayoral (2016) we proposed that the flow over a roughness texture of small size is not simply the sum of the ensemble average plus a turbulent component. Instead, the roughness-coherent flow is modulated by the overlying turbulence. For a particular roughness size, inducing a coherent flow $u_{RC,u}$, and with a background turbulence u_{BT}, the instantaneous velocity can intuitively be modelled as

$$u \approx U + u_{BT} + \frac{U + u_{BT}}{U} u_{RC,u}, \tag{3.1}$$

where U is the temporal and x-z-spatial averaged streamwise velocity.

Equation (3.1) can also be inferred by considering small roughness in the vis-

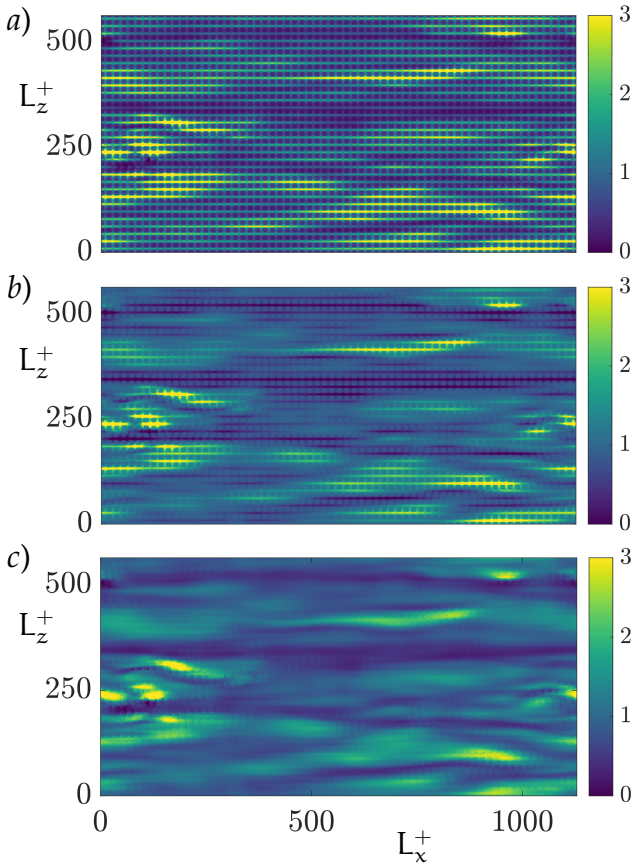

Figure 3.2.: Instantaneous streamwise velocity at $y^+ \approx 0.3$, for case C09. (*a*) Full signal. (*b*) Turbulent contribution obtained using the triple decomposition, $u - U - u_{RC,u}$. (*c*) Turbulent contribution obtained using equation (3.1). Mean flow from left to right.

cous limit. In the spirit of Luchini et al. (1991), the vanishingly small roughness limit reduces the problem to a shear driven, purely viscous flow, which results in a self-similar solution that scales with k and with the overlying shear, proportional to $U + u_{BT}$.

The triple decomposition proposed by Reynolds and Hussain (1974) is similar to equation (3.1) except for the amplitude modulation by $U + u_{BT}$. The triple decomposition has been widely used to characterise the texture-coherent flow in turbulence over a variety of complex surfaces (Choi et al., 1993; Jiménez et al., 2001; García-Mayoral and Jiménez, 2011; Jelly et al., 2014; Seo et al., 2015). However, if we are to study the modifications in the background turbulence, the

modulation of the roughness-coherent component needs to be accounted for. Figure 3.2(*a*) shows the streamwise velocity within the roughness layer, where the coherent signal of the roughness elements is strong. If the ensemble average, the roughness-coherent contribution, is subtracted we observe in figure 3.2(*b*) that, although reduced, the footprint of the surface texture remains. However, when we account for the modulation of the coherent flow, using equation (3.1), the signature of the roughness-coherent flow on the background turbulence is substantially weaker, as shown in figure 3.2(*c*).

The instantaneous overlying flow induces around roughness elements a velocity field with components in all three directions. At the same time, the background turbulent flow has components in all three directions, so for instance the spanwise background shear induces a texture-coherent cross-flow. Hence, the three velocity components have a roughness contribution induced by all components of the overlying flow. Let us take the streamwise velocity signal as an example. It would have contributions from the mean streamwise velocity, U, the background-turbulent streamwise component, u_{BT}, a roughness-coherent component, $u_{RC,u}$, driven and modulated by $U + u_{BT}$, and a roughness-coherent component, $u_{RC,w}$, driven and modulated by the background-turbulent spanwise component, w_{BT}. The simplified model presented in equation (3.1) can then be extended to all components of the full velocity,

$$u \approx U + u_{BT} + \frac{U + u_{BT}}{U} u_{RC,u} + \frac{w_{BT}}{\widetilde{w}} u_{RC,w} + \frac{v_{BT}}{\widetilde{v}} u_{RC,v}, \tag{3.2a}$$

$$w \approx \quad w_{BT} + \frac{U + u_{BT}}{U} w_{RC,u} + \frac{w_{BT}}{\widetilde{w}} w_{RC,w} + \frac{v_{BT}}{\widetilde{v}} w_{RC,v}, \tag{3.2b}$$

$$v \approx \quad v_{BT} + \frac{U + u_{BT}}{U} v_{RC,u} + \frac{w_{BT}}{\widetilde{w}} v_{RC,w} + \frac{v_{BT}}{\widetilde{v}} v_{RC,v}, \tag{3.2c}$$

where $u_{RC,w}$ is the roughness-coherent streamwise velocity induced by the overlying, background spanwise shear of w_{BT}, etcetera. Note that, while the modulating signal $U + u_{BT}$ is always positive, w_{BT} and v_{BT} can either be positive or negative, and due to symmetry, their mean values cancel out. To obtain a measure of the intensity of these components, $\widetilde{w}$ and $\widetilde{v}$ denote the conditional averages of w and v, which account for their mean direction over individual roughness elements, such that they are only included into the average when they are positive

(García-Mayoral and Jiménez, 2011). In the cube roughness geometries studied in this work we observe no significant flow induced by ν in the streamwise and spanwise directions, although the corresponding terms have been included in equations (3.2) for completeness. In textures with inclined planes, such as pyramids or cones, for instance, we would expect these contributions, $u_{RC,\nu}$ and $w_{RC,\nu}$, to be relevant. Figure 3.3 shows instances of all three velocity components and their corresponding turbulent contributions, obtained by removing the roughness-coherent terms according to equations (3.2). The present decomposition, accounting for the modulation of the overlying turbulence, reduces significantly the signature of the roughness-coherent flow. The remaining signature is overall much weaker than in the full signal, and is mostly prevalent in v_{BT}. For u_{BT}, our results show essentially no footprint of the texture, even for the larger k^+ studied. In any event, the decomposition is based on a fundamentally linearised approach, assuming that the roughness length scales are much smaller than those over which the background overlying shear varies (Zhang and Chernyshenko, 2016), and can be expected to fail eventually as k^+ is increase.

The modulation of the roughness-coherent flow by the background turbulence is analogous to the modulation of near-wall turbulence by the outer-layer dynamics (Mathis et al., 2009). The experiments by Mathis et al. (2009), Marusic et al. (2010a), Mathis et al. (2011) and Ganapathisubramani et al. (2012) show that the large scales in the outer regions of a boundary layer modulate the near-wall dynamics. The expression that they propose, and of which Zhang and Chernyshenko (2016) formalise the theoretical analysis, strongly resembles to equations (3.1). In their development, a universal near-wall velocity field is modulated by the large-scale component of the overlying flow. Similarly, in our case, the roughness-coherent component can be seen as playing the role of such universal component that is modulated by large-scale overlying background turbulence. Recently Anderson (2016) corroborated that the modulation of the near-wall is also present in flows over rough surfaces. In our direct numerical simulations, Re_τ is not sufficiently high to reproduce large-scale dynamics, so the background turbulence is essentially that of near-wall, small-scale dynamics. At larger Re_τ, we could expect a cascading modulation, where large scales modulate small scales in the background turbulence, and the full background turbu-

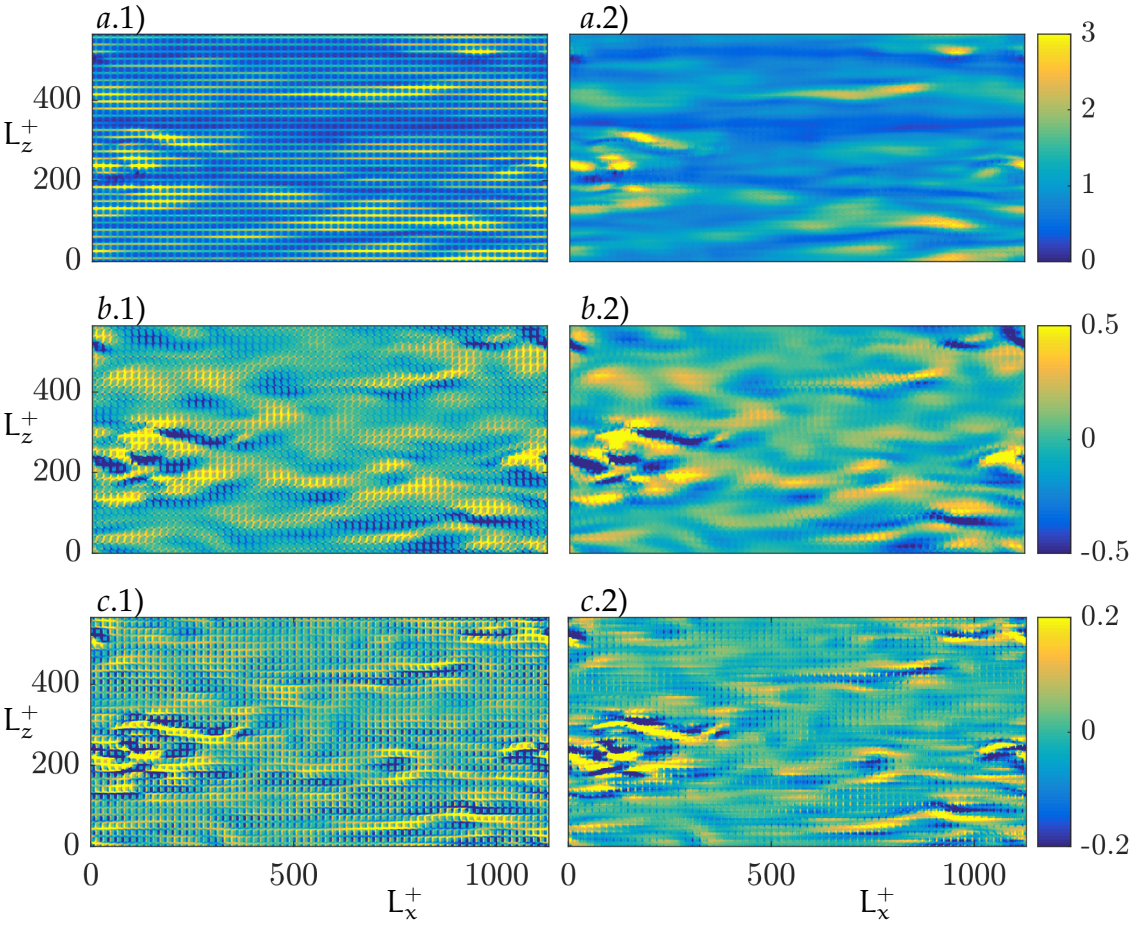

Figure 3.3.: Instantaneous velocity for case C09. (*a*) streamwise velocity; and (*b*) spanwise velocity, at $y^+ \approx 0.3$, (*c*) wall-normal velocity at $y^+ \approx 1$. (*a*.1), (*b*.1) and (*c*.1), full signal; (*a*.2), (*b*.2) and (*c*.2), turbulent contributions obtained using equations (3.2). Mean flow from left to right.

lence modulates the texture-coherent flow.

Beyond instantaneous realisations, the spectral densities of the different flow variables provide quantitative, statistical evidence to evaluate the proposed decomposition. The two-dimensional spectral density of two variables u_1 and u_2 is

$$E_{u_1u_2}(k_x, k_z, y) = \langle \hat{u}_1'(k_x, k_z, y)\hat{u}_2'^{\star}(k_x, k_z, y)\rangle, \tag{3.3}$$

with

$$\langle u'\rangle(y) = \iint_{k_x,k_z} E_{u_1u_2}(k_x, k_z, y)\,d(\log k_x)\,d(\log k_z), \tag{3.4}$$

where $u_2^{\star}$ is the complex conjugate of u_2. Figures 3.4 and 3.5 show premultiplied spectra and cospectra of the full velocity, as well as those of the background turbulence variables, for a roughness of $k^+ \approx 6$ and one of $k^+ \approx 18$. The full flow signals exhibit a large spike at the wavelengths of the texture, s_x and s_z, as well as its corresponding subharmonics. However, the surrounding wavelengths also contain a substantial amount of energy, in a similar fashion to the effect observed in figure 3.1 in one dimension. These regions are the signature of the amplitude modulation of the roughness-coherent flow. Using the classical triple decomposition, without the modulation of the roughness-coherent component, removes the wavelength of the texture only, as shown in figure 3.1(*b*.2). In addition to the wavelengths of the roughness-coherent flow and the background turbulence, we observe very elongated regions with the wavelength of the roughness in z and the range of wavelengths of the background turbulence in x, or vice versa. These are the signature of cross-terms BT–RC in equation (3.2). Let us take for instance the term $u_{BT}u_{RC,u}$, which essentially arises from the interaction of overlying streaks with the texture. In figure 3.2(*a*), it can be observed that the region of high u corresponding to a streak is broken down by the canyons formed by the roughness, so that within the footprint of the streak there are streamwise-aligned, alternating stripes of high and low u. The signature of this phenomenon in spectral space will have the streamwise wavelength of streaks, but the spanwise wavelength of the texture.

For small roughness textures, as in figure 3.4, the scale separation between the turbulent and roughness contributions is large enough that they can essen-

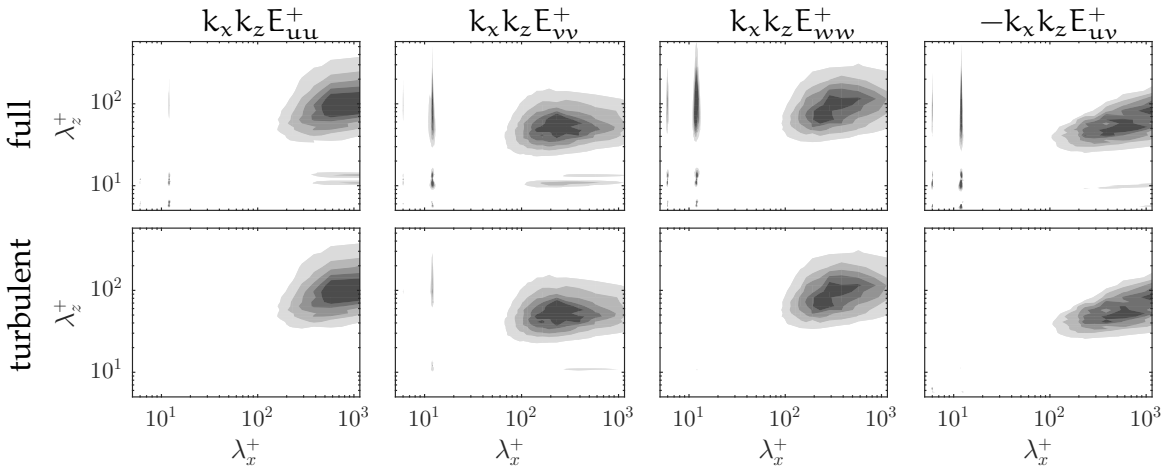

Figure 3.4.: Premultiplied energy spectra of the full velocity signal and its background turbulent component, $k_x k_z E^+_{uu}$, $k_x k_z E^+_{vv}$ and $k_x k_z E^+_{ww}$, and cospectrum of the Reynolds shear stress, $k_x k_z E^+_{uv}$, for case C06, at $y^+ = 2$ for v and $y^+ = 0.5$ for the rest. Maximum values are 0.036, 0.0015, 0.0135 and 0.0013, respectively, with 6 contour levels.

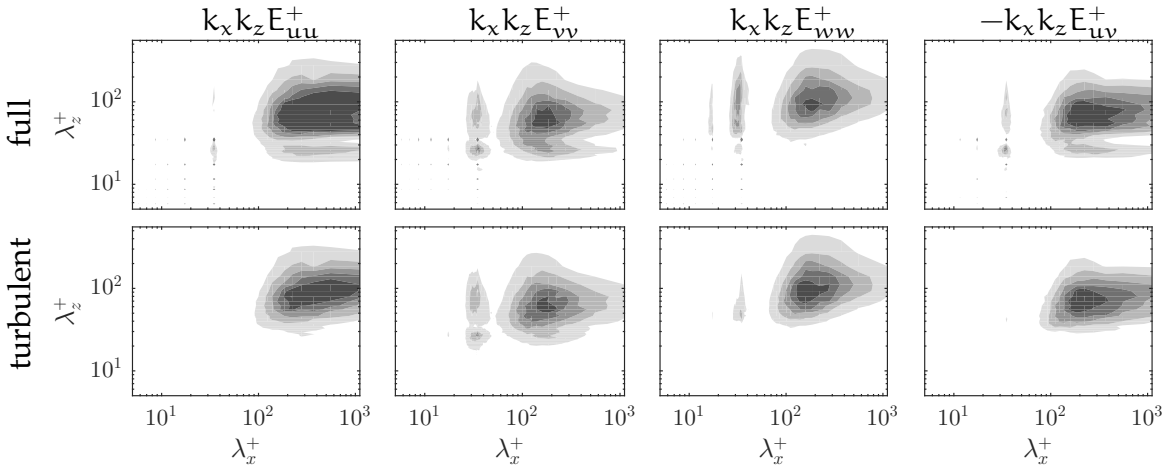

Figure 3.5.: Premultiplied energy spectra of the full velocity signal and its background turbulent component, $k_x k_z E^+_{uu}$, $k_x k_z E^+_{vv}$ and $k_x k_z E^+_{ww}$, and cospectrum of the Reynolds shear stress, $k_x k_z E^+_{uv}$, for case C18, at $y^+ = 2$ for v and $y^+ = 0.5$ for the rest. Maximum values are 0.22, 0.0268, 0.0744 and 0.0421, respectively, with 6 contour levels.

tially be extracted by Fourier filtering. We exploited this in the example shown in figures 3.1(*c*.1) and 3.1(*c*.2). However, for larger k^+, as shown in figure 3.5, the elongated regions mentioned above overlap with the turbulent contribution, which makes a pass-band filter ill-suited. Nevertheless, equations (3.2), interpreted as a filter, provide a tool to extract the turbulent contribution when Fourier filtering is not possible due to an overlap of wavelengths. In section 3.3 this decomposition is used to extract the background turbulence component and analyse the effects of roughness on it. First, in the next section, the roughness-coherent contribution is characterised and a model to predict it is proposed.

3.2. The roughness-coherent component

In smooth walls, the mean velocity is a function of the wall-normal coordinate alone. However, in rough surfaces, we can define a time-averaged mean velocity that not only depends on y, but is also a function of the x and z coordinates. This space-dependent mean flow minus the conventional mean velocity, $U(y)$, is the roughness-coherent contribution introduced in the previous section, which is steady and coherent in space with the roughness texture. If we focus on individual roughness elements, the coherent flow can be thought of as the flow around the obstacles of the roughness geometry driven by the overlying shear. As the flow is deflected from and surrounds the obstacles, it generates a three-dimensional velocity field. The roughness-coherent component can be obtained by averaging the flow in time. Since all geometries in the present work are made up of a periodic pattern, the roughness-coherent contribution will also be periodic, with the same wavelength of the roughness texture. This contribution is therefore obtained by ensemble averaging over time and over the periodic texture units as in Seo et al. (2015).

The coherent flow thus obtained decays above the roughness crests with height. In all our cases, the roughness-coherent components of the velocity have heavily decayed at a distance of $\sim k$, shorter than the commonly accepted height of the roughness-sublayer, $\sim$ 3–5k (Raupach et al., 1991; Flack et al., 2007). The rms of the roughness-coherent components of the velocity, whose squares are commonly referred to as dispersive stresses (Raupach and Shaw, 1982), are de-

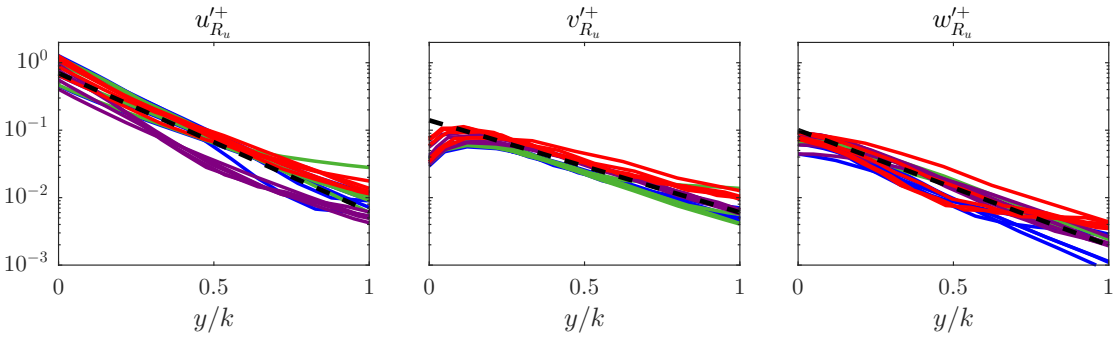

Figure 3.6.: Rms of the roughness-coherent velocity components above the roughness crests. —, collocated posts; —, spanwise-staggered posts; —, streamwise-staggered posts; —, collocated posts of two heights. The reference lines, – –, have slopes of 1.5π, 1π and 1.25π, respectively.

picted in figure 3.6 for several roughness textures and sizes. The decay is of the form $\sim \exp(-y/k)$ and is observed to scale with the roughness height, k, rather than the spacing, s. The rate of decay is observed to be different for the three velocity components, and is fastest for u and slowest for v. For all direct numerical simulations, the magnitude of the fluctuations, and in particular that of the wall-normal component, is below 2 percent of u_τ at one roughness height above the roughness crests. These results are consistent with experiments, where dispersive stresses are found to vanish at $y \approx k$ (Cheng and Castro, 2002; Florens et al., 2013).

For vanishingly small k, the roughness-coherent flow can be thought of as the flow induced around the roughness elements driven by a steady, homogeneous overlying shear. This concept was already used by Luchini et al. (1991), where they considered riblets of a vanishingly small size, so that the surface perceives the overlying turbulence as steady and homogeneous. Notice that, for small roughness, in the transitionally rough regime, the time-scales and length-scales of the overlying background-turbulent fluctuations are much larger than those of the roughness. These latter fluctuations are quasi-steady and quasi-homogeneous with respect to the characteristic scales of the surface, i.e. they vary slowly and over long distances. The concept of a quasi-steady, quasi-homogeneous limit was formalised by Zhang and Chernyshenko (2016) regarding the interaction between the overlying large-scales of the outer region and the smaller and

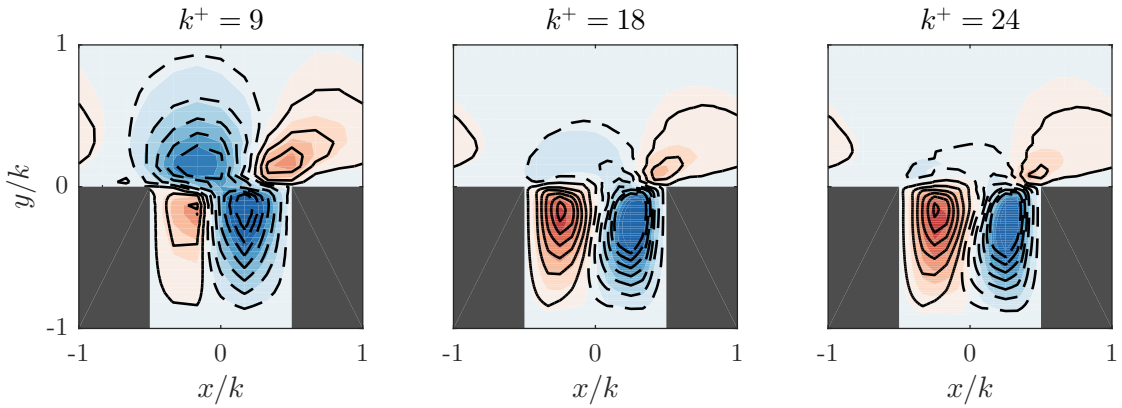

Figure 3.7.: Wall-normal velocity for cases (left) C09, (centre) C18 and (right) C24. Shaded, roughness-coherent contribution from direct numerical simulations; contours, steady laminar model. Red and solid indicate positive values, blue and dashed indicate negative values, with a maximum of 3.5 and a minimum of −3.5.

faster near-wall fluctuations, and a similar framework would apply here.

The roughness-coherent flow for small k^+, as suggested above, can be modelled as the flow induced by a steady and homogeneous overlying background flow. Therefore, to approximate the roughness-coherent contribution, we conduct steady, laminar simulations using the numerical methodology described in chapter 2, but where the periodic domain only contains one texture element. The mean shear and viscosity are adjusted to match the same k^+ of the corresponding direct numerical simulations. For small but finite values of k^+, these numerical domains are too small to sustain turbulence (Jiménez and Moin, 1991), and result in laminar, steady flows, which provide estimates of the roughness-coherent contribution. For instance, figure 3.7 compares the wall-normal roughness-coherent velocity obtained from the direct numerical simulations by ensemble averaging to the laminar model. Laminar simulations begin to deviate for the intermediate case, C18, but they still exhibit good qualitative agreement for the larger case, C24. Notice that, even for the smallest k^+, the flow is not symmetric and does not behave as purely viscous. It is therefore necessary to consider the advective terms, in contrast with the Stokes-flow analysis of Luchini et al. (1991). This model also allows us to predict the rms fluctuations of the roughness-coherent flow. Figure 3.8 depicts data from our direct numerical

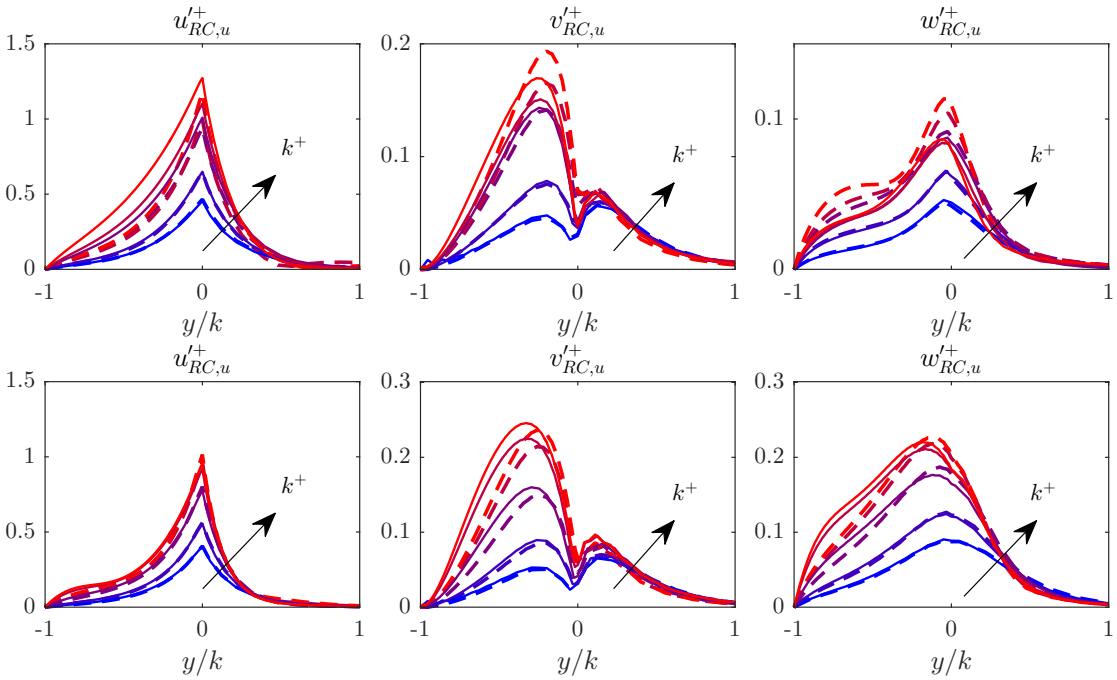

Figure 3.8.: Rms of the roughness-coherent contribution for the collocated and streamwise-staggered roughness. Solid, results from direct numerical simulations; dashed, results from the laminar model simulations. Blue to red, cases C06 to C18 (top) and SX06 to SX18 (bottom).

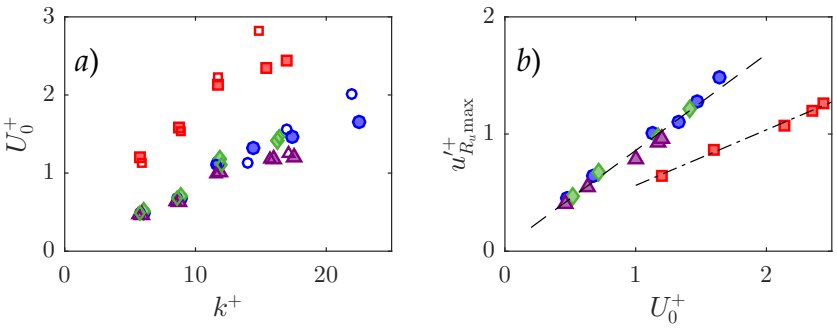

Figure 3.9.: (*a*) Mean streamwise velocity at the roughness crests. (*b*) Maximum streamwise roughness-coherent velocity as a function of the mean streamwise velocity at the roughness tips. ●, collocated posts; ◆, spanwise-staggered posts; ▲, streamwise-staggered posts; ■, collocated posts of two heights. Empty symbols correspond to estimations from the laminar model. Linear regression with slopes: – –, 0.82; and –·–, 0.47.

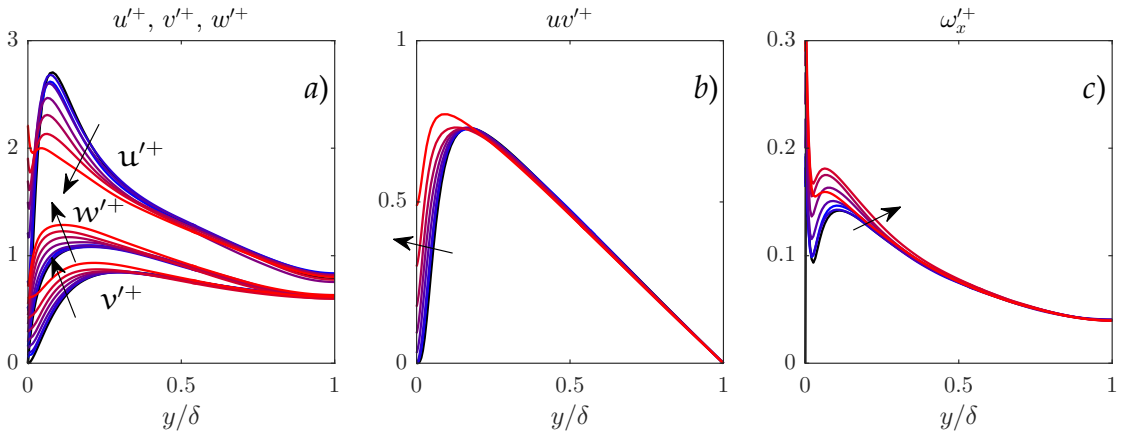

Figure 3.10.: Full rms fluctuations. Blue to red, cases C06 to C36; black, smooth channel. The arrows indicate increasing roughness size. (*a*), streamwise, wall-normal and spanwise velocity fluctuations; (*b*), Reynolds shear stress; (*c*) streamwise vorticity fluctuations.

simulations compared against those from the laminar model, and shows good agreement for $k^+ \lesssim 15$ for all our roughness surfaces. Notice that this method can also be used to estimate properties of the mean velocity profile close to the rough surface, such as the mean streamwise velocity at the roughness crests, by averaging along the x and z directions, as shown in figure 3.9.

3.3. The background turbulence component

Roughness does not only excite the wavelengths of the surface texture, but also modifies the background turbulence. This can be observed in the rms fluctuations that incorporate effects from both the roughness contribution, studied in the previous section, and the background turbulence. The streamwise rms fluctuations, shown in figure 3.10, decrease near the wall, and in particular the peak of intensity lowers as the roughness size increases, while a significant growth occurs at the roughness crests in a similar fashion to that in figure 3.8. This decrease in the peak of intensity can only be caused by a decrease, and therefore modification, of the rms fluctuations of the background-turbulent component. The wall-normal and spanwise rms fluctuations present an increase of intensity across the entire roughness sublayer, from the roughness crests to their near-

wall intensity peak. The near-wall intensity peak of the streamwise vorticity fluctuation also increases, save for the largest case, which flattens in magnitude and almost disappears, this being a symptom of roughness altering the near-wall cycle. Notice that these modifications of the rms fluctuations extend to a distance of $\sim 2k$, larger than the decay distance of the roughness-coherent signal observed in the previous section. However, beyond that distance, the rms fluctuations resemble those in smooth-wall turbulence, in agreement with the outer-layer similarity hypothesis (Townsend, 1976).

In this section, we analyse the effect of roughness on the background turbulence and, in particular, on the rms fluctuations. The rms fluctuations of the full signal, as shown in figure 3.10, contain contributions from both the turbulent-background and roughness-coherent components. However, the decomposition of equations (3.2) can be used to derive approximate expressions for the rms velocities from which the rms fluctuations of the background turbulence can be extracted. For the geometries studied in this work, the leading terms are

$$\begin{aligned}
\langle u'^2\rangle &= \langle u_{BT}^2\rangle + \langle u_{RC,u}^2\rangle \\
&\quad + \langle u_{RC,u}^2\rangle \left\langle \frac{u_{BT}^2}{U^2}\right\rangle + \langle u_{RC,v}^2\rangle \left\langle \frac{v_{BT}^2}{\widetilde{v}^2}\right\rangle + \langle u_{RC,w}^2\rangle \left\langle \frac{w_{BT}^2}{\widetilde{w}^2}\right\rangle, \qquad (3.5a)\\
\langle v'^2\rangle &= \langle v_{BT}^2\rangle + \langle v_{RC,u}^2\rangle \\
&\quad + \langle v_{RC,u}^2\rangle \left\langle \frac{u_{BT}^2}{U^2}\right\rangle + \langle v_{RC,v}^2\rangle \left\langle \frac{v_{BT}^2}{\widetilde{v}^2}\right\rangle + \langle v_{RC,w}^2\rangle \left\langle \frac{w_{BT}^2}{\widetilde{w}^2}\right\rangle, \qquad (3.5b)\\
\langle w'^2\rangle &= \langle w_{BT}^2\rangle + \langle w_{RC,u}^2\rangle \\
&\quad + \langle w_{RC,u}^2\rangle \left\langle \frac{u_{BT}^2}{U^2}\right\rangle + \langle w_{RC,v}^2\rangle \left\langle \frac{v_{BT}^2}{\widetilde{v}^2}\right\rangle + \langle w_{RC,w}^2\rangle \left\langle \frac{w_{BT}^2}{\widetilde{w}^2}\right\rangle, \qquad (3.5c)\\
\langle u'v'\rangle &= \langle u_{BT}v_{BT}\rangle + \langle u_{RC,u}v_{RC,u}\rangle \\
&\quad + \langle u_{RC,u}v_{RC,u}\rangle \left\langle \frac{u_{BT}^2}{U^2}\right\rangle + \langle u_{RC,v}v_{RC,v}\rangle \left\langle \frac{v_{BT}^2}{\widetilde{v}^2}\right\rangle + \langle u_{RC,w}v_{RC,w}\rangle \left\langle \frac{w_{BT}^2}{\widetilde{w}^2}\right\rangle \\
&\quad + \langle u_{RC,u}v_{RC,v}\rangle \left\langle \frac{u_{BT}v_{BT}}{U\widetilde{v}}\right\rangle, \qquad (3.5d)
\end{aligned}$$

where the angled brackets indicate temporal and x-z-spatial averaging, and the prime refers to fluctuations with respect to the mean. The full expressions including the terms that are negligible for our geometries can be found in ap-

pendix A. Equations 3.5 are adequate approximations only for small roughness, as long as equations (3.2) hold. The coherent–background cross terms, which are zero in the conventional triple decomposition, can be of the same order of magnitude as the coherent–coherent terms. Equations (3.5) can be used to extract the rms fluctuations of the background-turbulent contribution from the full and the roughness-coherent signals.

The rms fluctuations of the background turbulence are shifted towards the wall, as if they perceived a smooth wall, or a virtual origin, below the roughness crests. In the first column of panels in figure 3.11, the rms fluctuations of the background turbulence are compared with those in smooth-wall turbulence. The decomposition presented in equations (3.5) removes the near-wall peaks, which are observed for the full rms in figure 3.10, from the background turbulence rms. The fluctuations are shifted towards the wall, but otherwise display a similar shape to those of smooth-wall turbulence close to the wall. We refer to this displacements as virtual origins, since the rms fluctuations behave as if they had an origin below the roughness crests. This can be interpreted as the height below the roughness crests at which they would to go to zero if extended as smooth-wall rms fluctuations. Numerical results by MacDonald et al. (2016) also present a similar displacement.

The virtual origin of the streamwise rms fluctuations, ℓ_u^+, is obtained as the depth below the roughness crests at which u'^+_{BT} would zero out, when extrapolated from its profile above the roughness crests. When u'^+_{BT} is portrayed versus the height measured from that origin, as in figure 3.11(*b*.2), a good collapse with smooth wall data is observed in the first few wall units of height. However, this collapse does not extend outside the roughness sublayer, where all curves should converge to the smooth-wall case. According to Townsend's outer-layer similarity hypothesis (Townsend, 1976), sufficiently far from the wall, effectively outside the roughness sublayer, all turbulent fluctuations are independent of the surface condition when normalised in wall units. In the second column of panels in figures 3.11, the origin of the rms fluctuations is set at ℓ_u^+ for all variables. We observe that this virtual origin does not adequately collapse any rms fluctuations other than those of the streamwise velocity very near the wall.

We observe that the streamwise virtual origin, ℓ_u^+, is related to the apparent

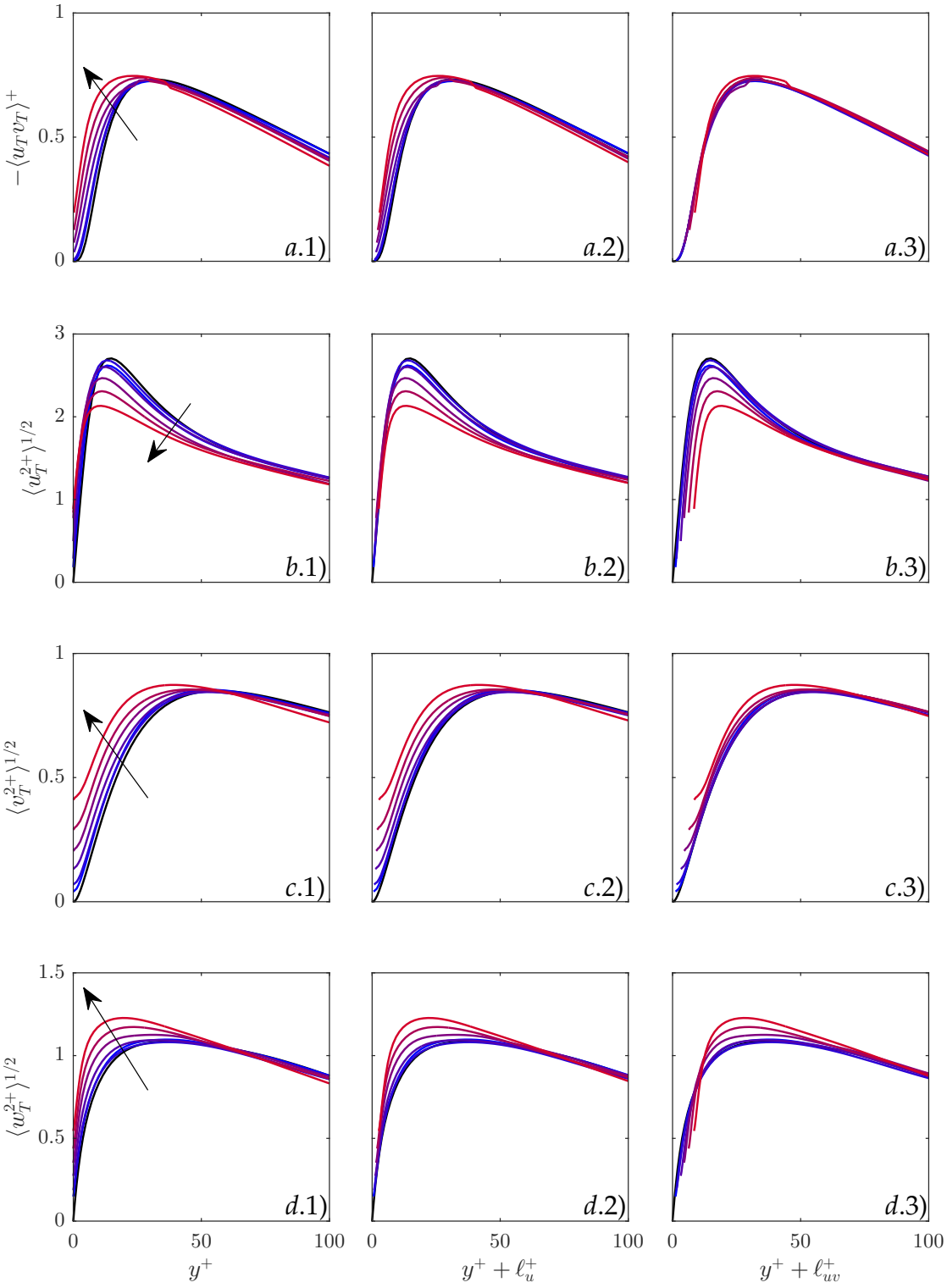

Figure 3.11.: Rms fluctuations of the background turbulent flow. (*a*) Reynolds shear stress, $u_{BT}v_{BT}$; (*b*) streamwise velocity, u_{BT}; (*c*) wall-normal velocity, v_{BT}; (*d*) spanwise velocity, w_{BT}. Blue to red, cases C06 to C24; black, smooth channel; the arrow indicates increasing k^+.

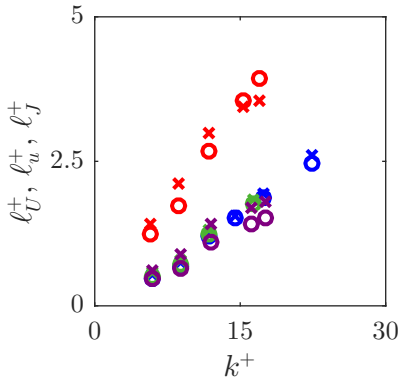

Figure 3.12.: Virtual origins for different geometries and k^+. ×, ℓ_U^+; ○, ℓ_u^+; and +, ℓ_J^+. Blue collocated posts; green, spanwise-staggered posts; purple, streamwise-staggered posts; red, collocated posts of two heights.

origin of the mean velocity profile. Determining the correct zero-plane displacement for the law of the wall is a question that has always been present in roughness studies. This reference level for the mean velocity profile is usually referred to as displacement height, and it is in essence equivalent to what we have defined as virtual origins, as it is a shift in the y-coordinate. Jackson (1981) proposes a displacement height, ℓ_J^+, based on the centroid of the total stress below the roughness crests, i.e. the height at which the mean surface drag appears to act,

$$\ell_J^+ = \int_{k^+} \left(\frac{dU^+}{dy^+} - \langle uv \rangle^+ \right) dy^+. \tag{3.6}$$

Similarly, since this displacement is essentially a virtual origin, we can also define another virtual origin for the mean velocity profile, ℓ_U^+, as the distance from the roughness crests at which the velocity would go to zero. This definition is equivalent to that used above for ℓ_u^+, where ℓ_U^+ can be obtained by linearly extrapolating the mean velocity profile at the wall. In figure 3.12, we observe that ℓ_U^+, ℓ_u^+ and ℓ_J^+ are generally similar for different roughness configurations and sizes.

The virtual origins of all cases are reported in table 3.1.

Further away from the wall, where the influence of the roughness-coherent flow is negligible, the rms fluctuations suggest that turbulence behaves as smooth-wall, canonical turbulence with a virtual origin ℓ_{uv}^+. The virtual origin of the Reynolds shear stress, ℓ_{uv}^+ appears to be the virtual origin of turbulence outside

	Case	δ/k	k^+	ΔU^+	Re_τ	U_0^+	ℓ_U^+	ℓ_u^+	ℓ_J^+	ℓ_{uv}^+
Smooth Channel	SC	—	0.0	0.0	183.9	0.0	0.0	0.0	0.0	0.0
Collocated	C06	30.6	6.0	0.5	183.9	0.5	0.5	0.5	0.6	1.2
	C09	20.4	8.8	0.7	180.8	0.7	0.7	0.7	0.7	1.5
	C12	15.4	11.7	1.5	180.0	1.1	1.2	1.2	1.2	3.2
	C15	12.3	14.4	2.4	178.7	1.3	1.5	1.6	1.6	4.5
	C18	10.3	17.4	3.5	179.0	1.5	1.9	1.9	2.3	6.3
	C24	7.7	22.5	4.7	174.5	1.6	2.5	2.6	3.8	8.4
	C36	5.2	35.7	6.7	186.7	2.1	4.4	4.8	8.8	—
Collocated two heights	CC06	30.7	5.8	0.8	178.7	1.2	1.2	1.4	1.3	2.1
	CC09	20.6	8.7	1.8	179.8	1.6	1.7	2.1	1.7	3.7
	CC12	15.5	11.7	3.3	182.6	2.1	2.7	3.0	2.6	6.2
	CC15	11.7	15.4	4.5	180.1	2.4	3.6	3.4	3.5	8.3
	CC18	10.4	17.0	4.9	176.7	2.4	3.9	3.5	4.0	9.1
Spanwise staggered	SZ06	30.6	5.9	0.4	183.0	0.5	0.5	0.6	0.6	1.0
	SZ09	20.4	8.9	0.9	182.7	0.7	0.7	0.8	0.8	1.7
	SZ12	15.4	11.8	1.6	181.8	1.2	1.3	1.3	1.3	3.4
	SZ15	11.6	16.2	3.2	188.3	1.4	1.8	1.8	2.1	6.0
Streamwise staggered	SX06	30.6	5.9	0.6	181.6	0.5	0.5	0.6	0.5	1.1
	SX09	20.4	8.8	1.2	179.5	0.6	0.6	0.9	0.7	2.0
	SX12	15.4	11.9	2.6	183.1	1.0	1.1	1.4	1.2	4.2
	SX15	11.5	16.0	4.1	185.3	1.2	1.4	1.7	1.6	6.0
	SX18	10.3	17.6	4.3	180.6	1.2	1.5	1.8	1.8	6.2

Table 3.1.: Main characteristics of the simulations. The characteristic size of the roughness elements is k. The half-height of the channel, measured from the roughness crests, is denoted by δ. The mean velocity at the roughness crests is U_0. ℓ^+ denotes the depth of virtual origins, measured from the tips, as introduced in section 3.3. The subscript $_U$ refers to the virtual origin of the mean velocity profile; $_u$, virtual origin of the streamwise rms fluctuations; $_J$, Jackson's displacement height (Jackson, 1981); and $_{uv}$ refers to the virtual origin of the Reynolds shear stress.

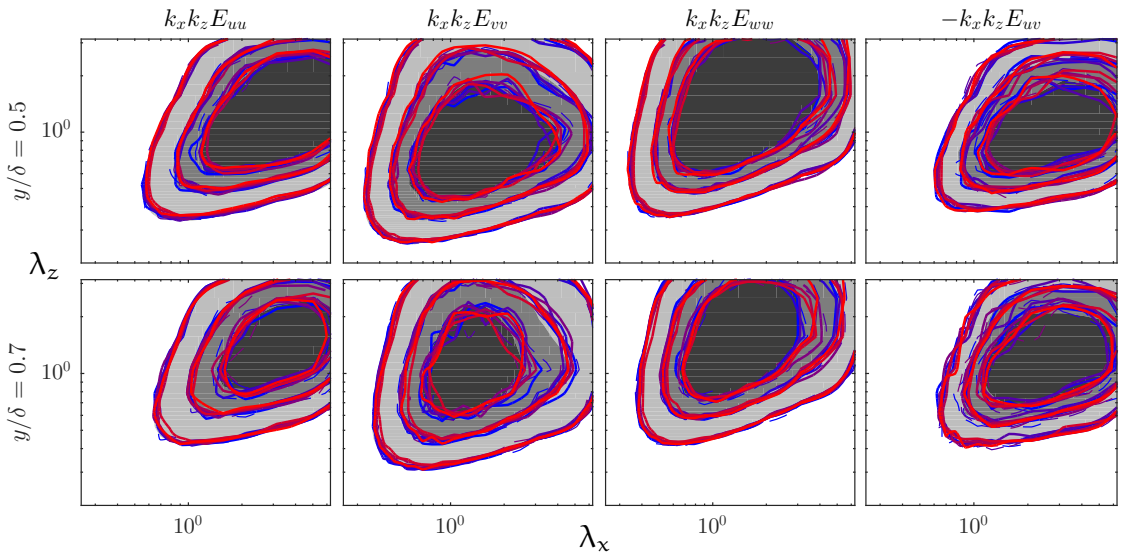

Figure 3.13.: Energy spectra and cospectrum of the velocity outside the roughness sublayer. The corresponding virtual origin is accounted for. Shaded, smooth-wall turbulence; solid blue to red, cases C06 to C36; and dashed blue to red, cases SZ06 to SZ15.

the roughness sublayer (Gómez-de-Segura et al., 2018a; Fairhall et al., 2018). Unlike for the rms fluctuations of the three velocity components, the shape of the Reynolds shear stress near the wall does not drastically change with roughness. In figure 3.11(*a*.3), we observe that using the virtual origin of its rms fluctuations, ℓ^+_{uv}, not only collapses the profiles in the region near the wall, but the entire curve. In the third column of panels in figure 3.11, the origin of the rms fluctuations is set at ℓ^+_{uv} for all variables. The rms fluctuations, including the streamwise ones, converge to smooth-wall turbulence rms fluctuations outside the roughness sublayer. Very near the wall, different variables would extrapolate to zero at different heights, as is particularly evident for u'^+_{BT} and w'^+_{BT}, which experience virtual origins shallower than ℓ^+_{uv}. Beyond this, up to at least $k^+ \approx 15$, the curves show an excellent collapse with smooth wall data. This suggests that, up to that k^+, turbulence remains essentially canonical, i.e. smooth-wall-like.

Figure 3.13 presents the energy spectra above the roughness sublayer, which display no significant discrepancy respect to the smooth-wall solution, even for $\delta/k \approx 5$, supporting that the flow over transitional roughness is statistically equivalent to that over a smooth-wall far away from the wall (Townsend, 1976).

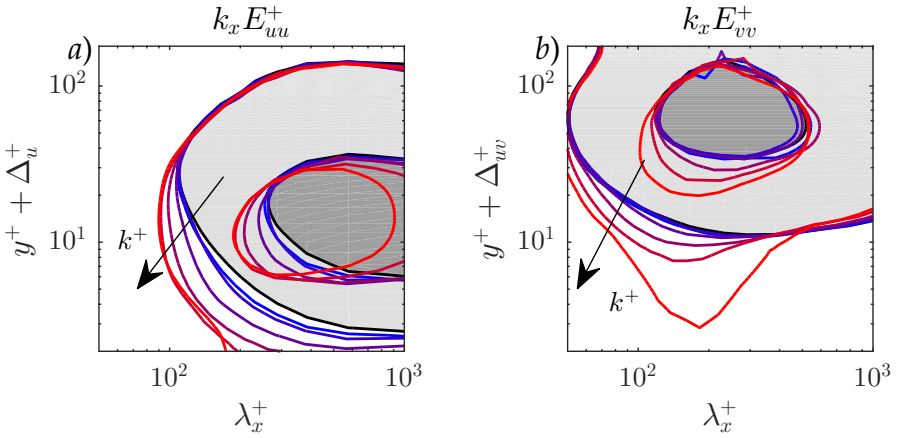

Figure 3.14.: (*a*) Streamwise and (*b*) spanwise one-dimensional pre-multiplied spectra for, blue to red, cases C06 to C36; and, shaded, smooth-channel. The contours are (*a*) $0.3u_\tau$ and $1.2u_\tau$, and (*b*) $0.04u_\tau$ and $0.2u_\tau$.

The evolution with y of one-dimensional spectral density of the streamwise and wall-normal velocity components are presented in figure 3.14. Differences are only observed near the wall. Notice, however, that the wall-normal spectrum converges to smooth-wall at a larger distance than the streamwise one.

To further explore the modifications of the background turbulence by roughness within the roughness sublayer, we analyse its two-dimensional energy density spectra and cospectra, E. As introduced in section 3.1, the decomposition can be used to obtain the two-dimensional energy spectra of the background turbulence, without the footprint of roughness. Figure 3.15 shows the turbulent premultiplied spectra of u_{BT}, v_{BT} and premultiplied cospectra of $u_{BT}v_{BT}$, together with smooth-wall results at the equivalent height accounting for the corresponding virtual origin. For this roughness, the spectra present little changes for $k^+ \lesssim 12$. As size increases, the spectra and cospectra start to be modified: the energy at large λ_x^+ decreases, while at smaller λ_x^+ there is an increase of energy. The decrease of energy at large wavelengths is particularly clear for the streamwise velocity component. There is also a noticeable change in the spanwise direction. The spectra and cospectra, especially that of v, display an increase of energy at small λ_x^+ and a wider range of λ_z^+. This increase of energy is centred approximately at $\lambda_x^+ \sim 150$, being particularly clear for the spectral density of the wall-normal velocity, E_{vv}. These changes are further explored in chapter 5.

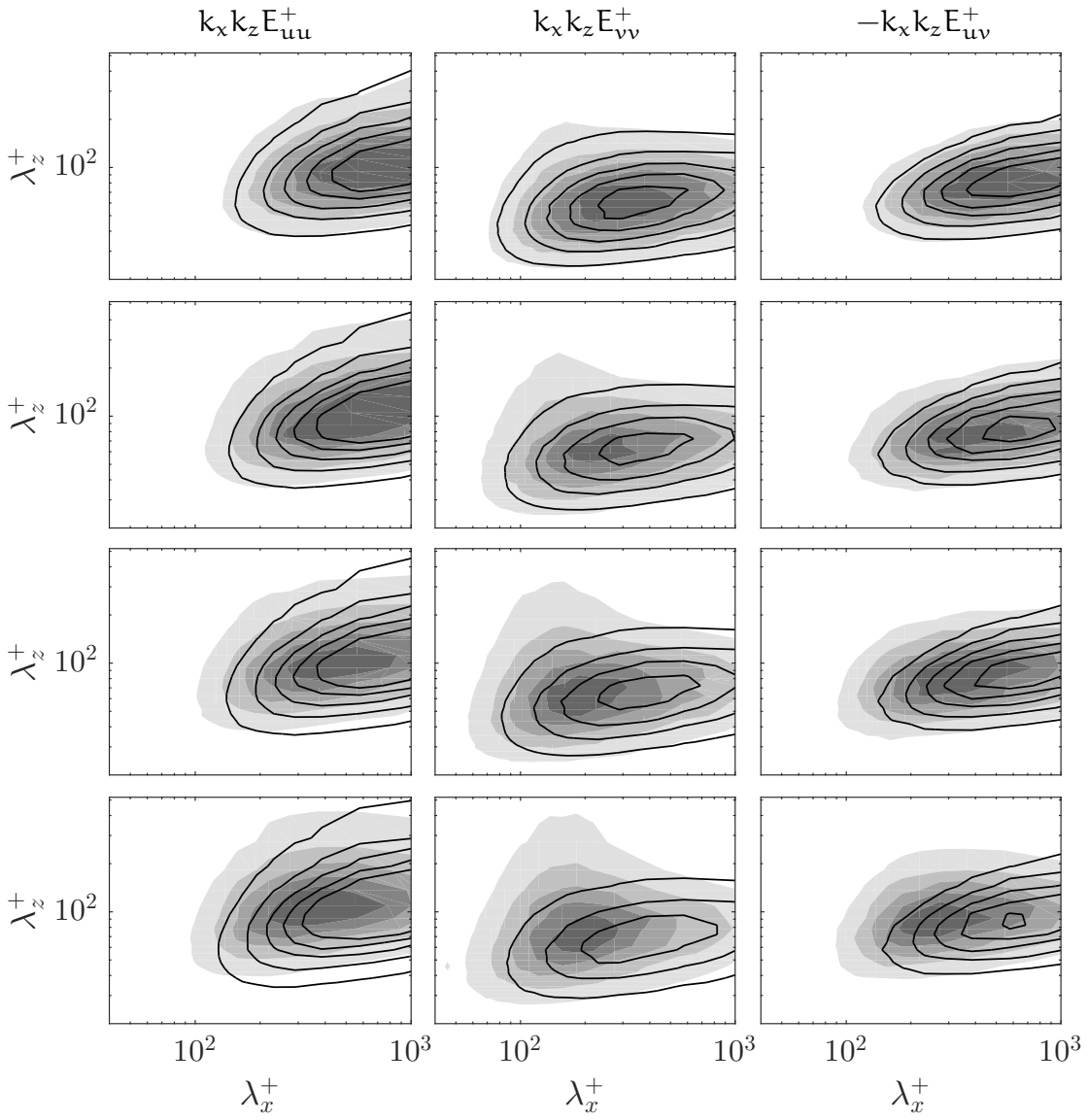

Figure 3.15.: Two-dimensional premultiplied spectra of the streamwise and wall-normal velocity components, and cospectrum of the Reynolds shear stress at $y^+ = 8$, from top to bottom cases C12, C15, C18 and C24. Shaded, background-turbulent component; —, smooth-wall data at the equivalent height above the corresponding virtual origin. Contours indicate the same value in wall units. The minimum value, in white, is zero for all subfigures, the maximum values, from left to right and top to bottom, are 1.397, 0.0338, 0.1376, 1.2883, 0.0524, 0.1675, 1.3329, 0.0662, 0.1847, 1.1633, 0.1011, 0.231.

3.4. Conclusions and discussion

We observe that, for small roughness in the transitionally rough regime, the flow can be thought of as composed of two contributions: a background-turbulent component, somewhat similar to that over smooth walls; and a roughness-coherent one, induced by roughness and modulated by the overlying background turbulence. Using this amplitude modulated decomposition, the background turbulence can be extracted from the full signal and analysed to investigate the effect of roughness on the flow.

The roughness-coherent component vanishes at heights lower than the roughness sublayer, suggesting that the modifications of the flow are present in the background turbulence at a larger distance than the contribution from the roughness-coherent component. It is also observed that the decay of the wall-normal roughness-coherent component is slower than that of the other velocity components. In addition, we present results where, for small roughness size k^+, this roughness-coherent contribution is approximated using a laminar simulation.

For a large extent of the transitionally rough regime, the most relevant effect of roughness on the background turbulence is the displacement towards the wall of the rms fluctuations of the velocity. This is interpreted in this work as turbulence perceiving an effective smooth-wall at a certain virtual origin below the roughness crests. The virtual origin of the Reynolds stress, ℓ^+_{uv}, seems to be the one perceived by turbulence, and therefore affecting the roughness function and skin friction.

4. Towards a predictive model for the roughness function

Part of the content of this chapter has been published in N. Abderrahaman-Elena et al. (2019). 'Modulation of near-wall turbulence in the transitionally rough regime'. J. of Fluid Mech. *865, pp. 1042–1071.*

In chapter 1, we have discussed the main drawbacks of the equivalent sand roughness, k_s^+, which, for historical reasons, has been widely used to characterise rough surfaces. However, k_s^+ can neither be predicted a priori, nor describes appropriately the transitionally rough regime. The latter is explicitly highlighted by Jiménez (2004), who shows that a collapse of the fully rough regime does not guarantee such a collapse in the transitionally rough regime, as shown in figure 1.1. Therefore, k_s^+ is not a universal parameter to predict a priori ΔU^+in the transitionally rough regime. Likewise, k^+ presents similar problems, as it is roughly proportional to k_s^+ (Schlichting, 1936). Figure 4.1 shows ΔU^+ as a function of the roughness element height in wall units, k^+, and of Jackson's displacement height, ℓ_J^+. Both capture the trend of increasing ΔU^+ for increasing roughness size, but display a strong dependence with the type of roughness surface. Orlandi and Leonardi (2006) find a strong linear correlation between $\Delta U^+ - U_0^+$ and the rms fluctuations of the wall-normal velocity at the roughness crests, $\overline{v}_t'^+$, as shown in figure 4.1(*c*) for our simulations. Similarly, a linear relationship between $\Delta U^+ - U_0^+$ and ℓ_{uv}^+ is also observed in figure 4.1(*d*). As introduced earlier, ℓ_{uv}^+ is the shift of the Reynolds stress below the roughness crests, and can be interpreted as the apparent position of the origin for turbulence. Both $\overline{v}_t'^+$ and ℓ_{uv}^+ establish a connection between the roughness function

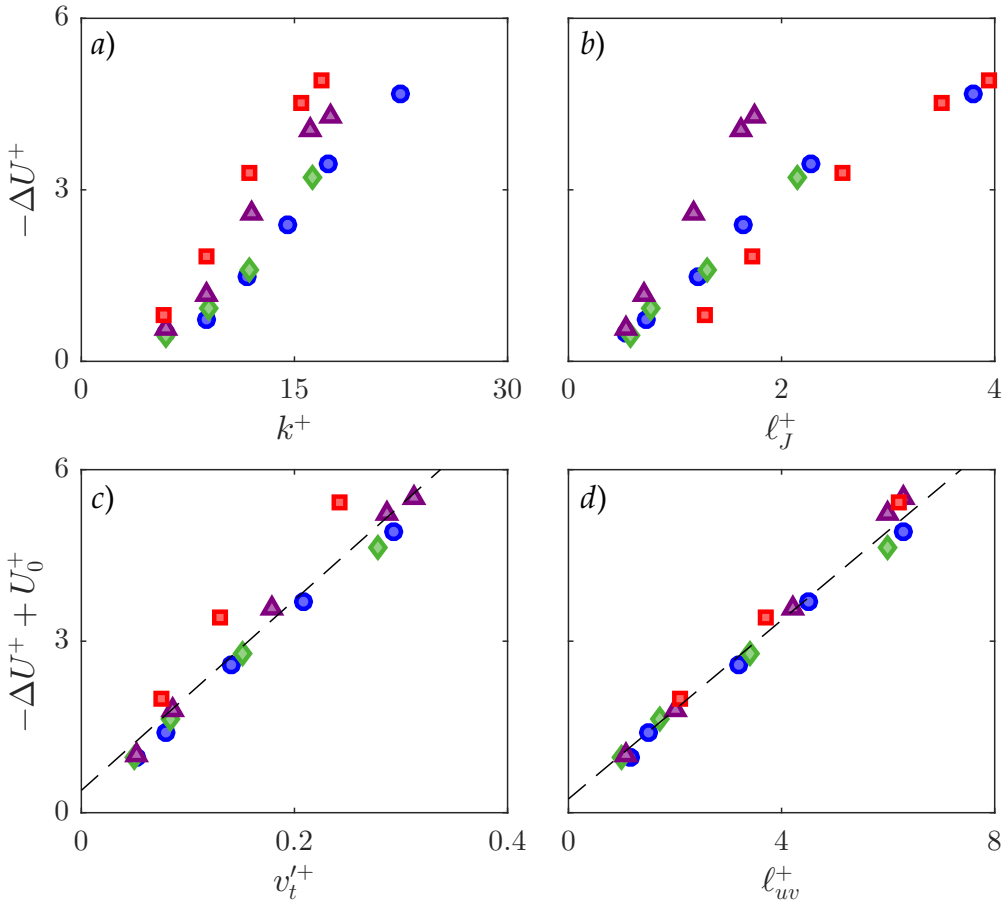

Figure 4.1.: Roughness function represented versus (*a*) roughness height in wall units, (*b*) Jackson's displacement height in wall units, (*c*) wall-normal velocity fluctuations at the roughness crests, and (*d*) virtual origin of turbulence. ●, collocated posts; ◆, spanwise-staggered posts; ▲, streamwise staggered posts; ■, collocated posts of two heights; – –, linear regressions $16.6\, v_t'^+$ and $0.78\, \ell_{uv}^+$.

and the effect of the roughness surface on the flow.

4.1. Breakdown of the contributions to the roughness function

The mean momentum equation is used below to explore this relationship between the roughness function, ΔU^+, and the virtual origin of the Reynolds shear stress, ℓ^+_{uv}. The goal is to obtain an expression for the roughness function. The procedure followed here is similar to that in García-Mayoral and Jiménez (2011) to study the contributions to ΔU^+. In a turbulent channel, the mean momentum equation along the streamwise direction is

$$-\langle uv\rangle + \nu\frac{dU}{dy_r} = u_\tau^2\frac{\delta' - y_r}{\delta'}, \tag{4.1}$$

where y_r is the wall-normal coordinate measured from the virtual origin of the mean velocity profile, $y_r = y - \ell_U$, and the apparent half-height of the channel has previously been defined as $\delta' = \delta + \ell_U$. This allows us to define a common origin $y_r = 0$ for the mean velocity profiles under different setup configurations. Note that ℓ_U is positive and $\delta' > \delta$. Scaling equation (4.1) in viscous units gives

$$-\langle uv\rangle^+ + \frac{dU^+}{dy^+} = \frac{\delta'^+ - y_r^+}{\delta'^+}. \tag{4.2}$$

This expression is valid above the roughness crests, $y^+ > 0$ or $y_r^+ > \ell_U^+$. Integrating equation (4.2) allows us to obtain U^+, and thus an expression for the roughness function, ΔU^+, as the difference in U^+ between rough and smooth-wall cases. At a distance H^+ sufficiently far from the wall, where outer-layer similarity holds and the mean velocity profile is logarithmic, the roughness function is $\Delta U^+ = U_r^+(H^+) + U_s^+(H^+)$. Let us denote by the subscripts 'r' and 's' the variables in a rough and smooth-wall channel, respectively. Equation (4.2) can then

be integrated between two heights

$$\int_{h_s^+}^{H^+} -\langle uv\rangle_s^+ \, dy^+ + U_s^+(H^+) - U_s^+(h_s^+) = (H^+ - h_s^+) - \frac{1}{2}\frac{H^{+2} - h_s^{+2}}{\delta_s'^+}, \tag{4.3a}$$

$$\int_{h_r^+}^{H^+} -\langle uv\rangle_r^+ \, dy^+ + U_r^+(H^+) - U_r^+(h_r^+) = (H^+ - h_r^+) - \frac{1}{2}\frac{H^{+2} - h_r^{+2}}{\delta_r'^+}, \tag{4.3b}$$

where the lower bounds of integration, h_r^+ and h_s^+, can in principle be different for the rough and the reference smooth case, but for equation (4.1) to hold, $h_r^+ \geqslant \ell_U^+$ is required. An expression for the roughness function, ΔU^+, can be obtained by subtracting equation (4.3a) from (4.3b). Taking $h^+ = h_s^+ = h_r^+ = \ell_U^+$, we then have

$$\Delta U^+ = U_r^+(H^+) - U_s^+(H^+) = \mathcal{T}_1 + \mathcal{T}_2 + \mathcal{T}_3, \tag{4.4}$$

where

$$\mathcal{T}_1 = -\left(\int_{h^+}^{H^+} -\langle uv\rangle_r^+ \, dy^+ - \int_{h^+}^{H^+} -\langle uv\rangle_s^+ \, dy^+\right), \tag{4.5a}$$

$$\mathcal{T}_2 = U_r^+(h^+) - U_s^+(h^+), \tag{4.5b}$$

$$\mathcal{T}_3 = -\frac{1}{2}\left(\frac{H^{+2} - h^{+2}}{\delta_r'^+} - \frac{H^{+2} - h^{+2}}{\delta_s'^+}\right). \tag{4.5c}$$

The first term, $\mathcal{T}_1$, encapsulates the increase in Reynolds stress that roughness produces compared to that over a smooth wall. Over conventional roughness, the Reynolds stress increases near the wall and hence the negative contribution of this term towards ΔU^+. Drag reducing surfaces produce large slip velocities that overcome the effect of $\mathcal{T}_1$, resulting in a net reduction of drag. Similarly, roughness also displays a mean velocity at the roughness crests, which is captured by the first term in $\mathcal{T}_2$. However, when the change in the virtual origin of the mean velocity profile is accounted for, by the second term in $\mathcal{T}_2$, the net result is generally negative. The first contribution to $\mathcal{T}2$ is simply the mean velocity at the roughness crests, U_0. The other contribution to $\mathcal{T}_2$ is the mean velocity of the smooth-wall channel at the roughness crests equivalent height, that is what the mean velocity would be at the roughness tips if the rough wall had no ef-

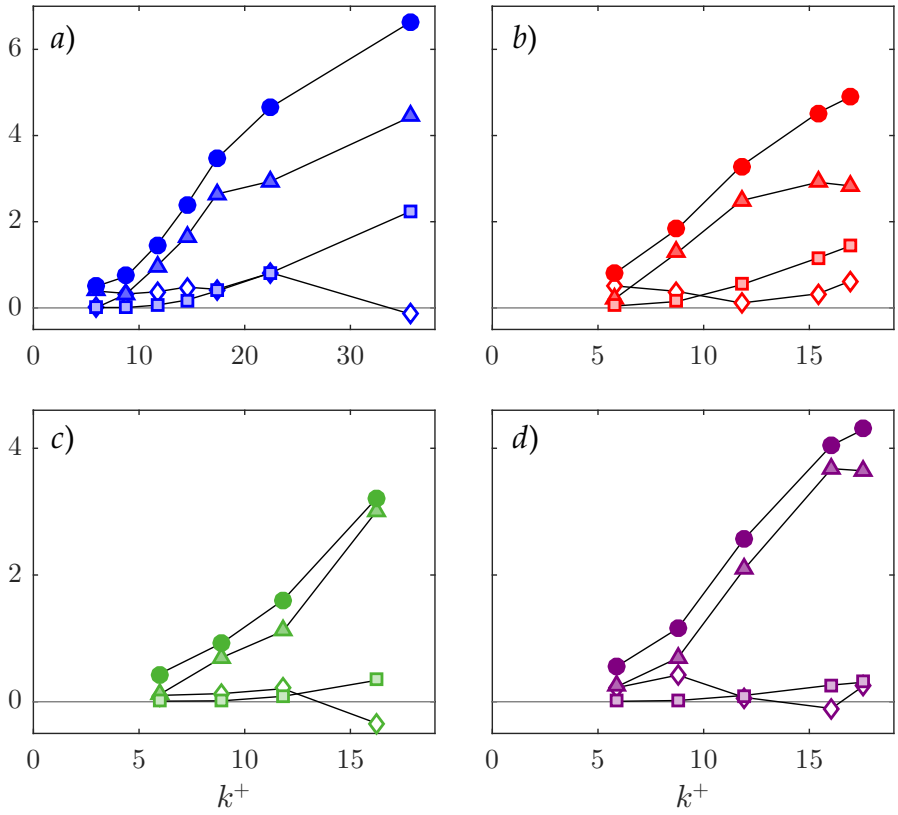

Figure 4.2.: Contributions to ΔU^+ for (*a*) collocated posts, (*b*) collocated posts of two heights, (*c*) spanwise-staggered posts, and (*d*) streamwise-staggered posts. ▲, T1; ■, T2; and ◆, T3; ●, $\Delta U^+ = T1 + T2 + T3$.

fect on the mean velocity profile. The term $\mathcal{T}_2$ then represents the difference between the actual mean velocity at the roughness crests and the ideal velocity that would have been achieved at such height without roughness. Notice that for small roughness, $\mathcal{T}_2 \approx 0$. As size increases, the advective terms gain relevance at the roughness crests and the magnitude of $\mathcal{T}_2$ increases. Finally, $\mathcal{T}_3$ accounts for Reynolds-number discrepancies between the different simulations, being zero if $\delta_r'^+ = \delta_s'^+$. In essence, the term $\mathcal{T}_3$ is obtained by integrating the total stress, i.e. the linear, right-hand-side of equation (4.2). The intersect of the linear total stress at different δ^+ causes relative variations in $\mathcal{T}_3$ of order $\delta_r'^+/\delta_s'^+$.

In our simulations, $\mathcal{T}_3$ contributes significantly to ΔU^+. The simulations are at slightly different Re_τ, which generates setup-dependent contributions to this term. To isolate these effects, we propose an alternative breakdown, $\Delta U^+ =$

$T1 + T2 + T3$, where

$$T1 = -\left(\frac{\delta_s'^+}{\delta_r'^+}\int_{h^+}^{H^+} -\langle uv\rangle_r^+ \, dy^+ - \int_{h^+}^{H^+} -\langle uv\rangle_s^+ \, dy^+\right), \tag{4.6a}$$

$$T2 = U_r^+(h^+) - U_s^+(h^+), \tag{4.6b}$$

$$T3 = \left(\frac{\delta_s'^+}{\delta_r'^+} - 1\right)\int_{h^+}^{H^+} -\langle uv\rangle_r^+ \, dy^+ \underbrace{-\frac{1}{2}\left(\frac{H^{+2} - h^{+2}}{\delta_r'^+} - \frac{H^{+2} - h^{+2}}{\delta_s'^+}\right)}_{\mathcal{T}_3}. \tag{4.6c}$$

These expressions are obtained by adding and subtracting $\delta_s'^+/\delta_r'^+ \int \langle uv\rangle_r^+$ to equation (4.5), and rearranging. In this form, the term $|T3| \ll |T1|, |T2|$, and the expression $\Delta U^+ = \mathcal{T}_1 + \mathcal{T}_2$ is still recovered for $\delta_r'^+ = \delta_s'^+$. By rescaling $-\langle uv\rangle_r^+$ by the ratio of channel heights, δ_s^+/δ_r^+, T1 is less dependent to small variations of the frictional Reynolds number, and thus cases with slightly different δ^+ can be more fairly compared. Results of equations (4.6) used on our rough geometries are portrayed in figure 4.2. The term T1 contributes the most towards ΔU^+. In our geometries, the term T2 is observed to always be negative, as shown in figure 4.2. However, some particular cases with two-dimensional roughness, such as riblets, have also proven to induce a positive, and therefore drag reducing, T2 term (García-Mayoral and Jiménez, 2011).

For $\delta_r^+ = \delta_s^+$, equations (4.5) and (4.6) simplify to

$$T1 = \mathcal{T}1 = \int_{h^+}^{\delta_s'^+} \left(\langle uv\rangle_r^+ - \langle uv\rangle_s^+\right) \, dy^+, \tag{4.7a}$$

$$T2 = \mathcal{T}2 = U_r^+(h^+) - U_s^+(h^+). \tag{4.7b}$$

Equations (4.7) present in a clearer manner the components of ΔU^+, as it is caused by the change in Reynolds stress as well as the difference between the mean velocity at the roughness crests and that over an reference smooth wall at the same height from the virtual origin.

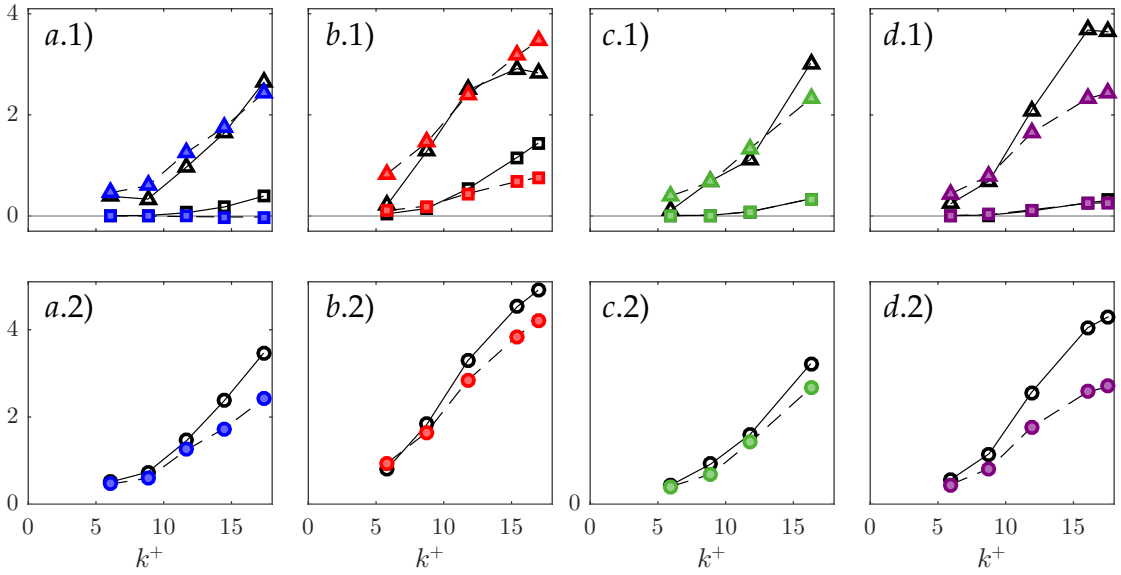

Figure 4.3.: Results from the direct numerical simulations and the estimates based on equations (4.7). ●, ΔU^+; ▲, $\mathcal{T}_1$; ■, $\mathcal{T}_2$. (*a*), collocated posts; (*b*), collocated posts of two heights; (*c*), posts staggered along *z*; and (*d*), posts staggered along x. Solid symbols, estimates; empty symbols, direct numerical simulations.

4.2. Model for the roughness function

Now we explore the potential of equations (4.7) for predicting ΔU^+. Based on the discussion in §3.2 and §3.3, we suggest a model for the contributions $\mathcal{T}_1$ and $\mathcal{T}_2$ to estimate ΔU^+. Let us assume that the statistics for a turbulent flow over a smooth wall at the desired Re_τ are available. Therefore, only the terms from roughness, $U_r^+(h^+)$ and $\langle uv\rangle_r^+(y^+)$, need to be modelled. For small roughness size, the velocity at the roughness crests, $U_r^+(h^+)$, can be estimated from the laminar model for the coherent flow presented in section 3.2. In §3.3 it is shown how for small k^+ the main effect of roughness on the Reynolds stress, $\langle uv\rangle_r^+$, is as a shift ℓ_{uv}^+ towards the wall, but otherwise the Reynolds stress closely resembles that of smooth-wall turbulence. As a result the effective displacement of the Reynolds stress is $\ell_{uv}^+ - \ell_U^+$, since the origin is at a depth ℓ_U^+ below the roughness tips. We can express this relation as if the Reynolds stress of a rough wall was that of smooth-wall turbulence shifted to the corresponding virtual origin, i.e. $\langle uv\rangle_r^+(y^+) \approx \langle uv\rangle_s^+(y_\star^+)$, where $y_\star^+$ is an auxiliary wall-normal coordinate that

displaces $\langle uv\rangle_s^+$. This auxiliary coordinate $y_\star^+$ is defined such that near the wall, at $y_r^+ = h^+$, $\langle uv\rangle_r^+(y_r^+ = h^+) \approx \langle uv\rangle_s^+(y_r^+ = h^+ + \ell_{uv}^+ - \ell_U^+)$. Notice that a mere shift of $\langle uv\rangle_s^+$ leads to a new δ'^+. Instead, to keep δ'^+ constant, $y_\star^+$ is linearly transformed, with $\langle uv\rangle_r^+(y_r^+ = \delta'^+) \approx \langle uv\rangle_s^+(y_r^+ = \delta'^+)$. The change in Reynolds stress, accounted for in the term $\mathcal{T}_1$, can therefore be expressed as

$$\mathcal{T}_1 \approx \int_{h^+}^{\delta^+} \left(\langle uv\rangle_s^+(y_\star^+) - \langle uv\rangle_s^+(y^+)\right)\, dy^+, \tag{4.8}$$

where

$$y_\star^+ = \left(\frac{\delta'^+ - \ell_{uv}^+}{\delta'^+ - \ell_U^+}\right)(y_r^+ - \ell_U^+) + \ell_{uv}^+. \tag{4.9}$$

Results of this model are portrayed in figure 4.3. In addition, the values of h_r^+ and U_0, used to estimate $\mathcal{T}_2$, are estimated from the laminar model for the roughness-coherent contribution, presented in §3.2. The model appears to estimate the initial trend of ΔU^+ with relatively good agreement up to values of $-\Delta U^+ \lesssim 2$, i.e. capturing the region of initial increase of drag with $\Delta C_f/C_f \lesssim 25\%$. For larger roughness, the results begin to deviate more significantly. These results show the potential of the model described by equations (4.7) and (4.8) to estimate ΔU^+ as it departs from the hydraulically smooth regime.

4.3. Conclusions and discussion

In the present chapter, the roughness function has been divided into two main contributions: the change in Reynolds stress; and the difference between the mean velocity at the roughness crests and that over smooth-wall at the equivalent height over the virtual origin. If the reference smooth-wall data at a different Reynolds number is used, a third term needs to be accounted for. Using this decomposition, a model for the roughness function is proposed. The results show the potential of this model to approximate ΔU^+ as it departs from the hydraulically smooth regime. Further work needs to be undertaken in order to extend the model to the entire transitionally rough regime, as well as to obtain an estimate for ℓ_{uv}^+. Additionally, its applicability to random roughness must be analysed, especially for the purpose of industrial applications.

5. Shear-flow instability

Part of the content of this chapter has been published in N. Abderrahaman-Elena and R. García-Mayoral (2017). 'Analysis of anisotropically permeable surfaces for turbulent drag reduction'. Phys. Rev. Fluids *2 (11), p. 114609.*
Part of the content of this chapter has been published in N. Abderrahaman-Elena et al. (2019). 'Modulation of near-wall turbulence in the transitionally rough regime'. J. of Fluid Mech. *865, pp. 1042–1071.*

In chapter 3, we have observed how the energy spectra is modified by roughness of increasing size. Energy at small λ_x^+ and large λ_z^+ increases in a fashion reminiscent of that in riblets. In the case of riblets, those modifications were found to be produced by a shear-flow instability (García-Mayoral and Jiménez, 2011). In this chapter, we explore whether such instability develops in transitional roughness. First, the stability of the mean velocity profile of our results from direct numerical simulations is analysed. Then, to overcome the need for complete simulations, we use a similar approach to that in García-Mayoral and Jiménez (2011), where the roughness surface is modelled by an impedance-like equation in the stability equation. For vanishingly small and densely packed roughness, we assume that the surface can be approximated by the equations for a permeable substrate. These results also lead to an a priori study on permeable substrates, which is presented in chapter 6.

5.1. Shear-flow instability over roughness

In section 3.3, we discuss the changes in the spectra for increasing roughness size. The spectral energy densities in figure 5.1 indicate the regions where en-

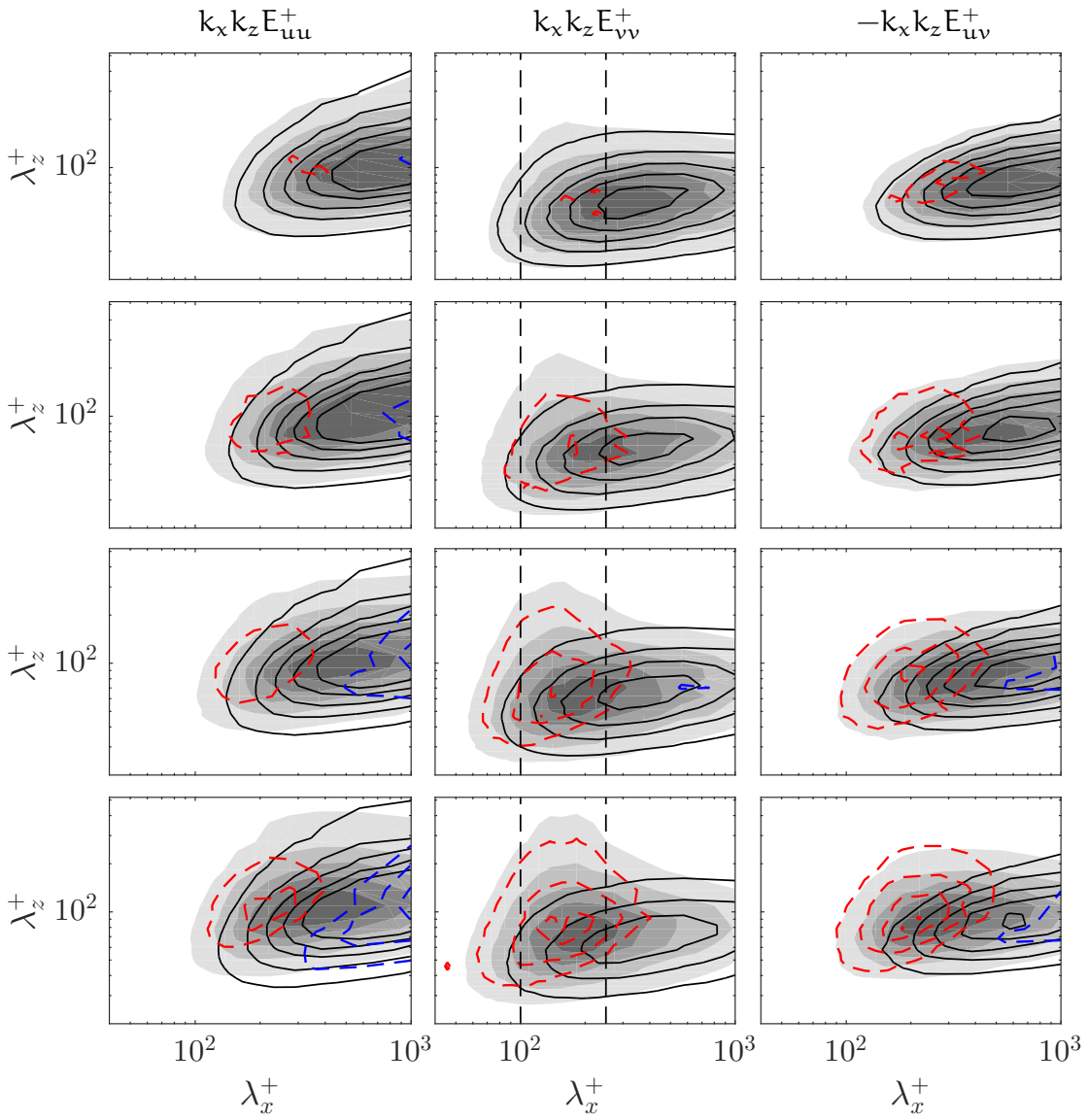

Figure 5.1.: Shaded, two-dimensional premultiplied spectrum of the streamwise and wall-normal velocity components, and cospectrum of the Reynolds shear stress. —, corresponding spectrum for smooth-wall turbulence, at the equivalent height accounting for the virtual origins, and using the same contour levels. – –, positive and, – –, negative difference between the rough and smooth-wall results. From top to bottom cases C12, C15, C18 and C24, at $y^+ = 8$. Same contour levels as in figure 3.15

ergy increases or decreases with respect to smooth wall turbulence. Energy increases at short streamwise wavelengths, λ_x, for a broad range of λ_z, both larger and smaller than the characteristic λ_z of smooth-wall turbulence. The values of λ_x at which energy increases, $\lambda_x^+ \approx 100$–200, appear to be independent of k^+. Although significantly more intense, similar modifications of the energy spectra were observed on riblets, a particular case of roughness. This increase in energy was found to be due to the formation of a shear flow instability (García-Mayoral and Jiménez, 2011). These instabilities are a common feature in obstructed flows (Ghisalberti, 2009), and have been observed on flows over plant canopies (Finnigan, 2000) and permeable substrates (Breugem et al., 2006). Although we do not observed them directly in our numerical simulations, the concentration of energy for a narrow range of λ_x^+ suggests a receptivity to this wavelengths that could be connected to a similar shear-flow instability of the mean velocity profile, for which we analyse the stability properties in this section.

Numerical works by Jiménez et al. (2001), and more recently by Abderrahaman-Elena and García-Mayoral (2017) and Gómez-de-Segura et al. (2018b), have shown that the wall-normal transpiration plays a dominant role on the onset of such instability. Gómez-de-Segura et al. (2018b) have observed substantial changes on the spectra even for very low wall-normal permeabilities. Similarly, roughness enhances wall-normal velocity fluctuations, as well as allows the flow to penetrate below the roughness crests, yielding a slight transpiration effect. Notice however, that in our results the energy associated to this change in the spectra is low, and therefore its development does not seem to be the main source of drag increase in roughness, conversely to flows over permeable surfaces (Gómez-de-Segura et al., 2018a) and riblets (García-Mayoral and Jiménez, 2011).

We focus on Kelvin-Helmholtz-like instabilities, which are essentially spanwise coherent, linear and inviscid. Previous studies have shown that the inviscid instability is essentially a property of the mean profile (Beneddine et al., 2016), although it is modulated by the effect of the complex substrate on the fluctuating flow (Raupach et al., 1991; White and Nepf, 2007; Zampogna et al., 2016), as well as by viscous effects (Jiménez et al., 2001; Luminari et al., 2016; Gómez-de-Segura et al., 2018c). Since we aim to assess this phenomenon only qualitatively, we conduct a simplified analysis, two-dimensional in x and y, inviscid and lin-

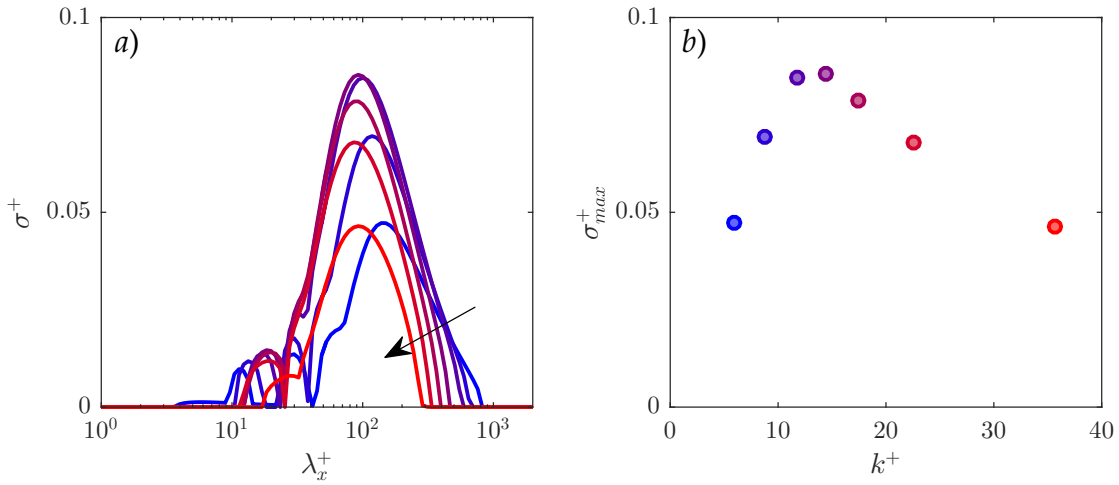

Figure 5.2.: (*a*) Growth rate $\sigma^+ = \mathrm{Im}\,(\alpha_x^+ c)$ of the most amplified mode as a function of the longitudinal wavelength λ_x^+. (*b*) Maximum growth rate σ^+ as a function of the roughness height. Blue to red, results for the mean velocity profiles for cases C06 to C36.

ear, where the flow is allow to fluctuate freely around the mean profile, neglecting the presence of the solid obstacles. We seek wavelike solutions for the velocity and pressure perturbations, of the form $f = \hat{f}\exp[i(\alpha_x x + \alpha_z z - \omega t)]$, which allows for a modal analysis. The linearised problem becomes then Rayleigh's equation (Rayleigh, 1879)

$$\left((U - c)(\partial_{yy} - \alpha_x^2 - \alpha_z^2) - \partial_{yy} U\right)\hat{v} = 0, \tag{5.1}$$

where α_x and α_z are the wave numbers in the streamwise and spanwise directions respectively, $\hat{v}$ is the corresponding perturbation mode of the wall-normal velocity, with $\hat{v} = 0$ at the bottom of the troughs, and c is the complex phase velocity. Note that, according to Squire's theorem, for any streamwise wavelength α_x the most amplified mode is two-dimensional, $\alpha_z = 0$. The mean velocity profiles, U, are directly extracted from our DNSs, and include the region below the roughness crests. Notice that the effect of roughness is exclusively introduced through the mean velocity profile. More precise studies include, for instance, a drag force model below the roughness or canopy tips (Py et al., 2006; Luminari et al., 2016; Sharma et al., 2017), at the cost of an increased cost and complexity.

The results of the stability analysis, portrayed in figure 5.2(*a*), show an instability for the mean flow predominantly for wavelengths $\lambda_x^+ \approx 100$–150. This result is in rough agreement with the modifications observed in the energy spectra and cospectra in figure 5.1, where energy concentrates at $\lambda_x^+ \sim 150$, and does not significantly change with k^+. This could be expected, as previous studies have shown that the lengthscales of the instability are set by the shape of the mean velocity profile, independently of the lenghtscales in the substrate geometry (White and Nepf, 2007; García-Mayoral and Jiménez, 2011; Gómez-de-Segura et al., 2018c). However, our simplified model exhibits a maximum for the instability at $k^+ \approx 15$, as depicted in figure 5.2(*b*), while the changes in the energy spectra increase monotonically with k^+, as can be observed in figure 5.1. Nevertheless, the results suggest that the wavelengths in which energy concentrates in the DNSs are the most receptive from the point of view of the stability of the mean flow.

5.2. A stability model based on porous materials

The analysis in the previous section relies on the mean velocity profiles obtained from direct numerical simulations to study the stability of the flow. Instead, García-Mayoral and Jiménez (2011) study the stability of a turbulent flow over riblets by modelling the interaction with the surface as a boundary condition to the stability equation. Based on that approach, we propose a model to predict the onset of the shear-flow instability discussed in section 5.1 over a generic rough surface. The flow dynamics are modelled within the roughness canopy, and its effect is applied to the outer flow in the form of an impedance equation. We assume that the roughness elements are small and densely packed such that the properties of the roughness surface can be consider as a homogeneous region. This region is then modelled as a porous substrate whose permeability depends on the characteristics of the surface to model. We consider an anisotropically permeable layer as that depicted in figure 5.3, characterised by its thickness, h, and its streamwise, wall-normal and spanwise permeabilities, K_x, K_y and K_z, respectively, which are assumed to be along the principal directions of the permeability tensor, K. Notice that the thickness of the layer, h, is a mere parameter

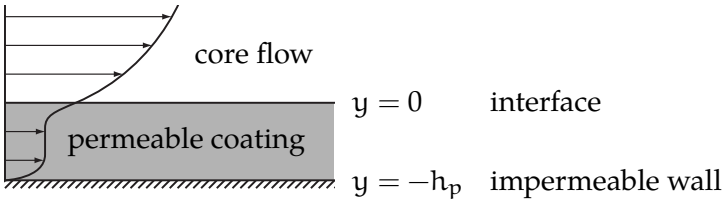

Figure 5.3.: Schematic representation of a permeable layer for drag reduction.

of the model, and is in principle different from $k_,$. We assume that the substrate is formed by a matrix of obstacles much smaller than any infinitesimal volume relevant to our problem so that homogenisation can be applied on any arbitrarily small volume within the substrate (Zampogna and Bottaro, 2016; Lācis and Bagheri, 2017). The permeability could decrease by increasing the number of obstacles, rather than their size, and vice versa. Under these conditions, the inertial terms are negligible and the resulting Stokes flow within the cavities can be volume-averaged to yield the Darcy equation (Darcy, 1856),

$$\nu K^{-1} \boldsymbol{u} + \nabla p = 0. \tag{5.2}$$

Darcy's equation is an adequate model for the flow in the core of the permeable material, but fails to represent the flow in the vicinity of impermeable walls or at the interface with an outer free flow. Gómez-de-Segura et al. (2018b) perform the stability analysis of a permeable coating modelled by the Darcy-Brinkman equation (Brinkman, 1947). Their results are qualitatively similar to those presented here, as the Kelvin-Helmholtz instability is inviscid.

5.2.1. Model from linear instability

To capture the onset of the shear-flow instability, we propose a model based on the linear stability analysis of the mean flow in a turbulent channel with symmetric permeable walls. Mean-flow analysis has been shown to adequate capture instabilities, and in particular Kelvin-Helmholtz rollers, in flows with a fluctuating turbulent component (Beneddine et al., 2016; Tammisola and Juniper, 2016), and has been extensively used in turbulent flows over complex sur-

faces (Jiménez et al., 2001; Py et al., 2006; Dupont et al., 2010; García-Mayoral and Jiménez, 2011). Here we closely follow the methodology of Jiménez et al. (2001) and García-Mayoral and Jiménez (2011).

Kelvin-Helmholtz instabilities are essentially inviscid and linear, and can therefore be captured by the equations for linearised inviscid perturbations (Jiménez et al., 2001; Py et al., 2006), with the fully viscous analysis showing no fundamental difference in the results (Jiménez et al., 2001; Luminari et al., 2016). Therefore, we restrict our analysis to the inviscid case. We conduct the analysis on the flow outside the permeable substrate, and the influence of the substrate appears as a boundary condition at the interface, provided by the analytical solution of the underlying flow, detailed below.

As in section 5.1, we seek solutions for equation (5.1). The difference between the present analysis and the previous case lies in the presence of the permeable substrate, which imposes an impedance-like boundary condition on the core flow (Jiménez et al., 2001; García-Mayoral and Jiménez, 2011; Scalo et al., 2015). To derive the boundary condition, we focus on the response of the flow within the permeable medium to the overlying pressure fluctuations, $\hat{p}|_{y=0^+}$. Since Kelvin-Helmholtz is an inviscid instability, the perturbation field of the overlying flow is assumed to be inviscid, so it cannot exert any shear on the flow below, which is therefore free to slip with respect to the external velocity.

Let us now consider the flow within the substrate on the bottom wall of the channel, which extends from $y = -h_p$ to $y = 0$. The flow is described by equation (5.2), which, combined with incompressibility, leads to a Poisson equation for $\hat{p}$. Assuming impermeability at $y = -h_p$, the solution is a function of the value of $\hat{p}$ at $y = 0$,

$$\hat{p} = \hat{p}_0 \left[\tanh\left(\widetilde{\alpha}\, h_p\, \Phi_{xy}\right) \sinh\left(\widetilde{\alpha}\, y\, \Phi_{xy}\right) + \sinh\left(\widetilde{\alpha}\, y\, \Phi_{xy}\right)\right], \tag{5.3}$$

where $\Phi_{xy} = \sqrt{K_x/K_y}$ is the streamwise-to-wall-normal anisotropy ratio, $\widetilde{\alpha}^2 = \alpha_x^2 + \alpha_z^2 K_z/K_x$, and the subscript v_0 and p_0 are magnitudes of wall-normal velocity and pressure at the interface, $y = 0$. This solution can be introduced in the

Darcy equation for the wall-normal velocity, giving

$$\hat{v}_0 = -\widetilde{\alpha}\left[\nu^{-1}\sqrt{K_x K_y}\tanh(\widetilde{\alpha}\, h_p\, \Phi_{xy})\right]\hat{p}_0. \tag{5.4}$$

Equation (5.4) can be used as an impedance boundary condition in the stability analysis of the overlying flow. On the top wall of the channel, an analogous impedance condition can be obtained, resulting in the same form of equation (5.4), but reversed in sign.

As in Jiménez et al. (2001) and Tilton and Cortelezzi (2008), Squire's transformation (Squire, 1933) reduces the problem of equations (5.1) and (5.4) to an equivalent spanwise-homogeneous, two-dimensional problem with $\alpha_{x,2D} = \widetilde{\alpha}$, $\alpha_{z,2D} = 0$, and modified permeabilities. The equivalent problem has lower permeabilities than the spanwise-homogeneous, two-dimensional problem with $\alpha_x = \alpha_{x,2D}$ and $\alpha_z = 0$ and, as shown below, reducing the permeabilities has a stabilising effect. Consequently, we will only consider solutions with $\alpha_z = 0$, as for each α_x they are the most amplified. Note that this is in agreement with the observed Kelvin-Helmholtz structures being predominantly spanwise-coherent (García-Mayoral and Jiménez, 2011; Ghisalberti, 2009; Jiménez et al., 2001; Finnigan, 2000).

5.2.2. Results for a piecewise-linear mean velocity profile

Before turning our attention to a quantitative analysis using turbulent mean profiles as base flows, it is useful to study a piecewise-linear one

$$U(y) = \begin{cases} U_\infty\, y/H_p & \text{for } y < H_p, \\ U_\infty & \text{for } y \geqslant H_p. \end{cases} \tag{5.5}$$

The solution using this profile is algebraic, and the basic mechanisms are more easily understood. Note that the base flow has $\partial_{yy}U = 0$ everywhere except at $y = H_p$, where it becomes singular. Equations (5.1) and (5.4) lead then to a second order equation for the complex phase velocity, c,

$$-2\mathcal{K}\sigma^2 + \left[-2i + \mathcal{K}\left(1 + 2\alpha_x' - e^{-2\alpha_x'}\right)\right]\sigma + (\mathcal{K} - i)\left(1 - 2\alpha_x' - e^{-2\alpha_x'}\right) = 0, \tag{5.6}$$

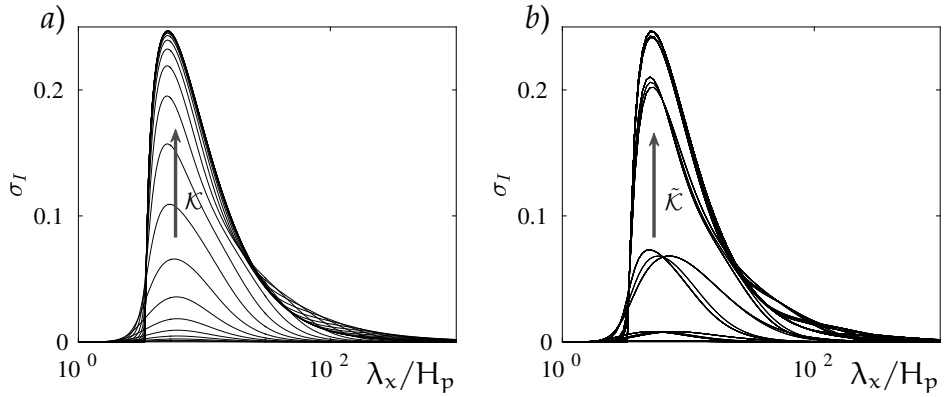

Figure 5.4.: Growth rate $\sigma_I = \mathrm{Im}(\sigma)$ of the most amplified modes given by (5.6). (a) Isotropic case with $\Phi_{xy} = 1$ and $h_p/H_p = 1$ Curves are shown for $(\sqrt{K_x K_y}/H_p^2)(UH_p/\nu) = 10^{[-2(0.4)6]}$. (b) Anisotropic case obtained using all possible combinations of $h_p/H_p = 10^{[-1,0,1]}$ and $\Phi_{xy} = 10^{[-3(1)3]}$. Curves are shown for $\widetilde{\mathcal{K}} = 10^{[-2(1)6]}$.

where $\alpha_x' = \alpha_x H_p$, $\sigma = \alpha_x' c/U_\infty$ and

$$\mathcal{K} = \frac{\sqrt{K_x K_y}}{H_p^2}\left(\frac{U_\infty H_p}{\nu}\right)\tanh\left(\alpha_x'\frac{h_p}{H_p}\Phi_{xy}\right). \tag{5.7}$$

Results of equation (5.6) are shown in figure 5.4(*a*) as a function of $\mathcal{K}$. The limit $\mathcal{K} \gg 1$ provides a physical interpretation of the nature of the instability. In this limit, the boundary condition (5.4) is equivalent to $p(0) = 0$, which can be reduced to $\partial_y \hat{v}(0) = 0$, and enforces symmetry on the perturbation flow. This gives the same solution as extending the base profile antisymmetrically about $y = 0$. The problem becomes then that of the instability of a shear layer, whose solutions are the Kelvin-Helmholtz unstable waves of a free shear layer. In the opposite limit, $\mathcal{K} \ll 1$, the neutrally stable solution of smooth, impermeable walls is asymptotically approached. The intermediate values of $\mathcal{K}$ connect the Kelvin-Helmholtz solution with the stable solution for the impermeable case.

Expression (5.7) depends not only on the properties of the porous substrate, but also on the reduced spectral wavenumber α_x', which is not a physical property of the permeable layer but part of the solution. In an attempt to remove the

dependency on the flow we propose the following empirical fit

$$\widetilde{\mathcal{K}} = \frac{\sqrt{K_x K_y}}{H_p^2} \left(\frac{U_\infty H_p}{\nu} \right) \tanh \left(\frac{h_p}{H_p} \Phi_{xy} \right). \tag{5.8}$$

Figure 5.4(*b*) shows results, as a function of $\widetilde{\mathcal{K}}$, for several combinations of K_x, K_y and h_p. For the same values of $\widetilde{\mathcal{K}}$, solutions for different coatings agree well, except perhaps for low values of $\widetilde{\mathcal{K}}$, for which the instability is not fully developed. Other than for those low values, the parameter $\widetilde{\mathcal{K}}$ encompasses the combined influence of K_x, K_y and h_p. Note that, while the amplification is determined by $\widetilde{\mathcal{K}}$, the most amplified wavelength does not scale with the characteristic permeability length scale, $\sqrt{K_x}$ or $\sqrt{K_y}$. As in García-Mayoral and Jiménez (2011), the wavelength scales with the height $y = H_p$ of the singularity in $\partial_{yy} U$, that is, it is determined by the shape of the base flow.

5.2.3. Results for turbulent mean velocity profile

Although the analysis on the piecewise-linear velocity profile provides qualitative information on the nature of the instability, quantitative results require more realistic profiles. We use approximate turbulent mean profiles as in Jiménez et al. (2001), Dupont et al. (2010) and García-Mayoral and Jiménez (2011). In particular, we use the profiles of Cess (1958), which have previously been used for flow stability analysis by Reynolds and Tiederman (1967) and more recently by del Álamo and Jiménez (2006). In contrast with the linear profile used in the previous section, the stability problem (5.1), with the boundary condition (5.4), does no longer lead to an algebraic expression, and the full generalised eigenvalue problem must be discretised and solved numerically. For every Fourier mode α_x the wall-normal direction is discretised using Chebyshev polynomials with 256 to 1536 collocation points, depending on the Reynolds number, which provide a resolution at the wall $\Delta y^+ \lesssim 0.01$. Obtaining insight from the solution becomes less straightforward, but some analogies can be established with the piecewise-linear results.

As in section 5.2.2, we find that the length scale of the problem is determined by the shape of the U-profile. The energy-producing term, $\partial_{yy} U$, is larger

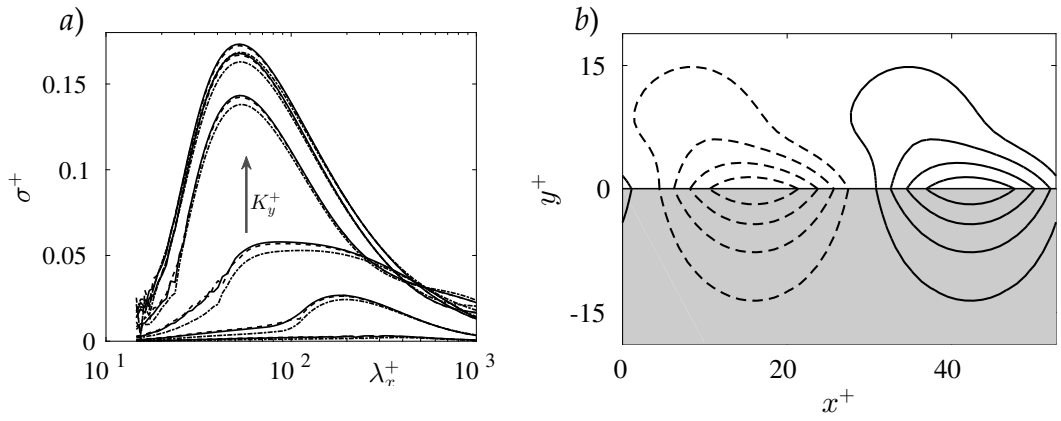

Figure 5.5.: (*a*) Growth rate $\sigma^+ = \alpha_x^+ \mathrm{Im}(c^+)$ of the most amplified mode as a function of the longitudinal wavelength λ_x^+. Isotropic case $\Phi_{xy} = 1$, $K^+ = 10^{[-0.66(0.66)2.66]}$, $h_p^+ = 100$. -·- , $Re_\tau = 180$; -- , $Re_\tau = 550$; — , $Re_\tau = 1000$. (*b*) Streamfunction contours of the mode with highest growth rate at $Re_\tau = 550$ for fully developed instability, $\widetilde{K}^+ = 10^4$. Solid and dashed lines correspond to clockwise and counter-clockwise rotation, respectively.

between $y^+ = 5$ and 20, peaking near $y_c^+ \approx 8$, which plays the same role as the singularity at $y = H_p$ for the piecewise-linear profile (García-Mayoral and Jiménez, 2011). This height is independent of the Reynolds number when scaled in wall-units, and is responsible for the inner scaling of the instability observed in figure 5.5(*a*). The solution, portrayed in figure 5.5(*a*) for isotropic substrates, is qualitatively similar to the one for the piecewise-linear profile, evolving as the permeability increases from the neutral, smooth-wall solution to increasingly amplified solutions, and eventually reaching a limit solution for high permeabilities.

We are particularly interested in the most amplified mode for each surface configuration, as this will be the most prevalent (Jiménez et al., 2001; García-Mayoral and Jiménez, 2011). This mode forms rollers turning alternatively clockwise and counter-clockwise which penetrate into the porous material below $y^+ = 0$, as portrayed in figure 5.5(*b*).

As in section 5.2.2, we aim to describe the solution using a simplified characterising parameter. By analogy with equation (5.8) we propose

$$\widetilde{K}^+ = \sqrt{K_x^+ K_y^+}\tanh\left(\frac{h_p^+}{y_c^+}\Phi_{xy}\right). \tag{5.9}$$

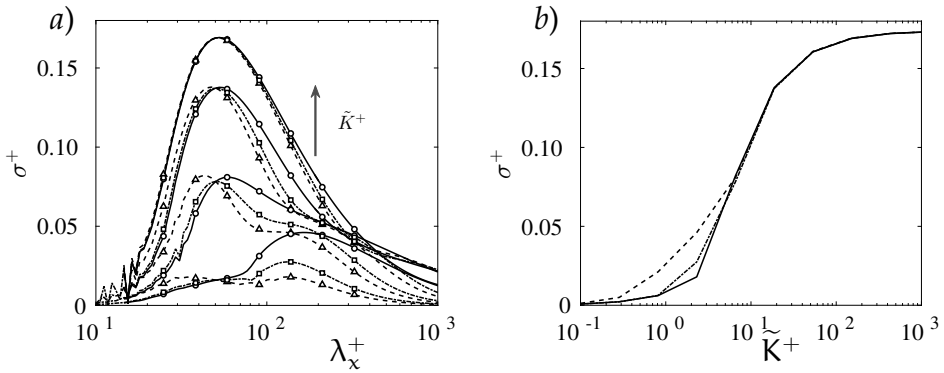

Figure 5.6.: (*a*) Growth rate $\sigma^+ = \alpha_x^+ \mathrm{Im}(c^+)$ of the most amplified mode as a function of the longitudinal wavelength λ_x. $\widetilde{K}^+ = 10^{[0.36,\ 0.82,\ 1.28,\ 2.20]}$ at $Re_\tau = 550$. —, $\Phi_x = 10^{-3}$, $h_p^+ = 10$; - -, $\Phi_x = 10^3$, $h_p^+ = 10$; △, $\Phi_x = 1$, $h^+ = 1$; ○, $\Phi_x = 1$, $h_p^+ = 100$; □, $\Phi_x = 1$, $h^+ = 10$. (*b*) Maximum growth rate σ^+ as a function of the permeability $\widetilde{K}^+$ at $Re_\tau = 550$. — $\Phi_x = 10^{-3}$, $h_p^+ = 1$; - - $\Phi_x = 10^3$, $h_p^+ = 100$; -·- $\Phi_x = 1$, $h_p^+ = 10$.

Figure 5.6(*a*) illustrates how scaling with this parameter results in a reasonable collapse for different K_x^+, K_y^+ and h_p^+. For high values of $\widetilde{K}^+$ there is good agreement, while for low values we observe some scatter depending on the value of $h_p^+ \Phi_{xy}$. The growth rate of the most amplified mode for each set of parameters is portrayed separately in figure 5.6(*b*) as a function of $\widetilde{K}^+$, showing that the effect of the modulation with $h_p^+ \Phi_{xy}$ is small, and only appears for low permeabilities $\widetilde{K}^+ \lesssim 5$. García-Mayoral and Jiménez (2011) found a similar S-shaped curve for the relationship between σ^+ and the characteristic length scale of riblets. In their case, the degradation of drag reduction cause by the onset of this instability was observed to roughly coincided with the sharp transition between the quasi-neutral and the fully amplified regimes. They suggested that the model could therefore be used as an indicator for the onset of Kelvin-Helmholtz-like rollers, and to obtain estimates for the riblet size, in viscous units, for which the degradation of drag would roughly set in.

In the present case, the transition between the quasi-neutral and fully amplified regimes occurs at $\widetilde{K}^+ \approx 5 - 10$. Note that, beyond $\widetilde{K}^+ = 5$, the scatter for low values of $\widetilde{K}^+$ discussed above is not significant. Hence, $\Phi_{xy} h_p^+$ should have little effect on the triggering of the instabilty. For that reason, the term $\tanh(\Phi_{xy} h_p^+ / y_c^+)$ in expression (5.9) can be approximated by its rapidly approached

limit, $\tanh(\Phi_{xy} h_p^+ / y_c^+) \approx 1$, taking into account that $y_c^+ \approx 8$ and that for the configurations of practical interest $\Phi_{xy} \gg 1$ and $h_p^+ \gtrsim 10$. The criterion for the onset of the Kelvin-Helmholtz-like instability can then be roughly set to

$$\widetilde{K}_{KH}^+ \approx \sqrt{K_x^+ K_y^+} \approx 5 - 10. \tag{5.10}$$

For flows over permeable substrates of diverse depth and permeability, it is difficult to find details of the structure of the near-wall flow in the literature. Breugem et al. (2006) reported the appearance of Kelvin-Helmholtz rollers at $\widetilde{K}^+ \approx 80$. Zampogna et al. (2016), on their permeable layer model for canopy flow, also observe rollers at $\widetilde{K}^+ \approx 300$. It is worth noting that, although Rosti et al. (2015) did not observe Kelvin-Helmholtz rollers directly in their simulations, with $\widetilde{K}^+ < 1$, they observed a weak Kelvin-Helmholtz signal in their velocity correlations. This is in agreement with the very low amplification that our model predicts for low $\widetilde{K}^+$, and the results in section 5.1.

5.2.4. Comparison with roughness results

This model based on a permeable coating, assuming small and densely packed roughness, shares similarities with the behaviour observed in section 5.1. The model describes a shear-flow instability potentially setting in beyond a permeability threshold. Notice that in the limit of vanishingly small size, the permeability of the surface can, in principle, be related to the size and arrangement of the roughness elements. Therefore, an increase in roughness size can be somewhat thought of as an increase in pore size and, as a result, an increase in permeability.

The model, however, does not describe the decrease in amplification observed in figure 5.2(*b*). Sharma et al. (2017) study the stability of canopy flows using two different models. They found that their impedance-like model, as the one used in this work, is capable to predict the increase in growth rate but not the later decrease. They also proposed a drag model, where the flow within the canopies is also included in the integration domain of Rayleigh's equation, that captures both the increase and later decrease of the growth rate of the instability. The difference between these models lay in the impedance-like approach not account-

ing for the change in fluctuations within the roughness surface or canopy. On the other hand, the drag model is a better approximation of how the roughness elements interact with flow fluctuations damping their intensity.

Notice that in the model presented in this work, we rely on the parameters that characterise the surface, K_x, K_y, K_z and h_p. This parameters could, in principle, be predicted using, for instance, homogenisation techniques (Zampogna and Bottaro, 2016; Lācis and Bagheri, 2017) or laminar models similar to the one proposed in chapter 3, however, this is left for future work.

5.3. Conclusions and discussion

In this chapter, we have studied the possible origin of the changes in the spectra observed in the previous chapter 3, in particular, the increase in energy at small λ_x^+. In the riblets literature, a somewhat similar change in the spectra was found to be produced by the shear-flow instability induced by the surface (García-Mayoral and Jiménez, 2011). In the case of riblets, the intensity of the instability can develop Kelvin-Helmholtz-like structures in the form of strongly coherent, spanwise rollers superimposed to the background turbulent flow. Therefore, we have studied the stability of mean velocity profile of one of our roughness surfaces. This profiles have also been found to be linearly unstable, with the wavelength of this instability agreeing well with that at which the increase in energy is observed in the spectra from direct numerical simulations. Notice that that wavelength is governed by the local shear at the surface and not directly by the roughness size. This is in agreement with the small variations in the wavelength at which energy increases in the energy spectra, which remains approximately constant, $\lambda_x \approx 150$, for increasing k^+. However, in any event, the shear-flow instability is weak, and not intense enough to develop rollers directly observable in instantaneous realisations of the flow field, conversely to some regimes of riblets and plant canopies in which they are stronger.

To extend this analysis without relying on results from direct numerical simulations, we then use a similar approach to that by García-Mayoral and Jiménez (2011) in riblets, where the surface is modelled as an impedance-like boundary condition for Rayleigh's equation. The model describes the unstable behaviour

setting in beyond a certain permeability threshold. Notice that an increase in k^+ would also produce an increase on its equivalent permeability. Therefore, these results are consistent with those in section 5.1, for increasing roughness height. On the other hand, this model does not capture the decrease in growth rate observed for sparse roughness.

The main drawback of this approach is finding a priori the parameters of the equivalent model, K_x, K_y, K_z and h_p, that characterise the surface studied. However, working on this model also presents an opportunity to study permeable surfaces in certain depth, which certainly display similarities with roughness. While conventional roughness increases drag, we find the particular case of riblets that reduce skin friction in part of the transitionally rough regime. In a similar fashion to conventional roughness, porous surfaces in turbulent flows generally increase skin friction (Darcy, 1856; Zagni and Smith, 1976). However, inspired by the idea that riblets are preferentially aligned roughness, anisotropic permeable substrates, also with a preferential flow direction, could yield drag reduction within some flow regimes. The concept of anisotropically permeable substrates is explored in the following chapter.

6. Analysis of anisotropically permeable surfaces for turbulent drag reduction

Part of the content of this chapter has been published in N. Abderrahaman-Elena and R. García-Mayoral (2017). 'Analysis of anisotropically permeable surfaces for turbulent drag reduction'. Phys. Rev. Fluids *2 (11), p. 114609.*

In chapter 5, we have drawn an analogy between roughness and permeable substrates. In the present chapter, we further explore this idea. Permeable substrates can be understood as idealised rough surfaces, where the characteristic size of the roughness elements is sufficiently small for the properties of the surface to be treated as homogeneous. In chapter 5, we showed that there is a threshold size beyond which a shear-flow instability develops, therefore potentially increasing drag. This phenomenon is also observed in riblets, which is actually the factor destroying their drag reducing effect (García-Mayoral and Jiménez, 2011). Expanding on the similarities between small size roughness and porous materials, we explore the use of anisotropically permeable substrates as a means to reduce turbulent skin friction in a similar fashion to riblets. We conduct an a priori analysis to assess the potential of these permeable surfaces, based on the effect of small-scale surface manipulations on near-wall turbulence. The goal is to propose a model, based on drag reduction theory combined with the linear stability analysis developed in the previous chapter, to find an upper bound to the maximum drag reduction that permeable substrates can achieve.

6.1. Anisotropically permeable substrates

In this chapter, we carry out an analysis of coatings with anisotropic permeability devised to reduce turbulent skin friction. We explore the possibility of using such coatings to produce the apparent slip that riblets (Walsh and Lindemann, 1984) or superhydrophobic surfaces (Rothstein, 2010) produce to reduce turbulent drag. Hahn et al. (2002) found that, in a similar fashion, streamwise-permeable walls reduce skin friction by creating an effective slip for the overlying turbulent flow. In their study, the walls were permeable in the streamwise and spanwise directions only, and impermeable in the wall-normal direction. They observed that high values of drag reduction were obtained with low or no spanwise permeability. Intuitively, the surface would then offer less resistance to longitudinal flow than to transverse flow, as riblets do (Luchini et al., 1991). Real materials cannot, however, be permeable in only certain directions, but they can have a preferential direction with higher permeability. The seal fur studied by Itoh et al. (2006) is, at least in part, an example of such anisotropically permeable material, as it is made up of fibres aligned preferentially in the streamwise direction. Such substrates produce a higher resistance for the cross-flow compared to the streamwise flow, and indeed Itoh et al. (2006) reported drag reduction properties similar to those of riblets, albeit slightly superior, as shown in figure 6.1. Previous studies have shown how a surface can reduce turbulent drag if it induces a streamwise-preferential effect (Luchini et al., 1991; Jiménez, 1994; Luchini, 1996). Taking some length-scale of the surface texture as reference, the drag reduction increases linearly with that length, when scaled in viscous units.

The theoretical framework developed in Luchini et al. (1991), Jiménez (1994) and Luchini (1996) assumes that the texture is vanishingly small compared to the length-scales in the flow. However, as the texture size increases, deleterious effects are observed and the performance saturates, as studied for riblets in García-Mayoral and Jiménez (2011) or for superhydrophobic surfaces in Seo et al. (2015) and García-Mayoral et al. (2014). The mechanisms for the onset of the deleterious effects vary, leading to more or less abrupt failures. These failures also occur for different texture sizes, depending on the type of surface.

In permeable substrates, one possible mechanism for the breakdown of drag

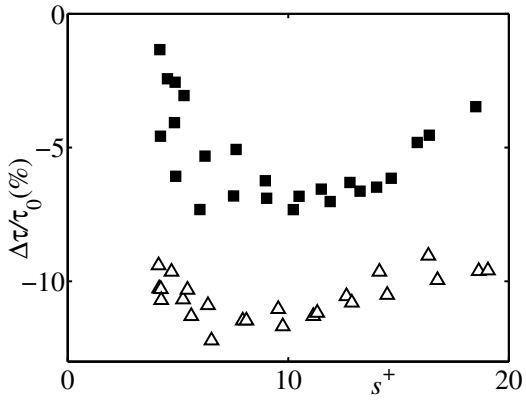

Figure 6.1.: Drag reduction, $DR = -\Delta\tau/\tau_0$, of the seal fur surface from Itoh et al. (2006). △, seal fur; ■, trapezoidal, flat-peak riblets, also from Itoh et al. (2006). For the seal fur, the wavelength identified by Itoh *et al.* by analogy with the riblet pitch, s^+, has been used to express their results in terms of a viscous length-scale. Taken from García-Mayoral (2011) with the permission from the author.

reduction is the appearance of spanwise coherent rollers over the surface. These are typical of turbulent flows over permeable surfaces when the permeability is large enough (Jiménez et al., 2001; Breugem et al., 2006; Rosti et al., 2015; Kuwata and Suga, 2016; Zampogna et al., 2016). While a substrate with a preferential streamwise permeability might yield the drag-reducing effect of Hahn et al. (2002) and Itoh et al. (2006), permeable surfaces have generally been reported to increase turbulent drag. This was the case in the DNS studies of Jiménez et al. (2001), where the wall was permeable in the wall-normal direction only, and of Breugem et al. (2006), where a substrate of packed particles with isotropic permeability was studied. In both cases, the large increase in drag was associated to the appearance of Kelvin-Helmholtz-like rollers, which enhance momentum transfer and increase the Reynolds stresses near the wall (García-Mayoral and Jiménez, 2011). It is worth noting that Jiménez et al. (2001) found that wall-normal permeability alone could trigger the appearance of spanwise rollers and increase drag. This suggests a competition between the beneficial, drag-reducing effect, driven by the longitudinal permeability, and the detrimental appearance of Kelvin-Helmholtz-like rollers, driven by the wall-normal permeability. The relaxation of the zero wall-normal velocity condition in com-

plex surfaces is generally responsible for the appearance of non-zero tangential Reynolds stress, increased mixing and thus increased friction (Orlandi and Jiménez, 1994; Orlandi, 2013). Kelvin-Helmholtz-like rollers appear frequently over complex substrates (Finnigan, 2000; Py et al., 2006; Coceal et al., 2007), and are indeed a common feature over a wide range of 'obstructing' surfaces (Ghisalberti, 2009). In riblets, they have been identified as the cause for the degradation of performance beyond the linear drag reduction regime, due to the additional Reynolds stresses that they generate (García-Mayoral and Jiménez, 2011). The resemblance of the drag curves for riblets and for the surface of Itoh et al. (2006), shown in figure 6.1, could suggest that the degradation is due to a similar mechanism. The apperance of a similar Kelvin-Helmholtz-like instability over conventional roughness in the transitionally rough regime has been studied in chapter 5. Here, we aim to characterise the linearly increasing drag reduction of surfaces with anisotropic permeability, but also to provide an upper bound, based on the development of Kelvin-Helmholtz-like rollers, for what would otherwise be an ever-increasing performance. Our study does not rule out the appearance of additional degrading phenomena, which could be triggered at smaller permeabilities and limit the drag reducing performance further. Nevertheless, the evidence on permeable substrates cited above strongly suggests that the spanwise rollers are a prevalent phenomenon and will eventually appear. The onset of rollers will therefore pose a limit to the maximum achievable performance and can be used to establish a performance bound a priori.

As in chapter 5, we consider an anisotropically permeable layer characterised by its thickness, h and its streamwise, wall-normal and spanwise permeabilities, K_x, K_y and K_z, which are assumed to be along the principal directions of the permeability tensor, K. If the inertial terms are negligible, then the resulting Stokes flow within the pores can be volume-averaged to yield the Darcy equation (Darcy, 1856),

$$\nu K^{-1}\boldsymbol{u} + \nabla p = 0, \tag{6.1}$$

6.2. Drag reduction mechanism

While for conventional smooth walls the velocity is zero at the wall, complex surfaces can yield non-zero velocities at their interface. For instance, the mean velocity at the roughness crests and at the interface between permeable materials and the free-flow is commonly greater than zero. This generates an apparent slip that can reduce drag. The theory for the underlying mechanism was proposed by Luchini et al. (1991), Jiménez (1994) and Luchini (1996). When the surface texture is vanishingly small with respect to the length scales characterising wall turbulence, the overlying turbulent eddies are comparatively very large and slow, and the shear that they induce over the wall is quasi-homogeneous and quasi-steady sufficiently away from the wall, typically a few texture heights. Above this height, the effect of the surface can be reduced to an effective slip condition at a notional wall plane, for instance the mean interface plane or the streamwise virtual origin. In the streamwise and spanwise directions, we can express the slip condition in terms of the corresponding slip lengths

$$u|_{y=0} = \ell_x \left.\frac{\partial u}{\partial y}\right|_{y=0}, \quad w|_{y=0} = \ell_z \left.\frac{\partial w}{\partial y}\right|_{y=0}, \tag{6.2}$$

where ℓ_x and ℓ_z are the streamwise and spanwise slip lengths, as depicted in figure 6.2. In viscous units, the resulting mean streamwise slip velocity at the wall is $U_s^+ = \ell_x^+$, so both slip length and slip velocity can be used interchangeably. In riblet literature, the slip lengths ℓ_x^+ and ℓ_z^+ are also referred to as protrusion heights (Bechert and Bartenwerfer, 1989; Luchini et al., 1991), interpreting them as the depth below the wall where the uniform, overlying shear would be extrapolated to zero, that is, where the virtual origin for the corresponding velocity profile would lie.

When the surface is anisotropic, ℓ_x^+ and ℓ_z^+ can be different. In the case of riblets, Luchini et al. (1991) identified this difference as responsible for their drag-reducing capability. Jiménez (1994) later generalised this result to any surface producing different streamwise and spanwise slip lengths, so long as they remain small compared to the typical length scales of near-wall turbulence.

We should note that for permeable substrates the theory assumes that the

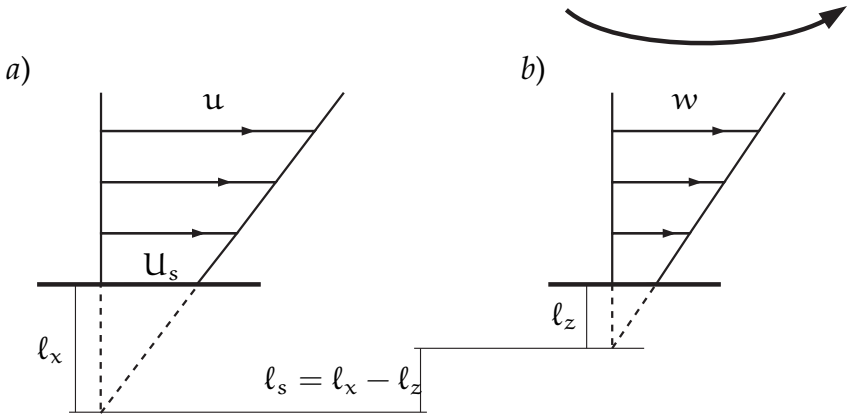

Figure 6.2.: Sketch of (*a*) streamwise and (*b*) spanwise slip lengths. In (*b*), the top arrow represents an overlying spanwise perturbation, which is perceived locally as quasi-steady and quasi-stationary under the assumption of vanishingly small surface texture.

characteristic size of the pores is much smaller than any other length scale in the problem, and in particular the viscous length scale. A real material would have a finite pore size that, as the Reynolds number increases, would eventually not be negligible compared to the viscous length scale, and the model for vanishingly small texture would stop holding. However, it is shown below that for other drag-reducing surfaces the theory holds reasonably well up to texture sizes of order $\mathcal{O}(10)$ wall-units (Busse and Sandham, 2012). Similarly, roughness typically behaves as hydraulically smooth up to roughness sizes of 3 to 5 wall units (Jiménez, 2004), so we can expect the effect of the granularity of the surface to be negligible up to these sizes.

6.2.1. Drag reduction by slip lengths

We summarise here the relationship between ℓ_x, ℓ_z and drag reduction, as laid out by Jiménez (1994), Luchini (1996) and García-Mayoral and Jiménez (2011). We have seen in chapter 1 that, in the classical theory of wall turbulence, surface manipulations only modify the intercept of the logarithmic velocity profile. The mean velocity profile, U, in the logarithmic layer can be expressed as that for a smooth wall plus a shift, ΔU, as in equation (1.1). This expression allows us

to directly connect the shift of the logarithmic velocity profile to variations in skin friction, as shown in equation (1.4). In turn, ΔU^+ relates to the slip length induced at the surface. In the limit of vanishingly small surface manipulations, ΔU^+ satisfies

$$\Delta U^+ = \mu_0(\ell_x^+ - \ell_z^+) = \mu_0 \ell_s^+, \tag{6.3}$$

where μ_0 is a universal constant of order one (Jiménez, 1994; Luchini, 1996; Bechert et al., 1997) and $\ell_s = \ell_x - \ell_z$. This concept was proposed by Luchini et al. (1991) and Luchini (1996) for riblets, and Jiménez (1994) found that equation (6.3) holds for any vanishingly small surface manipulation. Intuitively, if the cross-flow is more impeded than the streamwise flow, the motion induced by quasi-streamwise vortices is hindered, so they are 'pushed away' from the notional wall perceived by the mean streamwise flow, as sketched in figure 6.2. This reduces the entrainment of momentum from layers farther away from the wall, reducing the shear at the wall and thus the skin friction. Min and Kim (2004) showed that the presence of streamwise slip attenuates turbulent fluctuations, while the spanwise slip has the opposite effect, intensifying turbulence fluctuations, this had been done previously for riblets by Choi et al. (1993). Busse and Sandham (2012) conducted simulations for a wide range of slip lengths, and their results are consistent with equation (6.3) up to slip lengths $\lesssim 5$ wall-units. In chapter 4 we expand on this idea, attempting to establish an expression for ΔU^+ in the context of roughness.

Equations (1.4) and (6.3) provide an estimate for the drag reduction, DR, in the range of validity of small slip lengths. For typical flows at friction Reynolds numbers $Re_\tau \approx 1000 - 10000$, the friction coefficient is $c_{f_0} \approx 0.006 - 0.0025$, and the drag reduction produced by a given ℓ_x^+ and ℓ_z^+ pair is

$$DR \approx -\frac{\Delta\tau}{\tau_0} \approx -\frac{\Delta c_f}{c_{f_0}} \approx \frac{\mu_0}{(2c_{f_0})^{-1/2}}\,\ell_s^+ \approx 0.05\,(\ell_x^+ - \ell_z^+)\,. \tag{6.4}$$

Note that equation (6.4) is obtained using equation (6.3), which holds only for small surface manipulations. For high values of ℓ_s^+, equation (6.3), and consequently equation (6.4), would cease to hold as other mechanisms set in. In the seal fur experiments of Itoh et al. (2006), for instance, DR only increases up to ℓ_s^+

of order 2-4.

6.2.2. Slip lengths by porous media

In the case of an anisotropic permeable coating as that depicted in figure 5.3, the slip lengths can be calculated by solving the flow within the porous layer in response to an overlying shear. This is analogous to the calculation of slip lengths for superhydrophobic textures (Philip, 1972; Ybert et al., 2007) or of protrusion heights for riblets (Luchini et al., 1991). When the porous medium is configured as a swarm of particles (Brinkman, 1947; Taylor, 1971; Auriault, 2009), the flow is highly connected and any section through the material would cut mostly through fluid. The macroscale shear between the fluid on either side of the section would in general not be negligible, and can be accounted for by adding a macroscale viscous term to equation (6.1),

$$\tilde{\nu}\,\nabla^2\boldsymbol{u} - \nu\,K^{-1}\boldsymbol{u} - \nabla p = 0, \tag{6.5}$$

where the apparent viscosity, $\tilde{\nu}$, accounts for diffusion in scales much larger than the pore size (Brinkman, 1947; Taylor, 1971; Auriault, 2009), i.e. the large scale diffusion that would be missed by the volume average $\nu\,K^{-1}\vec{u}$, the classical Darcy term. Equation (6.5) is the Darcy-Brinkman equation (Darcy, 1856; Brinkman, 1947) which was also obtained by Taylor (1971) for a matrix of infinitesimal obstacles. In general, the empirically observed $\tilde{\nu}$ is different from ν, which accounts for the macroscale diffusive effects acting less efficiently than in the absence of obstacles.

If the material configuration is better represented as a matrix of microducts, rather than a swarm of obstacles, large-scale diffusion is essentially impeded and the Brinkman term should be ommited, recovering equation (6.1). At interfaces, a discontinuity in the macroscale velocity is empirically observed (Beavers and Joseph, 1967), which can be represented by a jump condition. For these configurations, here we use the widespread jump condition proposed by Beavers and

Joseph (1967), which along the streamwise direction reads

$$\left.\frac{dU}{dy}\right|_s = \frac{\alpha_{BJ}}{\sqrt{K_x}}\left(U_s - U_D\right), \tag{6.6}$$

where U_D is the velocity inside the coating, produced by the Darcy term, α_{BJ} is an empirical coefficient, which depends on the interface and the permeable material, and the subindex '$_s$' denotes variables right above the interface.

Let us consider the flow within the substrate driven by an overlying uniform streamwise shear S_x alone, the spanwise and wall-normal velocities are zero and the pressure is homogeneous. Since the flow is assumed to be shear-driven, $U_D \approx 0$, and equation (6.6) in viscous units becomes

$$S_x^+ \approx \frac{\alpha_{BJ}}{\sqrt{K_x^+}} U_s^+. \tag{6.7}$$

This equation, and its analogous along the spanwise direction, lead to estimations of the slip lengths based on Beavers-Joseph's jump condition,

$$\ell_x^+ \approx \frac{\sqrt{K_x^+}}{\alpha_{BJ}}, \qquad \ell_z^+ \approx \frac{\sqrt{K_z^+}}{\alpha_{BJ}}. \tag{6.8}$$

Let us now address swarm-of-obstacles configurations, described by equation (6.5). Again, the pressure terms are zero and the flow is driven by the overlying uniform streamwise shear S_x. The streamwise component of equation (6.5) becomes then

$$\frac{\partial^2 u}{\partial y^2} - \frac{\nu}{\tilde{\nu}}\frac{1}{K_x} u = 0, \tag{6.9}$$

which has solutions of the form $u \propto \exp\left(y/\sqrt{K_x \tilde{\nu}/\nu}\right)$. Boundary conditions can be obtained by imposing no slip at the bottom boundary, $y = -h_p$, and continuity of the tangential shear stress at the interface with the overlying flow, $y = 0$. The resulting flow depends linearly on S_x, and the relationship between u and $\partial u/\partial y$ at $y = 0$ gives an S_x-independent slip length, which expressed in wall units is

$$\ell_x^+ = \sqrt{\nu/\tilde{\nu}}\sqrt{K_x^+}\tanh\left(\frac{h_p^+}{\sqrt{\tilde{\nu}/\nu}\sqrt{K_x^+}}\right). \tag{6.10}$$

An analogous expression can similarly be derived for the spanwise slip,

$$\ell_z^+ = \sqrt{\nu/\tilde{\nu}}\sqrt{K_z^+}\tanh\left(\frac{h_p^+}{\sqrt{\tilde{\nu}/\nu}\sqrt{K_z^+}}\right). \tag{6.11}$$

Equations (6.8) and (6.10) are in agreement with the experimental measurements of Suga et al. (2010), who found streamwise slip lengths of order $\mathcal{O}\left(\sqrt{K_x^+}\right)$ for $\ell_x^+ \lesssim 3$.

An expression for DR can be obtained by introducing the estimates of equations (6.10) and (6.11) into equation (6.4). As we are interested in obtaining drag reduction from a positive effective slip, $\ell_s^+ = \ell_x^+ - \ell_z^+ > 0$, we focus on drag reducing configurations with $\ell_x^+ > \ell_z^+$, and thus $K_x^+ > K_z^+$. With this constraint, depending on the relative value of h_p, we can distinguish three regimes. For small values of substrate thickness, $h_p^+ \lesssim \sqrt{K_z^+}$, both slips tend to the same value, $\ell_x^+ \approx \ell_z^+ \approx h_p^+$, and therefore $\ell_s^+ \approx 0$, resulting in no drag reduction, DR ≈ 0. For intermediate substrate thickness, $\sqrt{K_x^+} \gtrsim h_p^+ \gtrsim \sqrt{K_z^+}$, a positive drag reduction is obtained since $\ell_x^+ \approx h^+$ is greater than $\ell_z^+ \approx \sqrt{K_z^+}$, giving as a result DR $\propto \left(h_p^+ - \sqrt{K_z^+}\right)$. Finally, if $h_p^+ \gtrsim \sqrt{K_x^+}$ the slip lengths are $\ell_x^+ \propto \sqrt{K_x^+}$ and $\ell_z^+ \propto \sqrt{K_z^+}$, yielding

$$\text{DR} \approx 0.05\sqrt{\frac{\nu}{\tilde{\nu}}}\left(\sqrt{K_x^+} - \sqrt{K_z^+}\right). \tag{6.12}$$

Of the three regimes, the latter is the most advantageous, as it gives the highest performance for a given anisotropic material with a set K. We can conclude that, provided that the substrate has a sufficient depth, $h_p^+ \gtrsim \sqrt{K_x^+}$, an optimal design should have high anisotropy in order to maximise K_x^+ while keeping K_z^+ as low as possible.

The Beavers-Joseph model leads to similar conclusions to those from the Brinkman model above. Using equations (6.4) and (6.8) yields

$$\text{DR} \approx 0.05\frac{1}{\alpha_{BJ}}\left(\sqrt{K_x^+} - \sqrt{K_z^+}\right), \tag{6.13}$$

which closely resembles equation (6.12), and where the same influence of $\left(\sqrt{K_x^+} - \sqrt{K_z^+}\right)$

is observed. With this model, however, α_{BJ} takes the place of $\tilde{\nu}/\nu$ in the relationship between shear stress and velocity at the interface, with drag reduction increasing with decreasing values of α_{BJ}.

Equations (6.12) and (6.13) also allow us to identify the influence of the permeability and thickness of the substrate. The drag reduction is essentially determined by the difference between streamwise and spanwise permeabilities, $\sqrt{K_x^+} - \sqrt{K_z^+}$, and, on the contrary to the stability analysis in section 5.2, the wall-normal permeability does not play a significant role in this linear regime. Both models agree that the permeable material should ideally be highly anisotropic in order to obtain a large $\sqrt{K_x^+} - \sqrt{K_z^+}$, and therefore high drag reduction. These models also show that the connectivity of the microstructure of the substrate, condensed in either $\tilde{\nu}$ or α_{BJ}, also plays an important role. Materials with high connectivity will allow larger slip at the interface, and therefore have a positive effect on DR. We must however note that expressions (6.12) and (6.13) only provide an estimate of the order of magnitude of the drag reduction, and that a more refined characterisation of the permeable substrate would be required for more precise estimates. The main source of uncertainty in equations (6.12) and (6.13) are the estimates for $\tilde{\nu}/\nu$ or α_{BJ}, which encapsulate the interaction between fluid and porous material at the interface. Zampogna and Bottaro (2016) and Lācis and Bagheri (2017) have recently proposed homogenisation techniques to predict this interaction accurately.

Using either model results in expressions for the slip lengths that closely resemble each other, when deep coatings are assumed. The coefficients α_{BJ} and $\sqrt{\tilde{\nu}/\nu}$ play the same role, as proposed by Neale and Nader (1974), which allows us to write equations (6.12) and (6.13) in the form

$$DR \approx 0.05\xi \left(\sqrt{K_x^+} - \sqrt{K_z^+} \right), \tag{6.14}$$

where ξ is either $\sqrt{\nu/\tilde{\nu}}$ or α_{BJ}^{-1}.

This result provides an expression for the order of magnitude of drag reduction obtained by permeable substrates. The above derivation neglects the effect of pressure within the substrate, which is negligible in most industrial applications. For example, in order to produce drag reduction of order $\mathcal{O}(10\%)$,

the permeability of the material would be $\sqrt{K_x^+} \approx$ 2-3, which would require a thickness of order $h_p^+ \sim \mathcal{O}(10)$. In industrial ducts and pipelines, for instance, the Reynolds number is 10^5-10^7, and the above thickness would correspond to $h_p \sim \mathcal{O}(100\,\mu m)$, resulting in an additional cross-section of order $\mathcal{O}(1\%)$. The additional drag caused by the pressure drop acting in this increased cross-section would then be $\mathcal{O}(1\%)$, much smaller than the DR caused by the slip effect. Moreover, this pressure drop would create additional Darcy flow within the coating, resulting in increased flow rate not only within the coating, but also across the whole section. This would mitigate the deleterious effect, and could even negate it, depending on the coating parameters. In turn, in external flows, like aeroplane fuselages, the pressure gradient is generally milder and therefore its effect on the substrate would not contribute significantly to drag. The coating thickness would also be of order of microns in this case, and the shape, and hence the form drag, would not change noticeably.

6.3. A limiting mechanism for drag reduction

Just like in the classical studies of Jiménez (1994) and Luchini (1996), the model presented in section 6.2 predicts a drag reduction ever-increasing with the surface permeability, scaled in viscous units. Let us take a given substrate configuration (K_x, K_z, K_y, h_p), yielding an effective slip $\ell_s > 0$. By simply increasing the friction velocity of the flow, the viscous length scale would decrease and $\sqrt{K_x^+}$, $\sqrt{K_z^+}$, and h_p^+ would increase by the same proportion, with the corresponding increase in DR, as given by equation (6.14). This is obviously not the case, because the theory and the resulting models cease to hold once the texture size, in viscous units, reaches a certain value. The theory developed by Luchini et al. (1991) and Luchini (1996) and Jiménez (1994) assumes slip lengths much smaller than one viscous unit, or in our case $\sqrt{K_x^+} \ll 1$. The linear behaviour is nevertheless observed to hold for $\sqrt{K_x^+} \lesssim 5$, but even beyond this value the drag reduction keeps increasing monotonically with $\sqrt{K_x^+}$ (Busse and Sandham, 2012). In experience, however, other mechanisms, different from the slip effect and dependent on the type of surface, can be expected to set in at some $\sqrt{K_x^+}$ and limit the drag reducing capability of the surface, as discussed in section 6.1.

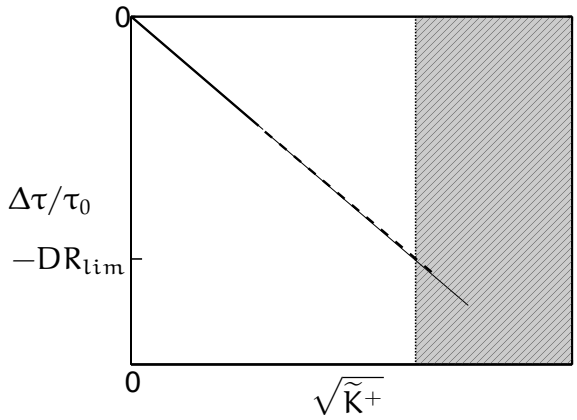

Figure 6.3.: Schematic summarising the inital linear behaviour of $DR = \Delta\tau/\tau_0$ for low permeability. The hatched area represent the region $\widetilde{K} > \widetilde{K}_{KH}$, where the drag reducing effect is destroyed by the appearance of Kelvin-Helmholtz rollers.

In chapter 5, we have studied the development of a shear-flow instability over obstructed flows. In particular, in section 5.2, the stability of a idealised roughness surface is analysed using a permeable substrate model, whose results directly apply to the permeable substrate treated in this chapter. This model predicts the onset of a Kelvin-Helmholtz-like instability and the appearance of spanwise rollers for values of the parameter $\widetilde{K}$ larger than the threshold value $\widetilde{K}_{KH}$. These rollers will degrade the linear performance assumed in section 6.2, as the rollers introduce additional Reynolds stresses (García-Mayoral and Jiménez, 2011). In the absence of earlier degrading mechanisms, the maximum drag reduction would occur for $\widetilde{K}^+ = \widetilde{K}^+_{KH}$, so $\widetilde{K}^+_{KH}$ can be taken as an upper bound for the limit of the drag-decreasing regime.

6.4. Limit to drag reduction by permeable coatings

In section 6.2 we have analysed the drag reduction for substrates of vanishing permeability. For these substrates, the slip lengths can be estimated as a function of the permeability, resulting in equation (6.14), which connects DR with the properties of a particular permeable substrate. Within the limits of the vanishingly small assumption, equation (6.14) denotes an ever-increasing DR with

$\sqrt{K_x^+}$. This result is consistent with numerical experiments on walls with anisotropic slip lengths (Hahn et al., 2002; Min and Kim, 2004; Busse and Sandham, 2012). However this behaviour will eventually fail for large permeabilities, once the assumptions in the model break down or additional mechanisms set in. To bound the range of validity of the model, the stability analysis presented in section 5.2 can be used to investigate the appearance of Kelvin-Helmholtz-like rollers, which are a common feature in flows over porous materials (Jiménez et al., 2001; Breugem et al., 2006). The appearance of these rollers results in enhanced mixing, increasing drag and posing a limitation to the aforementioned linear behaviour. These two concepts are depicted together in figure 6.3, which shows the initial linear behaviour for low permeabilities as well as the limit to drag reduction, DR_{lim}, for high permeabilities, due to the Kelvin-Helmholtz instability. Note that DR_{lim} must only be considered as an upper limit estimate, since in the intermediate range of permeabilities beyond $\sqrt{K_x^+} \ll 1$ we cannot rule out additional mechanisms that may degrade drag further. For riblets, the analogous linear behaviour roughly extends until the onset of the Kelvin-Helmholtz mechanism (García-Mayoral and Jiménez, 2011), although this may not be the case for the present porous substrate, as other degrading phenomena could appear before reaching $\widetilde{K}_{KH}^+$.

Section 6.2 shows that in order to obtain high drag reduction one would need to maximise the difference $\sqrt{K_x^+} > \sqrt{K_z^+}$, while in order to delay the appearance of the drag degrading spanwise rollers the product of permeabilities needs to stay below a threshold, $\sqrt{K_x^+ K_y^+} < \widetilde{K}_{KH}^+$, as shown in section 5.2. A high value of ξ, corresponding to substrates with sparse internal structure, is also desirable, noticing that previous research appears to agree that ξ tends to 1 for very sparse porous matrices (Auriault, 2009). These results can be combined to obtain an estimate for the limit to drag reduction produced by different substrates. Let us consider a permeable material with a preferential permeability, $K_x^+ > K_y^+ = K_z^+$. The resulting anisotropy ratio, $\Phi_{xy} = \sqrt{K_x/K_y} = \sqrt{K_x/K_z}$, can be used in equations (6.14) and (5.10) to obtain an expression for the order of magnitude of the upper limit for drag reduction,

$$DR_{lim} \approx 0.05\xi \left(1 - {\Phi_{xy}}^{-1}\right) \sqrt{\Phi_{xy} \widetilde{K}_{KH}^+}. \tag{6.15}$$

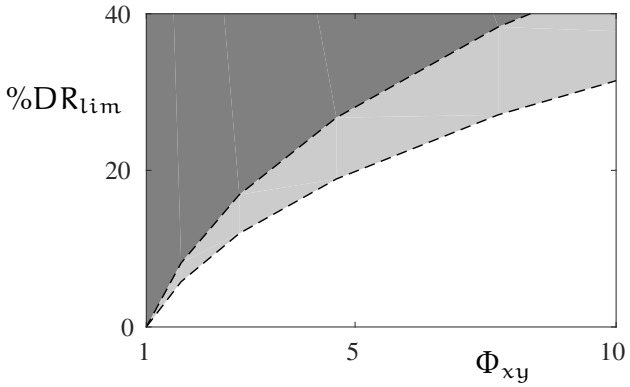

Figure 6.4.: Limit for the maximum drag reduction achievable as a function of the anisotropy ratio of the permeable layer, Φ_{xy}. --, equation (6.15) for $\widetilde{K}^{+}_{KH} = 5$ and 10, and $\xi = 1$. The light grey shaded region indicates the range for which Kelvin-Helmholtz rollers are expected to appear. The dark grey shaded region indicates the range for which the Kelvin-Helmholtz rollers would be fully developed.

Figure 6.4 portrays an example of the resulting $\Phi_{xy}-DR$ curves for both $\widetilde{K}^{+}_{KH} = 5$ and 10, in the limit of $\xi = 1$. The region enclosed by the two curves represents the range for which Kelvin-Helmholtz rollers can be expected to appear and delimits the range of realisable values for DR. For an anisotropy ratio of order $\Phi_{xy} \approx 5 - 10$ the maximum drag reduction achievable would be below $20 - 30\%$. Note however that for substrates that impede diffusion the drag reduction capability can be substantially smaller. For the substrate of Lācis and Bagheri (2017), for instance, $\xi \approx 0.25$, which would yield a drag reduction of no more than $5 - 7\%$. And thus, we can only estimate that $DR_{lim} = \mathcal{O}(10\%)$ with an anisotropy of order $\Phi_{xy} \approx 5 - 10$.

6.5. Conclusions and discussion

In the transitionally rough regime, riblet drag reduction is destroyed by the appearance of a shear-flow instability (García-Mayoral and Jiménez, 2011). The model developed in chapter 5, and based on permeability equations, shows that these instabilities could also develop over such permeable substrates. Inspired by these similarities and, in view of the preferential alignment of riblets, in this

chapter we have explored the capabilities of anisotropically permeable surfaces to reduce drag.

In the present chapter, we have proposed a simplified model to estimate the drag reduction properties of anisotropically permeable coatings. For small permeabilities, permeable substrates can potentially reduce skin friction if the surface obstructs more the spanwise than the streamwise flow, as riblets and some other drag-reducing surfaces do. Using simplified models, a relationship between drag reduction, slip length at the interface, and the properties of the porous material is established. This results in the drag reduction being approximately proportional to the difference between the streamwise and spanwise permeabilities, provided that the coating is sufficiently deep, $h_p^+ \gtrsim \sqrt{K_x^+} > \sqrt{K_z^+}$.

We have also investigated a limit to the drag-reducing capabilities of these surfaces, given by the triggering of Kelvin-Helmholtz-like rollers over the surface. These are common features of turbulent flows over permeable substrates and other complex surfaces, and are responsible for increased momentum transfer that increases drag. Their appearance will limit the drag reduction performance, which, in the absence of degrading mechanisms, would continuously improve as the permeability of the surface, measured in wall units, increases. This can be used to set an upper bound for the performance of the surfaces under consideration. A model derived from inviscid linear stability analysis indicates that the critical parameters for the onset of rollers scale in viscous units. The appearance of rollers is estimated to trigger for $\sqrt{K_x^+ K_y^+} \gtrsim \widetilde{K}_{KH}^+ \approx 5$–$10$. This implies that the anisotropically permeable substrates considered could yield drag reductions of order $\mathcal{O}(10\%)$, for anisotropy ratios of $\sqrt{K_x^+/K_y^+} = \sqrt{K_x^+/K_z^+} \approx 5 - 10$. This preliminary figure is promising, but requires further study to delimit more precisely the potential of these surfaces.

7. Conclusions and outlook

In the present work, we have investigated the interaction between small surface roughness and near-wall turbulence, and how roughness increases drag in turbulent flows. We have focused on the transitionally rough regime, to capture and model the effects that trigger the departure from the hydraulically smooth regime.

7.1. The roughness-coherent and the background-turbulent contributions

Analysing the instantaneous velocity field, we observe that the flow is composed of two contributions: a background-turbulent component, similar to that over smooth walls; and a roughness-coherent one, induced by the rough surface. While other decompositions have been proposed in the literature, in this work, we have presented a triple decomposition where the roughness-coherent contribution is modulated in amplitude by the overlying background-turbulent flow. To study the interaction between roughness and the near-wall turbulence, the changes on the background-turbulent component are investigated. Using this decomposition, a background turbulence component, essentially free of any footprint from the roughness texture, can be obtained from the full signal. Accounting for the modulation of the roughness-coherent contribution improves the extraction of the footprint of roughness. Without this modulation, the background turbulence obtained displays a significant footprint from the rough surface. The modulated triple decomposition has proven here to effectively extract the background turbulent contribution of instantaneous velocity realisations, rms fluctuations of the velocity and their density spectra. In particular, spectral

analysis of the velocity components has identified why the unmodulated triple decomposition is unable to fully filter out the roughness-coherent component, as it does not remove the modulation that appears in wavelengths in the vicinity of those of the roughness texture. In addition, the interaction between roughness and turbulence, displayed in the spectrum as elongated regions of high-energy, is also missed. The flow decomposition proposed in this work addresses these two issues, achieving substantial improvement, especially for small roughness size. It allows us to decompose the flow into two contributions with two different origins and whose physics can then be studied separately.

The region where the flow is affected by the rough surface, the roughness sublayer, is classically considered to extend to a height of $y^+ \approx 3$–$5k^+$. However, we observe that all components of the roughness-coherent contribution seem to essentially vanish for $y^+ \lesssim k^+$. This suggests that the modifications of the flow are present in the background-turbulent component at a larger distance from the wall than the contribution of the roughness-coherent component. The roughness-coherent velocity components, which can be obtained from the time-averaged flow field, exhibit an exponential decay with $-y/k$. Notice, however, that the simplified viscous analysis suggests a decay with the wavelength of the texture, s, instead of with the roughness size, k. We also find that the rate of decay depends on the velocity component, with the wall-normal velocity experiencing the slowest decay.

By using the triple decomposition, the roughness-coherent contribution can be extracted from the full signal, allowing us to investigate the changes produced in the background turbulence. For a large extent of the transitionally rough regime, $\Delta U^+ \lesssim 4$, the most relevant effect of roughness on the background-turbulent component is the displacement towards the wall of the rms fluctuations of the velocity and the Reynolds shear stress, while their shapes remain similar to those of smooth-wall turbulence. This is interpreted as turbulence perceiving an effective wall at a certain virtual origin below the roughness crests. In particular, the virtual origin of the Reynolds shear stress, ℓ^+_{uv}, seems to be the one perceived by turbulence, and therefore the one that affects the skin friction. This is in agreement with Townsend's hypothesis (Townsend, 1976), which we observe to hold even for height ratios as low as $\delta/k \approx 5$, as all fluctuations

perceive the same virtual origin farther away from the wall. We find a strong linear correlation between the virtual origin of the Reynolds shear stress, ℓ^+_{uv}, and the roughness function, ΔU^+. This is reminiscent of the relation between ΔU^+ and the rms of the wall-normal velocity fluctuations observed by Orlandi and Leonardi (2006). These findings suggest a link between the transpiration of the surface, measured by $\bar{v}'^+_t$, and the depth of the shift experienced by turbulence, ℓ^+_{uv}. We also observe a strong correlation between the virtual origin of the streamwise rms fluctuations, ℓ^+_u, the mean velocity profile, ℓ^+_U, and the displacement height of the mean velocity profile, ℓ^+_J.

7.2. Towards a model for the roughness function

The mean momentum equation has been integrated to investigate the effects that contribute to ΔU^+, and in particular the role of ℓ^+_{uv}. Results show that, in the initial departure from hydraulically smooth regime, the main contribution to the roughness function is the change in Reynolds shear stress, which for small roughness is essentially due to a shift ℓ^+_{uv} of the otherwise canonical, smooth-wall Reynolds shear stress. The other term with an impact on ΔU^+ is the mean velocity over the roughness crests. This velocity is smaller than the one that would be obtained without roughness, and therefore contributes negatively to the roughness function, increasing drag. This decomposition, together with a laminar model for the roughness-coherent contribution and the concept of ℓ^+_{uv}, allows us to propose a model for ΔU^+. The change in Reynolds stress is approximated by the smooth-wall solution shifted to the corresponding ℓ^+_{uv}. The change in velocity at the tips, as well as ℓ^+_U, are obtained from the laminar simulations. The model provides a rough approximation of the roughness function for $\Delta U^+ \lesssim 2$, capturing the initial departure of these surfaces from the hydraulically smooth regime towards the fully rough regime. Although this model offers an estimate of ΔU^+, a predictive model for ℓ^+_{uv} is yet needed. If such a model for ℓ^+_{uv} could be developed, the range of validity of the full model could also be extended to a larger region or even the entirety of the transitionally rough regime.

For the model described above, it is necessary to approximate the roughness-

coherent component without having to conduct the full direct numerical simulation of a particular rough surface. Since, for small roughness size, the roughness-coherent flow can be thought of as the flow induced by the roughness elements and driven by a steady, homogeneous overlying shear, we have proposed to estimate the roughness-coherent component by using laminar simulations at the corresponding finite Reynolds number, and where the flow is driven by a steady, homogeneous shear. The resulting steady flow field, as well as its rms fluctuations, agree well with DNS results, up to at least $\Delta U^+ \lesssim 2$. This laminar model also provides estimates for the mean velocity at the roughness tips, U_0^+, and the virtual origin of the mean velocity profile, ℓ_U^+. This model is therefore one key piece of the model for ΔU^+ also proposed in this work. However, to predict the whole transitional regime, the laminar model needs to be improved, as it presents significant discrepancies for $\Delta U^+ \gtrsim 2$. In addition, the model needs to be tested on surfaces with random roughness, and also regular patterns with different arrangements, different shapes, etc.

7.3. Analysis of shear-flow instability

We have also observed that, as roughness size increases, energy increases at short λ_x^+ wavelengths. In particular, energy tends to concentrate at $\lambda_x^+ \sim 150$. These changes in the energy spectra are somewhat similar, although much weaker, to those observed over riblets, due to the appearance of a shear-flow instability. The simplified stability analysis on the mean velocity profile of our direct numerical simulations results in wavelengths $\lambda_x^+ \sim 100$–150 being the most amplified. While the characteristic Kelvin-Helmholtz rollers are not directly observed in our flow fields, the stability analysis points to a possible relationship between the instability and the growth of energy at that particular range of streamwise wavelengths. This stability analysis relies on results from direct numerical simulations to obtain the mean velocity profiles. Therefore, we present an analysis that characterises the surfaces using a permeable model to mimic the obstruction of the surface as an impedance boundary condition, based on a similar study on riblets (García-Mayoral and Jiménez, 2011). Results from this model are consistent with those using direct numerical data.

7.4. Anisotropically permeable substrates for drag reduction

The results from the permeable model for roughness directly apply to permeable substrates. The concept of these permeable coatings is explored and we have found that under certain configurations they can yield drag reduction. In particular, the porous matrix needs to be anisotropic, with preferential flow in the streamwise direction, and the parameter $\widetilde{K}$ needs to be smaller than $\widetilde{K}_{KH}$, so a Kelvin-Helmholtz-like instability does not develop in the flow, leading to an increase in skin friction. The development of these instabilities has also been reported in literature of riblets and canopy flows, and has been observed to increase drag.

7.5. Future work

In the present work, we have proposed a model for the roughness function that provides an approximation for the increase in skin friction produced by rough surfaces. While we have studied different pattern arrangements and included a case with elements of different heights, in all our geometries there is a well-defined dominant wavelength. An interesting path of research is expanding this model to other roughness surfaces, and in particular random roughness. While nothing in our study points towards the model failing for random roughness, it is necessary to investigate if that is indeed the case.

Moreover, some characteristics of the model could be improved in the future. The first aspect to be considered is that the laminar model, used to approximate the roughness-coherent contribution, could be improved to provide better estimates for large roughness height, k^+. Improvements on this method will have a direct impact on the roughness function model. Some elements that could be added to the laminar simulations are, for instance, considering the curvature of the mean velocity profile, as opposed to using a steady, homogeneous shear; and accounting for the turbulent dissipation, as the current model overpredicts the mean velocity at the roughness crests for large k^+. The second aspect to consider

is the approximation of the change in Reynolds shear stress. The model for this term is based on the assumption that the main effect of roughness on the Reynolds shear stress is a shift towards the wall with, otherwise, negligible alterations of its actual shape. However, this assumption does not hold for large roughness as the shape of the Reynolds shear stress begins to be significantly altered for our larger cases. In addition, a model to estimate ℓ_{uv}^{+} based on the roughness geometry remains an open challenge. A possible way to face this problem is by exploring the relationship between the virtual origin of the Reynolds shear stress, ℓ_{uv}^{+}, and the rms of the wall-normal velocity at the roughness crests, as they appear to be closely related.

Another interesting aspect, also related to the modifications of the Reynolds shear stress, is the presence of a shear-flow instability induced by the roughness surface that we have observed. These instabilities have been reported in flows over transitional roughness, in the form of riblets, and over surfaces with wall-normal permeability. This phenomenon could be further explored by studying other surface configurations. For instance, Akshath Sharma is currently working on varying the depth of the roughness elements for a constant spacing, transitioning from a shallower and more conventional roughness surface to a deeper, canopy-like configuration. Another interesting case consists of using elongated posts for a constant height and spanwise spacing, exploring the changes from a cubic geometry to a very elongated or riblet-like surface geometry. In both cases, the goal would be to study the development of a Kelvin-Helmholtz instability and predict its formation.

A. Rms fluctuations decomposition

In section 3.3 approximate expressions for the decomposition of the rms Reynolds stress fluctuations are obtained in a simplified form. Here we present the full expressions including terms whose order of magnitude is negligible in the geometries explored in this work. The approximate decomposition of the rms fluctuations using equations 3.2 are

$$\begin{aligned}\langle u'^2\rangle &= \left\langle \left(u_{BT} + u_{RC,u} + u_{RC,u}\frac{u_{BT}}{U} + u_{RC,v} + u_{RC,v}\frac{v_{BT}}{\widetilde{v}} + u_{RC,w} + u_{RC,w}\frac{w_{BT}}{\widetilde{w}} \right)^2 \right\rangle \\ &= \langle u_{BT}^2\rangle + \langle u_{RC,u}^2\rangle + \langle u_{RC,u}^2\rangle \left\langle \frac{u_{BT}^2}{U^2} \right\rangle + \langle u_{RC,v}^2\rangle \left\langle \frac{v_{BT}^2}{\widetilde{v}^2} \right\rangle + \langle u_{RC,w}^2\rangle \left\langle \frac{w_{BT}^2}{\widetilde{w}^2} \right\rangle \\ &+2\left(\langle u_{RC,u}u_{RC,v}\rangle \left\langle \frac{u_{BT}v_{BT}}{U\widetilde{v}} \right\rangle + \langle u_{RC,u}u_{RC,w}\rangle \left\langle \frac{u_{BT}w_{BT}}{U\widetilde{w}} \right\rangle + \langle u_{RC,v}u_{RC,w}\rangle \left\langle \frac{v_{BT}w_{BT}}{\widetilde{v}\widetilde{w}} \right\rangle \right),\end{aligned} \tag{A.1a}$$

$$\begin{aligned}\langle v'^2\rangle &= \left\langle \left(v_{BT} + v_{RC,u} + v_{RC,u}\frac{u_{BT}}{U} + v_{RC,v} + v_{RC,v}\frac{v_{BT}}{\widetilde{v}} + v_{RC,w} + v_{RC,w}\frac{w_{BT}}{\widetilde{w}} \right)^2 \right\rangle \\ &= \langle v_{BT}^2\rangle + \langle v_{RC,u}^2\rangle + \langle v_{RC,u}^2\rangle \left\langle \frac{u_{BT}^2}{U^2} \right\rangle + \langle v_{RC,v}^2\rangle \left\langle \frac{v_{BT}^2}{\widetilde{v}^2} \right\rangle + \langle v_{RC,w}^2\rangle \left\langle \frac{w_{BT}^2}{\widetilde{w}^2} \right\rangle \\ &+2\left(\langle v_{RC,u}v_{RC,v}\rangle \left\langle \frac{u_{BT}v_{BT}}{U\widetilde{v}} \right\rangle + \langle v_{RC,u}v_{RC,w}\rangle \left\langle \frac{u_{BT}w_{BT}}{U\widetilde{w}} \right\rangle + \langle v_{RC,v}v_{RC,w}\rangle \left\langle \frac{v_{BT}w_{BT}}{\widetilde{v}\widetilde{w}} \right\rangle \right),\end{aligned} \tag{A.1b}$$

$$\begin{aligned}\langle w'^2\rangle &= \left\langle \left(w_{BT} + w_{RC,u} + w_{RC,u}\frac{u_{BT}}{U} + w_{RC,v} + w_{RC,v}\frac{v_{BT}}{\widetilde{v}} + w_{RC,w} + w_{RC,w}\frac{w_{BT}}{\widetilde{w}} \right)^2 \right\rangle \\ &= \langle w_{BT}^2\rangle + \langle w_{RC,u}^2\rangle + \langle w_{RC,u}^2\rangle \left\langle \frac{u_{BT}^2}{U^2} \right\rangle + \langle w_{RC,v}^2\rangle \left\langle \frac{v_{BT}^2}{\widetilde{v}^2} \right\rangle + \langle w_{RC,w}^2\rangle \left\langle \frac{w_{BT}^2}{\widetilde{w}^2} \right\rangle \\ &+2\left(\langle w_{RC,u}w_{RC,v}\rangle \left\langle \frac{u_{BT}v_{BT}}{U\widetilde{v}} \right\rangle + \langle w_{RC,u}w_{RC,w}\rangle \left\langle \frac{u_{BT}w_{BT}}{U\widetilde{w}} \right\rangle + \langle w_{RC,v}w_{RC,w}\rangle \left\langle \frac{v_{BT}w_{BT}}{\widetilde{v}\widetilde{w}} \right\rangle \right),\end{aligned} \tag{A.1c}$$

$$
\begin{aligned}
\langle u'v' \rangle = {} & \langle u_{BT} v_{BT} \rangle + \langle u_{RC,u} v_{RC,u} \rangle \\
& + \langle u_{RC,u} v_{RC,u} \rangle \left\langle \frac{u_{BT}^2}{U^2} \right\rangle + \langle u_{RC,v} v_{RC,v} \rangle \left\langle \frac{v_{BT}^2}{\widetilde{v}^2} \right\rangle + \langle u_{RC,w} v_{RC,w} \rangle \left\langle \frac{w_{BT}^2}{\widetilde{w}^2} \right\rangle \\
& + (\langle u_{RC,u} v_{RC,v} \rangle + \langle u_{RC,v} v_{RC,u} \rangle) \left\langle \frac{u_{BT} v_{BT}}{U\widetilde{v}} \right\rangle + (\langle u_{RC,u} v_{RC,w} \rangle + \langle u_{RC,w} v_{RC,u} \rangle) \left\langle \frac{u_{BT} w_{BT}}{U\widetilde{w}} \right\rangle \\
& + (\langle u_{RC,v} v_{RC,w} \rangle + \langle u_{RC,w} v_{RC,v} \rangle) \left\langle \frac{v_{BT} w_{BT}}{\widetilde{v}\widetilde{w}} \right\rangle . \qquad \text{(A.1d)}
\end{aligned}
$$

Bibliography

Abderrahaman-Elena, N. and García-Mayoral, R. (2016). 'Geometry-induced fluctuations in the transitionally rough regime'. *J. Phys. Conf. Ser.* 708.

Abderrahaman-Elena, N. and García-Mayoral, R. (2017). 'Analysis of anisotropically permeable surfaces for turbulent drag reduction'. *Phys. Rev. Fluids* 2 (11), p. 114609.

Abderrahaman-Elena, N., Fairhall, C. T. and García-Mayoral, R. (2019). 'Modulation of near-wall turbulence in the transitionally rough regime'. *J. of Fluid Mech.* 865, pp. 1042–1071.

Acharya, M., Bornstein, J. and Escudier, M. P. (1986). 'Turbulent boundary layers on rough surfaces'. *Experiments in Fluids* 4.1, pp. 33–47.

Álamo, J. C. del, Jiménez, J., Zandonade, P. and Moser, R. D. (2006). 'Self-similar vortex clusters in the turbulent logarithmic region'. *J. Fluid Mech.* 561, p. 329.

Amir, M. and Castro, I. P. (2011). 'Turbulence in rough-wall boundary layers: universality issues'. *Experiments in Fluids* 51.2, pp. 313–326.

Anderson, W. (2016). 'Amplitude modulation of streamwise velocity fluctuations in the roughness sublayer: evidence from large-eddy simulations'. *J. Fluid Mech.* 789, pp. 567–588.

Auriault, J. L. (2009). 'On the domain of validity of Brinkman's equation'. *Transp. Porous Media* 79.2, pp. 215–223.

Beavers, G. S. and Joseph, D. D. (1967). 'Boundary conditions at a naturally permeable wall'. *J. Fluid Mech.* 30, pp. 197–207.

Bechert, D. W. and Bartenwerfer, M. (1989). 'The viscous flow on surfaces with longitudinal ribs'. *J. of Fluid Mech.* 206, pp. 105–129.

Bechert, D. W., Bruse, M., Hage, W., Hoeven, J. van der and Hoppe, G. (1997). 'Experiments on drag-reducing surface and their optimization with an adjustable geometry'. *J. Fluid Mech.* 338, pp. 59–87.

Beneddine, S., Sipp, D., Arnault, A., Dandois, J. and Lesshafft, L. (2016). 'Conditions for validity of mean flow stability analysis'. *J. Fluid Mech.* 798, pp. 485–504.

Bernardini, M., Pirozzoli, S. and Orlandi, P. (2014). 'Velocity statistics in turbulent channel flow up to Reτ =4000'. *J. Fluid Mech.* 742, pp. 171–191.

Bradshaw, P. (2000). 'A note on critical roughness height and transitional roughness'. *Phys. Fluids.* 12.6, p. 1611.

Breugem, W.-P., Boersma, B. J. and Uittenbogaard, R. E. (2006). 'The influence of wall permeability on turbulent channel flow'. *J. Fluid Mech.* 562, pp. 35–72.

Brinkman, H. C. (1947). 'A calculation of the viscous force exerted by a flowing fluid on a dense swarm of particles'. *Appl. Sci. Res.* A1, pp. 27–34.

Busse, A. and Sandham, N. D. (2012). 'Influence of an anisotropic slip-length boundary condition on turbulent channel flow'. *Phys. Fluids.* 24.5, p. 055111.

Busse, A., Lützner, M. and Sandham, N. D. (2015). 'Direct numerical simulation of turbulent flow over a rough surface based on a surface scan'. *Computers & Fluids* 116, pp. 129–147.

Canuto, C., Hussaini, M. Y., Quarteroni, A. and Zang, T. A. J. (1988). *Spectral methods in fluid dynamics*. Springer-Verlag Berlin Heidelberg.

Castro, I. P. (2007). 'Rough wall boundary layer Mean flow universality'. *J. Fluid Mech.* 585, pp. 469–485.

Cess, R. D. (1958). 'A survey of the literature on heat transfer in turbulent tube flow'. *Rep. 8-0529-R24. Westinghouse Research*

Chan, L., Macdonald, M., Chung, D., Hutchins, N. and Ooi, A. (2015). 'A systematic investigation of roughness height and wavelength in turbulent pipe flow in the transitionally rough regime'. *J. Fluid Mech.* 771, pp. 743–777.

Cheng, H. and Castro, I. P. (2002). 'Near wall flow over urban-like roughness'. *Boundary-Layer Meteorology* 104.2, pp. 229–259.

Choi, H., Moin, P. and Kim, J. (1991). 'On the effect of riblets in fully developed laminar channel flows'. *Phys. Fluids. A: Fluid Dynamics* 3.8, pp. 1892–1896.

Choi, H., Moin, P. and Kim, J. (1993). 'Direct numerical simulation of turbulent flow over riblets'. *J. Fluid Mech.* 255, pp. 503–539.

Chorin, A. J. (1968). 'Numerical solutions of the Navier-Stokes equations'. *Math. Comput.* 22.104, pp. 745–762.

Chu, D. C. and Karniadakis, G. E. (1993). 'A direct numerical simulation of laminar and turbulent flow over riblet-mounted surfaces'. *J. Fluid Mech.* 250, pp. 1–42.

Chung, D., Chan, L., MacDonald, M., Hutchins, N. and Ooi, A. (2015). 'A fast direct numerical simulation method for characterising hydraulic roughness'. *Journal of Fluid Mechanics* 773, pp. 418–431.

Clauser, F. H. (1956). 'The turbulent boundary layer'. *Adv. Appl. Mech* 4, pp. 1–51.

Coceal, O., Dobre, A., Thomas, T. G. and Belcher, S. E. (2007). 'Structure of turbulent flow over regular arrays of cubical roughness'. *J. Fluid Mech.* 589, pp. 375–409.

Colebrook, C. F. (1939). 'Turbulent flow in pipes, with particular reference to the transitional region between smooth and rough wall laws'. *J. Inst. Civ. Eng.* 11, pp. 133–156.

Colebrook, C. F. and White, C. M. (1937). 'Experiments with Fluid Friction in Roughened Pipes'. *Proc. R. Soc. A Math. Phys. Eng. Sci.* 161.906, pp. 367–381.

Cooley, J. W. and Tukey, J. W. (1965). 'An Algorithm for the Machine Computation of the Complex Fourier Series'. *Math. Comput.* 19, pp. 297–301.

Darcy, H. (1856). *Les fontaines publiques de la ville de Dijon*. Dalmont.

del Álamo, J. C. and Jiménez, J. (2006). 'Linear energy amplification in turbulent channels'. *J. Fluid Mech.* 559, pp. 205–213.

Del Álamo, J. C. and Jiménez, J. (2003). 'Spectra of the very large anisotropic scales in turbulent channels'. *Phys. Fluids.* 15.6, pp. 41–44.

Djenidi, L., Elavarasan, R. and Antonia, R. A. (1999). 'The turbulent boundary layer over transverse square cavities'. *J. Fluid Mech.* 395, pp. 271–294.

Dupont, S., Gosselin, F., Py, C., De Langre, E., Hemon, P. and Brunet, Y. (2010). 'Modelling waving crops using large-eddy simulation: comparison with experiments and a linear stability analysis'. *J. Fluid Mech.* 652, pp. 5–44.

Fadlun, E. A., Verzicco, R., Orlandi, P. and Mohd-Yusof, J (2000). 'Combined Immersed-Boundary Finite-Difference Methods for Three-Dimensional Complex Flow Simulations'. *J. Comput. Phys.* 161, pp. 35–60.

Fairhall, C. T., Abderrahaman-Elena, N. and García-Mayoral, R. (2018). 'The effect of slip and surface texture on turbulence over syperhydrophobic surfaces'. *For consideration in J. Fluid Mech.*

Ferziger, J. H. and Perić, M. (2002). *Computational methods for fluid dynamics*. 3rd ed. Springer.

Finnigan, J. (2000). 'Turbulence in plant canopies'. *Annu. Rev. Fluid Mech.* 32, pp. 519–571.

Flack, K. A. (2018). 'Moving beyond Moody'. *J. Fluid Mech.* 842, pp. 1–4.

Flack, K. A. and Schultz, M. P. (2010). 'Review of Hydraulic Roughness Scales in the Fully Rough Regime'. *J. Fluids Eng.* 132, p. 041203.

Flack, K. A. and Schultz, M. P. (2014). 'Roughness effects on wall-bounded turbulent flows'. *Phys. Fluids.* 26.10, p. 101305.

Flack, K. A., Schultz, M. P. and Connelly, J. S. (2007). 'Examination of a critical roughness height for outer layer similarity'. *Phys. Fluids.* 19, p. 095104.

Florens, E., Eiff, O. and Moulin, F. (2013). 'Defining the roughness sublayer and its turbulence statistics'. *Exp. Fluids.* 54.4, p. 1500.

Flores, O. and Jiménez, J. (2006). 'Effect of wall-boundary disturbances on turbulent channel flows'. *J. Fluid Mech.* 566, pp. 357–376.

Flores, O. and Jiménez, J. (2010). 'Hierarchy of minimal flow units in the logarithmic layer'. *Phys. Fluids.* 22, pp. 1–4.

Ganapathisubramani, B., Hutchins, N., Monty, J. P., Chung, D. and Marusic, I. (2012). 'Amplitude and frequency modulation in wall turbulence'. *J. Fluid Mech.* 712, pp. 61–91.

García-Mayoral, R. and Jiménez, J. (2011). 'Hydrodynamic stability and breakdown of the viscous regime over riblets'. *J. Fluid Mech.* 678, pp. 317–347.

García-Mayoral, R, Seo, J and Mani, A (2014). 'Dynamics of gas-liquid interfaces in turbulent flows over superhydrophobic surfaces'. *Proc. Summer Progr.* Center for Turbulence Research, pp. 295–304.

García-Mayoral, R. (2011). 'The Interaction of Riblets with Wall-bounded Turbulence'. PhD thesis. Universidad Politécnica de Madrid.

García-Mayoral, R. and Jiménez, J. (2011). 'Drag reduction by riblets.' *Phil. Trans. R. Soc. A* 369, pp. 1412–1427.

Garcia-Mayoral, R., Segura, G. G. de and Fairhall, C. T. (2018). 'The control of near-wall turbulence through surface texturing'. *Fluid Dyn. Res.*

Ghisalberti, M. (2009). 'Obstructed shear flows: similarities across systems and scales'. *J. Fluid Mech.* 641, pp. 51–61.

Ghisalberti, M. and Nepf, H. M. (2006). 'The structure of the shear layer in flows over rigid and flexible canopies'. *Environ. Fluid. Mech.* 6, pp. 277–301.

Gómez-de-Segura, G., Fairhall, C., MacDonald, M., Chung, D. and García-Mayoral, R. (2018a). 'Manipulation of near-wall turbulence by surface slip and permeability'. *J.Phys.: Conf. Ser.* 1001, p. 012011.

Gómez-de-Segura, G., Sharma, A. and García-Mayoral, R. (2018b). 'Analysis of Kelvin-Helmholtz instabilities in turbulent flows over anisotropic permeable substrates'. *(In preparation)*.

Gómez-de-Segura, G., Sharma, A. and García-Mayoral, R. (2018c). 'Turbulent drag reduction using anisotropic permeable substrates'. *Flow Turbul. Combust.* 100.4, pp. 995–1014.

Hahn, S., Je, J. and Choi, H. (2002). 'Direct numerical simulation of turbulent channel flow with permeable walls'. *J. Fluid Mech.* 450, pp. 259–285.

Hama, F. R. (1954). 'Boundary-layer characteristics for smooth and rough surfaces'. *Trans. Soc. Nav. Archit. Mar. Engrs* 62, pp. 333–358.

Hoyas, S. and Jiménez, J. (2006). 'Scaling of the velocity fluctuations in turbulent channels up to Reτ=2003'. *Phys. Fluids.* 18.011702, pp. 1–4.

Hutchins, N. and Marusic, I. (2007). 'Evidence of very long meandering features in the logarithmic region of turbulent boundary layers'. *J. Fluid Mech.* 579, pp. 1–28.

Iaccarino, G. and Verzicco, R. (2003). 'Immersed boundary technique for turbulent flow simulations'. *Appl. Mech. Rev.* 56.3, p. 331.

Ikeda, S. and Kanazawa, M. (1996). 'Three-dimensional organized vortices above flexible water plants'. *J. Hydraul. Eng* 122, pp. 634–640.

Itoh, M., Tamano, S., Iguchi, R., Yokota, K., Akino, N., Hino, R. and Kubo, S. (2006). 'Turbulent drag reduction by the seal fur surface'. *Phys. Fluids.* 6.18, p. 065102.

Jackson, P. S. (1981). 'On the displacement height in the logarithmic velocity profile'. *J. Fluid Mech.* 111, pp. 15–25.

Jelly, T. O., Jung, S. Y. and Zaki, T. A. (2014). 'Turbulence and skin friction modification in channel flow with streamwise-aligned superhydrophobic surface texture'. *Phys. Fluids.* 26, p. 095102.

Jelly, T. O., Sarakinos, S. and Busse, A. (2017). 'Dependence of near-wall flow on the higher moments of a multi-scale rough surface'. *70th Annual Meeting of the APS Division of Fluid Dynamics*.

Jiménez, J. (1994). 'On the structure and control of near wall turbulence'. *Phys. Fluids.* 6 (2), pp. 944–953.

Jiménez, J. (2004). 'Turbulent flows over rough walls'. *Annu. Rev. Fluid Mech.* 36, pp. 173–196.

Jiménez, J., Uhlmann, M., Pinelli, A. and Kawahara, G. (2001). 'Turbulent shear flow over active and passive porous surfaces'. *J. Fluid Mech.* 442, pp. 89–117.

Jiménez, J. (2018). 'Coherent structures in wall-bounded turbulence'. *J. Fluid Mech.* 842.P1, pp. 1–100.

Jiménez, J. and Moin, P. (1991). 'The minimal flow unit in near-wall turbulence'. *J. Fluid Mech.* 225, pp. 213–240.

Jiménez, J. and Moser, R. D. (2007). 'What are we learning from simulating wall turbulence?' *Philos. Trans. R. Soc. London, Ser. A* 365, pp. 715–732.

Jiménez, J. and Pinelli, A. (1999). 'The autonomous cycle of near-wall turbulence'. *J. Fluid Mech.* 389, pp. 335–359.

Kim, H. T., Kline, S. J. and Reynolds, W. C. (1971). 'The production of turbulence near a smooth wall in a turbulent boundary layer'. *J. Fluid Mech.* 50, pp. 133–160.

Kim, J. and Moin, P. (1985). 'Application of a fractional-step method to incompressible Navier-Stokes equations'. *J. Comput. Phys.* 59, pp. 308–323.

Kim, J., Moin, P. and Moser, R. D. (1987). 'Turbulence statistics in fully developed channel flow at low Reynolds number'. *J. Fluid Mech.* 177, pp. 133–166.

Kline, S. J., Reynolds, W. C., Schraubt, F. A. and Runstadler, P. W. (1967). 'The structure of turbulent boundary layers'. *J. Fluid Mech.* 30.4, pp. 741–773.

Kuwata, Y and Suga, K (2016). 'Lattice Boltzmann direct numerical simulation of interface turbulence over porous and rough walls'. *Int. J. Heat Fluid Flow* 61, pp. 145–157.

Lācis, U. and Bagheri, S. (2017). 'A framework for computing effective boundary conditions at the interface between free fluid and a porous medium'. *J. Fluid Mech.* 812, pp. 866–889.

Le, H. and Moin, P. (1991). 'An improvement of fractional step methods for the incompressible Navier-Stokes equations'. *J. Comput. Phys.* 92, pp. 369–379.

Lee, M. and Moser, R. D. (2015). 'Direct numerical simulation of turbulent channel flow up to $Re\tau \approx 5200$'. *J. Fluid Mech.* 774, pp. 395–415.

Lele, S. K. (1992). 'Compact finite difference schemes with spectral-like resolution'. *J. Comput. Phys.* 103, pp. 16–42.

Leonardi, S., Orlandi, P. and Antonia, R. A. (2007). 'Properties of d- and k-type roughness in a turbulent channel flow'. *Phys. Fluids.* 19.125101, pp. 1–6.

Ligrani, P. M. and Moffat, R. J. (1986). 'Structure of transitionally rough and fully rough turbulent boundary layers'. *J. Fluid Mech.* 162, pp. 69–98.

Lozano-Durán, A. and Jiménez, J. (2014). 'Effect of the computational domain on direct simulations of turbulent channels up to Re = 4200'. *Phys. Fluids.* 26, p. 011702.

Luchini, P., Manzo, F. and Pozzi, A. (1991). 'Resistance of a grooved surface to parallel flow and cross-flow'. *J. Fluid Mech.* 228, pp. 87–109.

Luchini, P. (1996). 'Reducing the turbulent skin friction'. *Comput. Methods Appl. Sci. – Proc. 3rd ECCOMAS CFD Conf.* Pp. 466–470.

Luchini, P. (2017). 'Universality of the Turbulent Velocity Profile'. *Phys. Rev. Lett.* 118.22, pp. 1–4.

Luminari, N., Airiau, C. and Bottaro, A. (2016). 'Drag-model sensitivity of Kelvin-Helmholtz waves in canopy flows'. *Phys. Fluids.* 28, p. 124103.

Lyon, M. and Bruno, O. P. (2010). 'High-order unconditionally stable FC-AD solvers for general smooth domains II. Elliptic, parabolic and hyperbolic PDEs; theoretical considerations'. *J. Comput. Phys.* 229, pp. 2009–2033.

MacDonald, M., Chan, L., Chung, D., Hutchins, N. and Ooi, A. (2016). 'Turbulent flow over transitionally rough surfaces with varying roughness densities'. *J. Fluid Mech.* 804, pp. 130–161.

MacDonald, M., Chung, D., Hutchins, N., Chan, L., Ooi, A. and García-Mayoral, R. (2017). 'The minimal-span channel for rough-wall turbulent flows'. *J. Fluid Mech.* 816, pp. 5–42.

MacDonald, M., Ooi, A., García-Mayoral, R., Hutchins, N. and Chung, D. (2018). 'Direct numerical simulation of high aspect ratio spanwise-aligned bars'. *J. Fluid Mech.* 843, pp. 126–155.

Marusic, I., Mathis, R. and Hutchins, N. (2010a). 'Predictive model for wall-bounded turbulent flow'. *Science* 329, pp. 193–196.

Marusic, I., McKeon, B. J., Monkewitz, P. A., Nagib, H. M., Smits, A. J. and Sreenivasan, K. R. (2010b). 'Wall-bounded turbulent flows at high Reynolds numbers: Recent advances and key issues'. *Phys. Fluids.* 22.6, pp. 1–24.

Mathis, R., Hutchins, N. and Marusic, I. (2009). 'Large-scale amplitude modulation of the small-scale structures in turbulent boundary layers'. *J. Fluid Mech.* 628, pp. 311–337.

Mathis, R., Hutchins, N. and Marusic, I. (2011). 'A predictive inner–outer model for streamwise turbulence statistics in wall-bounded flows'. *J. Fluid Mech.* 681, pp. 537–566.

Min, T. and Kim, J. (2004). 'Effects of hydrophobic surface on skin-friction drag'. *Phys. Fluids.* 16.7, pp. L55–L58.

Mittal, R. and Iaccarino, G. (2005). 'Immersed Boundary Methods'. *Annu. Rev. Fluid Mech.* 37, pp. 239–261.

Mizuno, Y. and Jiménez, J. (2011). 'Mean velocity and length-scales in the overlap region of wall-bounded turbulent flows'. *Phys. Fluids.* 23.8, p. 085112.

Mohd-Yusof, J (1997). 'Combined immersed-boundary/B-spline methods for simulations of flow in complex geometries'. *Annu. Res. Briefs Cent. Turbul. Res.* Pp. 317–327.

Moin, P. and Kim, J. (1982). 'Numerical investigation of turbulent channel flow'. *J. Fluid Mech.* 118, pp. 341–377.

Moin, P. and Mahesh, K. (1998). 'Direct Numerical Simulation: A Tool in Turbulence Research'. *Annu. Rev. Fluid Mech.* 30.1, pp. 539–578.

Moody, L. F. (1944). 'Friction factors for pipe flow'. *Trans ASME* 66, pp. 671–684.

Moser, R. D., Kim, J. and Mansour, N. N. (1999). 'Direct numerical simulation of turbulent channel flow up to Reτ=590'. *Phys. Fluids.* 11.4, pp. 943–945.

Neale, G. and Nader, W. (1974). 'Practical significance of Brinkman's extension of Darcy's law'. *Can. J. Chem. Eng.* 52, pp. 475–478.

Nelson, K. S. and Fringer, O. B. (2017). 'Reducing spin-up time for simulations of turbulent channel flow'. *Phys. Fluids.* 29.10, p. 105101.

Nikuradse, J. (1933). 'Laws of flow in rough pipes'. *NACA TM 1292*

Nordström, J., Mattsson, K. and Swanson, C. (2007). 'Boundary conditions for a divergence free velocity-pressure formulation of the Navier-Stokes equations'. *J. Comput. Phys.* 225, pp. 874–890.

Orlandi, P. (2013). 'The importance of wall-normal Reynolds stress in turbulent rough channel flows'. *Phys. Fluids.* 25, p. 110813.

Orlandi, P. and Jiménez, J. (1994). 'On the generation of turbulent wall friction'. *POF.* 6, pp. 634–641.

Orlandi, P. and Leonardi, S. (2006). 'DNS of turbulent channel flows with two- and three-dimensional roughness'. *J. Turbul.* 7.53, pp. 1–22.

Orszag, S. A. (1971). 'On the elimination of aliasing in finite difference schemes by filtering high-wavenumber components'. *J. Atmos. Sci.* 28, p. 1074.

Perot, B. (1993). 'An analysis of the fractional step method'. *J. Comput. Phys.* 108, pp. 51–58.

Perry, A. E., Schofield, W. H. and Joubert, P. N. (1969). 'Rough wall turbulent boundary layers'. *J. Fluid Mech.* 37.2, pp. 383–413.

Peskin, C. S. (1972). 'Flow patterns around heart valves: A numerical method'. *J. Comput. Phys.* 10.2, pp. 252–271.

Philip, J. R. (1972). 'Flows satisfying mixed no-slip and no-shear conditions'. *Z. Angew. Math. Phys.* 23, pp. 353–372.

Placidi, M. and Ganapathisubramani, B. (2015). 'Effects of frontal and plan solidities on aerodynamic parameters and the roughness sublayer in turbulent boundary layers'. *J. Fluid Mech.* 782, pp. 541–566.

Placidi, M. and Ganapathisubramani, B. (2018). 'Turbulent Flow Over Large Roughness Elements: Effect of Frontal and Plan Solidity on Turbulence Statistics and Structure'. *Boundary-Layer Meteorol.* 167.1, pp. 99–121.

Pope, S. B. (2001). *Turbulent Flows*. IOP Publishing.

Py, C., De Langre, E. and Moulia, B. (2006). 'A frequency lock-in mechanism in the interaction between wind and crop canopies'. *J. Fluid Mech.* 568, pp. 425–449.

Quadrio, M., Frohnapfel, B. and Hasegawa, Y. (2016). 'Does the choice of the forcing term affect flow statistics in DNS of turbulent channel flow?' *Eur. J. of Mech. - B/Fluid.* 55, Part 2, pp. 286–293.

Raupach, M. R., Antonia, R. A. and Rajagopalan, S. S. (1991). 'Rough-Wall Turbulent Boundary Layers'. *Appl. Mech. Rev.* 44, pp. 1–25.

Raupach, M. R. and Shaw, R. H. (1982). 'Averaging procedures for flow within vegetation canopies'. *Boundary-Layer Meteorol.* 22.1, pp. 79–90.

Raupach, M. R., Finnigan, J. and Brunet, Y. (1996). 'Coherent eddies and turbulence in vegetation canopies: The mixing-layer analogy'. *Bounddary-Layer Meteorol.* 78.3-4, pp. 351–382.

Rayleigh, L. (1879). 'On the stability, or instability, of certain fluid motions'. *P. Lond. Math. Soc.* 1.1, pp. 57–72.

Reynolds, W. C. and Tiederman, W. G. (1967). 'Stability of turbulent channel flow, with application to Malkus's theory'. *J. Fluid Mech.* 27, pp. 253–272.

Reynolds, W. and Hussain, A. (1974). 'The mechanics of an organized wave in turbulent shear flow. Part 3. Theoretical models and comparisons with experiments'. *J. Fluid Mech.* 54, pp. 263–288.

Robinson, S. K. (1991). 'Coherent Motions in the Turbulence Boundary Layer'. *Annu. Rev. Fluid Mech.* 23, pp. 601–639.

Rosti, M. E., Cortelezzi, L. and Quadrio, M. (2015). 'Direct numerical simulation of turbulent channel flow over porous walls'. *J. Fluid Mech.* 784, pp. 396–442.

Rothstein, J. P. (2010). 'Slip on superhydrophobic surfaces'. *Annu. Rev. Fluid Mech.* 42, pp. 89–109.

Scalo, C., Bodart, J. and Lele, S. K. (2015). 'Compressible turbulent channel flow with impedance boundary conditions'. *Phys. Fluids.* 27.3, p. 035107.

Schlichting, H. (1936). *Experimental investigation of the problem of surface roughness*. Tech. rep.

Schlichting, H. (1968). *Boundary-layer theory*. 7th ed. New York: McGraw-Hill.

Schultz, M. P., Bendick, J. A., Holm, E. R. and Hertel, W. M. (2011). 'Economic impact of biofouling on a naval surface ship'. *Biofouling* 27.1, pp. 87–98.

Seo, J., García-Mayoral, R. and Mani, A. (2015). 'Pressure fluctuations in turbulent flows over superhydrophobic surfaces'. *J. Fluid Mech.* 783, pp. 448–473.

Sharma, A., Segura, G. Gomez-de and Garcia-Mayoral, R (2017). 'Linear stability analysis of turbulent flows over dense filament canopies'. *10th International Symposium on Turbulence and Shear Flow Phenomena, TSFP 2017*. Vol. 2.

Simens, M. P. (2008). 'The study and control of wall bounded flows: El estudio y control de flujos de pared'. PhD thesis. Universidad Politecnica de Madrid.

Smith, C. and Metzler, S. (1983). 'Characterization of low-speed streaks in the near-wall region of a turbulent boundary layer'. *J. Fluid Mech.* 129, pp. 27–54.

Spalart, P. R. (1991). 'Spectral methods for the Navier-Stokes equations with one infinite and two periodic directions'. *J. Comput. Phys.* 96.2, pp. 297–324.

Spalart, P. R. and McLean, J. D. (2011). 'Drag reduction: enticing turbulece, and then industry'. *Phil. Trans. R. Soc. A* 369, pp. 1556–1569.

Squire, H. B. (1933). 'On the stability for three-dimensional disturbances of viscous fluid flow between parallel walls'. *Proc. R. Soc. Lond. A* 142, pp. 621–628.

Suga, K., Matsumura, Y., Ashitaka, Y., Tominaga, S. and Kaneda, M. (2010). 'Effects of wall permeability on turbulence'. *Int. J. Heat Fluid Flow* 31.6, pp. 974–984.

Tammisola, O. and Juniper, M. P. (2016). 'Coherent structures in a swirl injector at Re = 4800 by nonlinear simulations and linear global modes'. *J. Fluid Mech.* 792, pp. 620–657.

Taylor, G. I. (1971). 'A model for the boundary condition of a porous material. Part 1'. *J. Fluid Mech.* 49, pp. 319–326.

Tennekes, H. and Lumley, J. L. (1972). *A First Course in Turbulence*. MIT Press, p. 300.

Thakkar, M., Busse, A. and Sandham, N. D. (2018). 'Direct numerical simulation of turbulent channel flow over a surrogate for Nikuradse-type roughness'. *J. Fluid Mech.* 837, R1.

Tilton, N. and Cortelezzi, L. (2008). 'Linear stability analysis of pressure-driven flows in channels with porous walls'. *J. Fluid Mech.* 604, pp. 411–445.

Townsend, A. A. (1976). *The structure of turbulent shear flow*. Second. Cambridge University Press.

Trefethen, L. N. (1996). *Finite difference and spectral methods for ordinary and partial differential equations*. Unpublished text.

Tseng, Y.-H. and Ferziger, J. H. (2003). 'A ghost-cell immersed boundary method for flow in complex geometry'. *J. Comput. Phys.* 192.2, pp. 593–623.

Vanderwel, C. and Ganapathisubramani, B. (2015). 'Effects of spanwise spacing on large-scale secondary flows in rough-wall turbulent boundary layers'. *J. Fluid Mech.* 774.2013, R2.

Volino, R. J., Schultz, M. P. and Flack, K. A. (2007). 'Turbulence structure in rough- and smooth-wall boundary layers'. *J. Fluid Mech.* 592, pp. 263–293.

Walsh, M. J. and Lindemann, A. M. (1984). 'Optimization and application of riblets for turbulent drag reduction'. *AIAA*

White, B. L. and Nepf, H. M. (2007). 'Shear instability and coherent structures in shallow flow adjacent to a porous layer'. *Journal of Fluid Mechanics* 593, pp. 1–32.

Ybert, C., Barentin, C. and Cottin-Bizonne, C. (2007). 'Achieving large slip with superhydrophobic surfaces: Scaling laws for generic geometries'. *Phys. Fluids.* 19, p. 123601.

Zagni, A. and Smith, K. (1976). 'Channel flow over permeable beds of graded spheres'. *J. Hydr. Div-ASCE.* 102.2, pp. 207–222.

Zampogna, G. A. and Bottaro, A. (2016). 'Fluid flow over and through a regular bundle of rigid fibres'. *J. Fluid Mech.* 792.2016, pp. 5–35.

Zampogna, G. A., Pluvinage, F., Kourta, A. and Bottaro, A. (2016). 'Instability of canopy flows'. *Water Resour. Res.* 52, pp. 5421–5432.

Zhang, C. and Chernyshenko, S. I. (2016). 'Quasisteady quasihomogeneous description of the scale interactions in near-wall turbulence'. *Phys. Rev. Fluids* 1 (1), p. 014401.